NORTHWESTERN UNIVERSITY

Models and Studies of Self-assembled Systems Using High Information Polymer Coated Particles

A DISSERTATION

SUBMITTED TO THE GRADUATE SCHOOL

IN PARTIAL FULFILLMENT OF THE REQUIREMENTS

for the degree

DOCTOR OF PHILOSOPHY

Field of Applied Physics

By

Martin Girard

EVANSTON, ILLINOIS

September 2018

ABSTRACT

Models and Studies of Self-assembled Systems Using High Information Polymer Coated Particles

Martin Girard

Systems of colloids coated with high-information polymers are powerful tools for designing crystal lattice with tailorable properties or studying the fundamentals of crystallization. By changing the colloid-colloid interaction strength or colloid shape, different types of lattices can be assembled. In this thesis, I present novel coarse-grained models to describe high-information polymer coated colloids in simulation and use various explicit chain models to study experimental systems.

Chapter 2 presents a static model based on orbital descriptions that enable calculation of arbitrary interaction potentials and colloid shape. This is intended to alleviate the need for explicit chains in coarse-grained simulations. I show that this model enables computation of assembly of Janus particles with charges on the surface interacting through Yukawa potential.

Chapter 3 extends this orbital model for time-varying orbitals based on an expansion around equilibrium. I revisit the pathological cases observed in assembly of polymer-coated cubes where shell deformation induces phase changes.

Chapter 4 presents the phases observed for various polyhedron colloids coated with deoxyribonuclic acid (DNA). Short DNA enforces packing according to the shape of particle core, while long DNA induces spherical-like packing. For cubes, we find that the system transitions from one

cubic phase to another by breaking symmetry into a tetragonal phase. This is due to deformation of the colloids' DNA shells.

Chapter 5 presents kinetic Wulff shapes obtained from growth of hexagonal AB_2 type crystals, which grow in long hexagonal prisms. Unlike usual kinetic products, the shape is highly reproducible. We show that assembly into hexagonal rods happens due to energy barriers between different surface layers with identical Miller indices.

Chapter 6 presents a study on colloid crystal size obtained as a function of salt concentration. In particular, experiments find that the mean crystal size drastically increases when concentration is raised to 1M. Based on simulation results, we find that this is due to an increase of the attachment barrier between two colloids. This increase results in a slower attachment and nucleation rates, which effectively means that diffusion is faster. The interface-limited to diffusion-limited transition for individual colloids thus happens at a larger crystallite size, resulting in a faster growth of individual colloids at constant nucleation rate.

Chapter 7 introduces the concept of metallic bonding in self-assembled crystals. Previously studied crystals had defined positions for all colloids in the crystal. By mixing the usual colloids with much smaller ones (≤ 2 nm), we find that these small particles stop holding defined crystallographic positions and instead roam the crystals, similar to electrons in a classical metal. We define metallicity as translation entropy of small particles and explain system behavior with analogies from band structure of solid-state physics. We also find that there is a Mott-like transition of these particles with changes in temperature. At low temperatures, the electron condensates in defined crystallographic positions corresponding to complex metal alloys or intermetallics.

Acknowledgments

First and foremost, I would like to acknowledge the continued support throughout the years from my advisor, Prof. Monica Olvera de la Cruz. I have been very lucky in finding an advisor with whom I could build such a good relation and explore many different aspect of physics. I also want to thank the members of my committee, Prof. Erik Luijten and Prof. Chad A. Mirkin for taking the time to review this document; and also the good collaborative works with Prof. Mirkin.

I had excellent experimental collaborators from the group of Prof. Mirkin who I would like to acknowledge, in particular, Matthew O'Brien, Eileen Soyoung Seo, Anindita Das and Shunzhi Wang. Working with them got me to look at very interesting problems that I wouldn't had gotten the chance otherwise. It also led to very interesting discussions on how to connect simulations with experiments.

I would also like to thank the past and present members of the Olvera group, especially people I had collaborative works with, Trung Dac Nguyen, Jaime Millan, Yaohua Li, Meng Shen and Aykut Erbas. I also would like to acknowledge the early mentorship of Ting Li. A special mention for Annaliese Ehlen for reviewing the English of this work.

Last, I would like to acknowledge my parents for continued support throughout the years.

Table of Contents

List of Tables

List of Figures

CHAPTER 1

Introduction

The work in this thesis focuses on self-assembled crystals. We define these as structures that spontaneously assembles upon some external change such as cooling the samples. This approach is called bottom-up as we only design the colloids to be able to take a predefined structure. There are a few benefits from this, notably that we are free of lithography and fabrication scales very well. I explore various factors that influence the resulting crystals: particle shape, salt concentration in the solution and grafting number. These factors can be used to drive the resulting crystal lattices, habits or even to form metallic-like bonds. The tunability of our system let us continuously vary quantities that are discrete in atomic crystals such as metallic valency.

Colloidal crystals are assemblies of colloids (particles of size $1 - 100$ nm) into structures with a well defined periodicity. Colloids can be made out of many different materials, from metals like gold to polymers like polystyrene to proteins. They may also be coated with ligands, such as alkanes or other polymers.

While it is also possible to form glasses from these colloids, those are generally the result of fast kinetic processes which are extremely hard to reproduce with high fidelity. On the simulation side, glasses generally represent non-equilibrium systems with long relaxation times which are very hard to simulate properly and even harder to correctly relate to experiments.

Before I head in detailed discussions, it is worthwhile to address the issue of *why*. After all, colloidal crystals have been around for a long time, studied by Langmuir in [**2**] and evidently the appearance of crystals is not the main discovery here. Rather, the main focus of high information

polymers is *how*, as we are interested in creating colloidal crystals with some specific properties. These may be varied, but typically are composition, symmetry and lattice spacing. This kind of problem, where we have prescribed an end result, is known as an inverse problem. They are typically much harder than direct problems; figuring out if some colloids will assemble is easier than determining which kind of colloid will assemble into a specified structure.

Overall, we can distinguish two general goals in building these crystals. The first is from an engineering point of view and relates to where we can actually use these crystals. This is typically tied to to optical properties, for which I provide a general description later on in this chapter. A general statement is that optical properties of these crystals are dependent on the lattice and internal composition. The second goal is much more fundamental and relates to understanding the physical foundations of crystal formation. This is particularly true for the crystal lattices corresponding to complex metal alloys or intermetallics. In the atomic variant of these systems, it is not clear at all why they form in the first place. Considering that they appear in self-assembled systems, the dna-guided assembly platform may be suitable as a testing platform. We can directly tune valency, particle size, interaction strength in our system, while atomic systems are limited by the available elements.

1.1. High-information polymers

This work focuses on assembled structures of colloids coated with high-information polymers, but we still have to define what they are and why they are interesting. For the scope of this thesis, we will define as high-information any polymer which is composed of multiple monomer types, each of which has only a single other monomer type to which it can bind. We also require that each of the monomers have at most a single bond at any given time. The classical case, DNA is a chain of alternating sugars and phosphates. Each sugar unit is bonded to a nucleic base, denoted by A,

T, C or G, where the pairs AT and CG can form, but any other pair does not. The other archetypal case is ribonucleic acid, a similar polymer where an extra hydroxyl group is present in the sugar and the T base is replaced by U. We will exclude polypeptides, polymers composed of 21 different amino acid monomers, as interactions between different monomers are not highly specific.

High information polymers are used for their specific interactions. The binding energy of different colloids can be precisely controlled. For instance, in a ternary mixture of colloids A, B and C grafted with different DNA sequences, we can independently tune the interactions A-B, B-C and A-C. This control leads to tunable melting temperature as it is directly linked to the binding energy.

With this in mind, we can use these polymer grafted colloids to either tackle the inverse problem of constructing crystals with specific properties or study the fundamentals of crystal formation. Control over interactions and lack of quantum behavior of the building blocks render high information polymers a spectacular platform for looking at physics of crystals. In particular, we demonstrate in chapter 7 that self-assembled systems can show behavior akin to Mott transitions observed in regular solids. Unlike atomic metal-insulator transitions, this is a localization of colloids in specific lattice sites corresponding to intermetallic phases.

1.2. Previous work in self-assembled systems

As mentioned before, self-assembled systems of high-information polymers have been made before. The first realization of single crystals is already a few years old [**3**], but it is worthwhile to go over the basic science that allows us to assemble artifical crystals. In the DNA-guided assembly, colloids are coated with DNA strands, which are composed of a double-stranded region in the middle capped by two single-stranded regions (see figure 1.1).

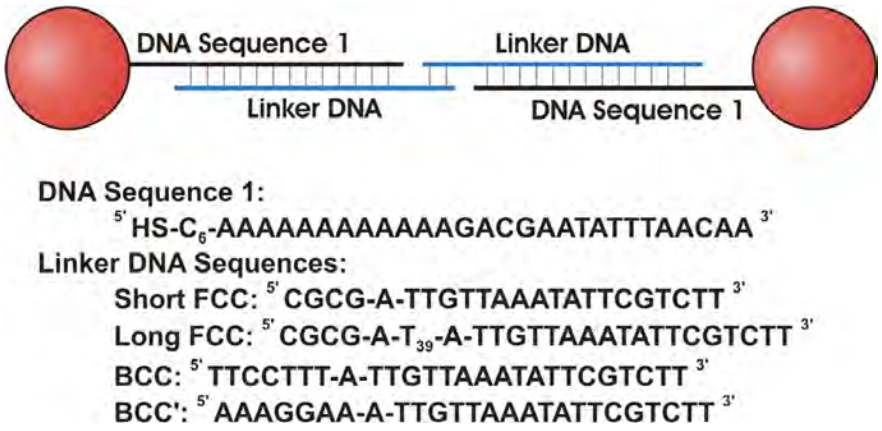

Figure 1.1. DNA sequences used in used in [**1**]. AuNPs were functionalized with 58 $\pm$ 5 (10-nm AuNPs) or 12 $\pm$ 3 (5-nm AuNPs) strands of DNA Sequence 1, linked via a 5' hexyl-thiol moiety. Crystals were formed via the addition of linker sequences with a 3' end complementary to the Au-bound DNA, a single flexor base used to increase DNA strand flexibility, and a 5' end that is either self-complementary (FCC crystals) or non-self-complementary (BCC crystals). Figure reproduced from [**1**]

The single-stranded sequence near the end (sticky end) can be chosen to be complementary to itself (single component, self-complementary systems) or to another sequence (binary systems). When the temperature is dropped below the melting point of the sticky end, strands from two different colloids hybridize leading to crystallization of the system. In order to obtain single crystals, the cooling rate has to be slow enough to allow for rearrangements of building blocks [**3**]. Rapid cooling leads to either multigrain aggregates or glassy materials. Single crystals made of building blocks differing only by the sequence of their sticky ends form shapes dictated by equilibrium Wulff construction. This construction method is a minimization of the surface energy of a crystal at a fixed volume. For instance, the binary system of [**3**] forms BCC lattices which crystallizes in rhombic dodecahedrons.

Self-complementary spheres do not show much tunability as only the ratio between DNA length and particle core size can be changed. Nevertheless, two distinct regimes are observed. For short DNA, the spheres crystallize into close packed structures (FCC) to maximize enthalpy.

For long and flexible DNA chains, the structure assembled is controlled by the entropy of chains grafted. This entropy corresponds to a maximization of the free volume of the chains and keeps the DNA brush on the surface as spherical as possible. This induces a transition from FCC to BCC [**4**]. This regime has not been fully explored for the binary systems at this point.

The phase diagram for binary spherical nucleic acid coated particles is published [**5**]. Unlike self-complementary particles, binary system offer control over particle size ratios as well as DNA grafting number ratio. Phases obtained are generally understood through maximization of hybridization in the system. For this reason, binary systems can assemble into a variety of different crystal phases ranging from BCC to Cr_3Si. One should note that all binary phases obtained from spherical particles are of very high symmetry: with the exception of AB_2 type lattices, they are all cubic.

In order to further expend the number of available lattices, the next step is to use anisotropic building blocks. This has been made possible by advances in synthesis of monodisperse particles [**6, 7**]. Early experiments using gold particles have shown potential control over crystal lattice by use of these anisotropic building blocks [**8**]. A systematic study of polyhedral anisotropic building blocks constitutes a chapter presented further on in this thesis. Other types of anisotropic building blocks include proteins where very specific sites on the surface can be coated with DNA[**9**].

Epitaxy is another technique that we can borrow from atomic crystal growth. In regular crystals, this refers to growth of a crystal on top of another crystalline substrate. Many variants of the technique exists (see [**10**] for a complete description), but the relevant ones are liquid phase epitaxy and molecular beam epitaxy. The first is a fairly old technique, commonly used in industry to grow ternary or quaternary compounds on top of gallium arsenide substrate. The second achieves growth by flowing atoms onto a substrate at very low pressure. While the assembly of colloids is done in liquid phase (water), the concentration of particles in solution is low and thus the process is similar

to molecular beam epitaxy (MBE). For instance, pressure can be controlled by the concentration of colloids in water just as in MBE but, as in liquid phase epitaxy, temperature of the substrate and colloids cannot be controlled independently. In our colloidal system, our substrates can be patterned with posts emulating a crystal surface and coated with DNA strands. Regular particles with complementary strands can then be added to the solution, enabling a layer-by-layer growth in liquid phase [**11**]. This makes epitaxy a convenient tool to study crystallization processes as dynamics of the colloids are much slower and easier to probe than regular atoms. However, additional differences arises due to the soft coating. The resulting crystal tolerates very high lattice mismatch, for instance in [**12**], and requires films to be "stapled" to achieve growth of multiple layers (see [**11**]).

On the simulation side, my predecessors and others have built viable coarse-grained models for these systems [**13, 14**] and conducted many simulations showing quantitative agreement with experimental results [**14, 3**], yielding a high degree of confidence in these models. For systems containing explicit ions (well defined positions for ions), other developed models can be used with high confidence in the results [**15, 16**]. I did not have to develop any force-fields since existing models were sufficiently good for our purposes.

1.3. Electromagnetism and tailoring optical properties in periodic solids

These crystals can be made relevant for many applications by tailoring interactions with light. Optical modes are usually calculated in the first cell of reciprocal space, the Brillouin zone, as it is sufficient to describe all available modes. Any strong interaction between light and the periodic lattice must take place near a high symmetry point, excluding the limit $\omega \to 0$ near the Γ point. For light propagating in periodic solids we can distinguish two relevant regimes. Denoting the light wavelength by λ and lattice spacing Λ, these regimes are $\Lambda \ll \lambda$ and $\Lambda \sim \lambda/2$.

The regime $\Lambda \ll \lambda$ produces what is known as effective materials. In this regime, the Brillouin zone is infinite and light does not interact with the lattice, only with the mean value of the constituents. The whole systems behaves just as if the permittivity, $\epsilon(\vec{r})$, is constant throughout the crystal. For visible light wavelengths ($\lambda \sim 800$ nm), atomic crystals fall in this category as they have lattice spacing on the order of a few ångströms. In this regime, defects are not important unless they have correlation lengths on the order of λ. The actual value of ϵ (or μ) can be tailored by the individual responses of the building blocks as was demonstrated by Pendry in [**17**], who used open ring resonators to build a material where μ takes negative values. In self-assembled systems, individual building block shapes that have been produced experimentally are limited to somewhat regular polyhedrons and are relatively far from the complex shapes required to obtain resonant building blocks. Usage of multicomponent crystals with complex lattices could be used to replicate the resonant building blocks, but this would require a significant expansion of the available set of crystal lattices.

The other available regime, $\Lambda \sim \lambda/2$ corresponds to photonic crystals. In this regime, the optical response can be fully tailored, even forbidding entire frequency bands from propagating in the solid (optical bandgap). The system responds to any defect of the lattice, which can be engineered to further alter light-matter response by making them concentrate optical fields (resonant defect). However, this comes at the cost of extreme sample delicacy during fabrication. A misplaced building block also acts as a defect, which means that the phonons in these systems are problematic due to the small spring constant. At the time of writing this thesis, I have not found any highly resonant defect used for light-matter interactions in self-assembled crystals. However, usage of high density of states near band edges has been used in colloidal systems [**18**].

The final crystal shape (crystal habit) can further be used as a resonator. This resonance has been demonstrated experimentally in DNA-guided assembly [**19**] from metallic building blocks

(plasmonic response). Rod shaped crystal habits are suitable targets as they support whispering gallery modes, which typically have high quality factors. In chapter 5, we demonstrate assembly of a hexagonal rod which should support similar modes. This path should be further explored, particularly in combination with tailoring the dielectric constant.

1.4. Outline of this thesis

In this thesis, I study two classes of problems relating to colloidal crystals: those arising in the modeling itself and those related to physics of self-assembly. The first class of problems relate to simplifying the description of interactions to increase calculation speed. For example, a set of interacting DNA-coated spheres might be treated as possessing a single radial interaction between different spheres. This process, which is known as coarse-graining, must be done carefully in order to avoid spurious results arising from oversimplification. Good coarse-graining schemes are a requirement for efficient calculation of physical and experimental systems. One article and one work in progress will be presented on this topic. One deals with coarse-graining anisotropic bodies. The other deals with strong deformation of the polymer shell due to interactions between colloids, which leads to strong multi-body effects [**20, 21**].

The second class of problems is related to physical phenomenon. In this thesis, these problems are tackled in collaboration with experimentalists from the group of Prof. C. A. Mirkin. I will present four articles in this part that address some of the issues mentioned earlier in this chapter. These articles explore changes in properties related to particle shape, salt concentration and number of grafted strands.

The first article is a systematic study of self-assembled regular polyhedrons for various DNA coating lengths. As expected, short strands produce compact lattices dictated by particle anisotropy,

while long strands induce spherical-like behavior of the colloids. For cubes, we find that the transition goes through a broken symmetry regime. Both the short strand phase (simple cubic) and long strand phase (face-centered cubic) as well as the particle core possess cubic symmetry. Near the transition however, this is broken into a tetragonal lattice. This is investigated by a combination of experiments and molecular dynamics simulations.

The second article presents kinetic Wulff shapes, which are out of equilibrium but highly reproducible. These appear due to significant energy barriers between different crystal planes with identical Miller indices. This is probed using experiments and molecular dynamics and kinetic Monte Carlo simulations. The paper is in preparation to be submitted to Nature Communications.

The third article relates an increase in mean crystal size to salt concentration in water. Using molecular dynamics simulations we show that there is an increase in attachment barriers between colloids at elevated salt concentrations. This barrier causes a slowdown of the attachment process in crystal growth. Using classical nucleation theory, we show that this slowdown causes each crystal to undergo the interface- to diffusion-limited transition at larger crystal size and thus that average crystal size increases. This paper is in preparation to be submitted to ACS central.

The last chapter presents work done in mixtures of small and large particles. In this system, there is a very large size different between the colloids (5:1 ratio). In regular systems, each colloid has a relatively large number of linkers grafted to it ($\geq$30). This leads individual colloids to behave as the average, due to the central limit theorem. For our small colloids (< 2 nm, < 10 strands), the very low number of strands grafted on them means that the number of hybridized strands can be very far from the average value of hybridized strands on small colloids. They can thus be completely dissociated and move from site to site in the crystal. Unlike the previously formed compounds, these are metallic in nature. As the temperature is lowered, the smaller particles

crystallize in specific lattice sites corresponding to intermetallic lattices. We intend to submit this work to Science.

A general conclusion will follow the presentation of the articles.

Part 1

Modeling polymer-coated anisotropic bodies

Modeling physical systems using simulations requires calculations to be done on the scale of the physical system. For instance, if we want to compute properties of a self-assembled system of 10 nm colloids, the system size needs to be somewhat larger than a few crystal periods. This can require representation of millions of atoms. Computing properties from ab-initio quantum mechanics is simply not feasible. The first approximation one will do is to remove electrons and represent atoms based on their bonding state. For example, a free carbon atom will not behave in the same way a carbon in a propane chain does. Further reductions in the number of degrees of freedom can be achieved by grouping atoms together. The first removed atoms are hydrogens: they are small and oscillate around their bonds much faster than heavier atoms, thus requiring smaller timesteps to capture their motion. This leads to united atoms models, where non-polar hydrogens are grouped on their carbon. At this point, the calculations are still called atomic.

One enters the coarse-grained regime upon further grouping of atoms. This can be done in various ways. For simple polymers like polystyrene sulfonate (carbon chain with sulfonated benzene sidegroups), individual degrees of freedom (DoF) can be chosen to represent two carbons, benzene rings and sulfonates [**22**], while the solvent (water) is not included explicitely in the model. The DoF obtained in this way are usually called beads. The removed DoF are the fast ones, hydrogens, internal bonds in the beads and so forth, while the leftover DoF are slow, representing movement of multiple atoms. There are multiple techniques that currently allow one to go from atomic to coarse-grained descriptions which can be found in the literature [**23, 24**] and the reader might be wondering why we want to revisit coarse-graining schemes. When one coarse-grains at very high levels, for say spherical colloids, the interaction is assumed to be spherically symmetric [**3**]. This is usually called a potential of mean force or effective potential and can be derived in various ways. However, if the polymer coverage is fairly low, the coating can deform during assembly, leading to multibody interactions [**21, 20**]. Currently, there are no coarse-grained methods to calculate this

deformation efficiently in simulations. The typical solution is to include all the ligands, which is fairly slow to simulate. We are interested in large-scale deformations, which are slow compared to movement of individual beads or chains of beads and the question is whether we can we approximate the interaction between colloids as a spherical interaction, plus a few anisotropic corrections. For this to happen, we first need a description of general interacting anisotropic bodies. This is shown in the chapter 2 of this thesis, which is a paper published in Physical Review E. In chapter 3, we demonstrate the full multibody interaction potentials. This is currently a draft in progress.

CHAPTER 2

Orbitals for classical arbitrary anisotropic colloidal potentials

Authors : Martin Girard, Trung Dac Nguyen, Monica Olvera de la Cruz

2.1. Abstract

Coarse-grained potentials are ubiquitous in mesoscale simulations. While various methods to compute effective interactions for spherically symmetric particles exist, anisotropic interactions are seldom used, due to their complexity. Here, we describe a general formulation, based on a spatial decomposition of the density fields around the particles, akin to atomic orbitals. We show that anisotropic potentials can be efficiently computed in numerical simulations using Fourier-based methods. We validate the field formulation and characterize its computational efficiency with a system of colloids that have Gaussian surface charge distributions. We also investigate the phase behavior of charged Janus colloids immersed in screened media, with screening lengths comparable to the colloid size. The system shows rich behaviors, exhibiting vapor, liquid, gel and crystalline morphologies, depending on temperature and screening length. The crystalline phase only appears for symmetric Janus particles. For very short screening lengths, the system undergoes a direct transition from a vapor to a crystal upon cooling; while, for longer screening lengths, a vapor-liquid-crystal transition is observed. The proposed formulation can be extended to model force fields that are time- or orientation-dependent, such as those in systems of polymer-grafted particles and magnetic colloids.

2.2. Introduction

Efforts to synthesize and assemble anisotropic particles such as Janus particles [**25, 26, 27, 28, 29**], patchy colloids [**30, 31**], polyhedral particles [**32**] and functionalized polyhedral nanoparticles [**33**] have led to materials with diverse structures and functionalities. Systems described by and modeled on anisotropic interactions also include proteins [**34, 35, 36, 37**] and polyhedral colloids [**38, 39, 40, 41**]. The anisotropy of the interaction field is akin to that of the electron orbitals of individual atoms or molecules, and could enhance control of structural properties such as that of the crystal lattices formed [**37, 33**].

Simulations can guide experimental attempts to self-assemble systems with anisotropic interactions. While state of the art simulations are often effective at both the micro (particle-based description) and macro (continuum) scales, they frequently fail at the mesoscopic scale, where macroscopic equations become invalid and the number of particles is too large for efficient computation. Coarse-graining circumvents this problem by reducing the number of degrees of freedom. For instance, the interactions of spherical colloids are generally rewritten as a function of the distance between the spheres only, discarding fine details such as surface roughness and the explicit nature of grafted chemical components. For non-spherical colloids of arbitrary nature, one must take into account the relative orientation of the colloids. The single degree of freedom for two spherically symmetric colloids then becomes six degrees of freedom.

All-atom molecular force fields encounter similar problems for rigid molecules, where fast calculation of interaction potentials is sought [**42**]. An expansion into spherical harmonics for potentials of the form r^{-a} was explored, which yields products of spherical harmonics and hypergeometric functions. Sack attacked the problem of arbitrary interactions between sites [**43**],

but could not obtain any explicit form. Ruedenberg used properties of Fourier transforms to reformulate the problem as an integral representation [**44**]; however, in numerical implementations, calculating hypergeometric functions is prohibitively expensive. A few other approaches that do not involve spherical harmonics have been attempted, such as expressing excluded-volume interactions in liquid crystals using the Gay-Berne potential and subsequent refinements [**45, 46**], and using potential decomposition for lock-and-key systems [**47**]. However, a general description of arbitrary potentials remains elusive. The common solution is to use brute force calculation, where the surface is tessellated with particles and some not necessarily physical interaction is used between surface particles.

Here, we revisit this problem for the general case of arbitrary bodies. We expand interactions into orbital-like interactions which are efficiently evaluated by Fourier transforms in the spirit of Ruedenberg [**44**]. Previous approaches aimed at obtaining analytical formulations require solving an integral and evaluating computationally expensive functions. We avoid explicitly computing these integrals by relying on tabulations of Fourier integrals and their full derivatives. Our approach is equivalent to *ab initio* Molecular Dynamics (AIMD) where the amplitudes are replaced by densities [**48**]. The numerical implementation avoids the Pulay forces which plague traditional AIMD. This orbital expansion is truncated at some appropriate level, which effectively smooths the particle description and produces expressions closely related to classical multipole expansions. We implement this potential in the LAMMPS software package [**49**] and provide a simple implementation for the uniaxial case (See Supplemental Material at [URL will be inserted by publisher] for implementation details).

The method requires two conditions: 1) that the orbital expansion of a particle is time invariant (that is, the particle shape does not change over time), which is a reasonable approximation for colloids grafted with a very dense brush and for rigid bodies with charges on the surface, and

2) that the interaction potential possesses a Fourier transform. A large set of potentials satisfy this second requirement, including Coulomb, Yukawa and Gaussian potentials; whereas the well-known Lennard-Jones potential does not, due to its rapidly divergent excluded volume term at $r = 0$. Excluded volume interactions can be resolved, for example, by using a Gaussian force, a technique used in mean field theories [**50, 51, 52**].

We first introduce the method and a numerical implementation (Section 2.3). We derive the field representation for a system of colloids interacting through a Gaussian surface charge distribution and for a system of charged Janus particles in a screened environment. For the Gaussian charged particles, for which the multipole expansion terminates, we show that this method is exact and thus has improved accuracy compared with a naive tessellation of the surface (Section 2.4.1). For the charged Janus particles (Section 2.4.2), which was previously examined using a Kern-Frenkel potential valid only at very short screening lengths [**53**], we extend the calculation to higher screening lengths, which is a regime typically difficult to access numerically. The limitations of the method are also discussed (Section 2.4.3).

2.3. Field representation of pairwise potentials

2.3.1. Motivating example

Consider a system of charged particles interacting through a screened Yukawa potential. We assume that particle i is located at $\vec{r}_i$ with orientation $\hat{R}_i$. Let $\rho(\vec{r}, \hat{R})$ be the distribution of interacting particles and $\chi(r)$ their interaction potential. $\chi(r)$ must possess a Fourier transform; otherwise, it has no restriction. In the case of charged particles interacting through a Yukawa potential, $\rho_i(\vec{r} - \vec{r}_i, \hat{R}_i)$ is the charge distribution and $\chi_{es}(r) = r^{-1}\exp(-\kappa r)$. The interaction is given by the integral:

$$U_{ij}^{es}(\vec{r}_i, \hat{R}_i, \vec{r}_j, \hat{R}_j) = \int_V \rho_i(\vec{r}, \hat{R}_i) d\vec{r} \int_{V'} \chi_{es}(|(\vec{r} - \vec{r}' - \vec{r}_{ij}|) \rho_j(\vec{r}', \hat{R}_j) d\vec{r}', \tag{2.1}$$

where $\vec{r}_{ij} = \vec{r}_j - \vec{r}_i$ and the coordinates are centered around the two colloids i and j. The second integral in Eq. 2.1 is a convolution of ρ_j with χ_{es}, which we introduce as the auxiliary field Φ_ρ,

$$\Phi_{\rho_j}(\vec{r}, \hat{R}_j) = \int_{V'} \chi_{es}(|\vec{r} - \vec{r}'|) \rho_j(\vec{r}', \hat{R}_j) d\vec{r}' = \rho_j(\vec{r}, \hat{R}_j) * \chi_{es}(r), \tag{2.2}$$

where $*$ denotes the convolution operation. The electrostatic potential energy between the colloids is then rewritten as the overlap integral of the auxiliary field with the density field as:

$$U_{ij}^{es}(\vec{r}_i, \hat{R}_i, \vec{r}_j, \hat{R}_j) = \int_V \rho_i(\vec{r} - \vec{r}_i, \hat{R}_i) \Phi_{\rho_j}(\vec{r} - \vec{r}_j, \hat{R}_j) d\vec{r}, \tag{2.3}$$

where we expanded the auxiliary field around the center of the colloid j for symmetry considerations that will become clear later. While the density $\rho(\vec{r}, \hat{R})$ and interaction $\chi(r)$ fields are scalar, generalization to tensor fields is straightforward, as shown for the vector case in Appendix C.

2.3.2. Field equations

We now derive the general formalism for forces based on overlaps of fields. We consider two arbitrary fields $\Phi_i(\vec{r} - \vec{r}_i, \hat{R}_i)$ located near colloid i and $\Phi_j(\vec{r} - \vec{r}_j, \hat{R}_j)$ located near colloid j as we did in the previous section. In the case of electrostatic interactions, $\Phi_i(\vec{r} - \vec{r}_i, \hat{R}_i) = \rho_i(\vec{r} - \vec{r}_i, \hat{R}_i)$ and $\Phi_j(\vec{r} - \vec{r}_j, \hat{R}_j) = \Phi_{\rho_j}(\vec{r} - \vec{r}_j, \hat{R}_j) = (\rho_j(\vec{r} - \vec{r}_j, \hat{R}_j) * \chi_{es}(r))$. The overlap integral in which we are interested is given by

$$U_{ij}(\vec{r}_i, \hat{R}_i, \vec{r}_j, \hat{R}_j) = \int_V \Phi_i(\vec{r} - \vec{r}_i, \hat{R}_i)\Phi_j(\vec{r} - \vec{r}_j, \hat{R}_j)d\vec{r}. \tag{2.4}$$

We first rewrite the left-hand side of Eq. 2.4. Without making any assumptions on the particular shape of each particle or field, we have six degrees of freedom, three for the relative position of the second particle with respect to the first one, and three for the rotation of the second particle. To obtain completely symmetric forms suitable for molecular dynamics (MD), we treat the potential energy as having nine degrees of freedom, three for the center to center vector $\vec{r}$, three for the rotation of the first particle and three for the rotation of the second particle.

Without loss of generality, we can assume that the particle i is located at the origin. We note that Eq. 2.4 is very similar to the convolution integral treated by Fourier transforms [**54**]. Denoting the difference in colloid position by $\vec{r}_{ij} = \vec{r}_j - \vec{r}_i$ and geometrical inversion of $f(\vec{r})$ by $\underline{f}(\vec{r})$ such that $\Phi_j(\vec{r} - \vec{r}') = \underline{\Phi_j}(\vec{r}' - \vec{r})$, we cast equation 2.4 as the convolution of Φ_i and the inversion of Φ_j:

$$U_{ij}(\vec{r}_{ij}, \hat{R}_i, \hat{R}_j) = \int_V \Phi(\vec{r})\underline{\Phi_j}(\vec{r}_{ij} - \vec{r})d\vec{r} = \Phi_i(\vec{r}) * \underline{\Phi_j}(\vec{r}) \Big|_{\vec{r}=\vec{r}_{ij}} \tag{2.5}$$

Within the spherical harmonics transform framework [**54**], this operation is straightforward in reciprocal space, where $\vec{r} \to \vec{\rho}$, $\Phi(r, \theta, \phi) \to \tilde{\Phi}(\rho, \theta_w, \phi_w)$ is the Fourier transform operation, and $\tilde{U}_{ij}(\vec{\rho}, \hat{R}_i, \hat{R}_j) = \tilde{\Phi}_i(\vec{\rho}, \hat{R}_i)\tilde{\Phi}_j(\vec{\rho}, \hat{R}_j)$. We introduce the Wigner functions $\mathcal{D}^l_{m,\mu}(\hat{R})$ to treat the rotation of spherical harmonics, resulting in the full expressions for $\tilde{\Phi}_i$ and $\underline{\tilde{\Phi}_j}$ given by:

$$\tilde{\Phi}_i(\vec{\rho}) = \sum_{l_i,m_i,\mu_i} \mathcal{D}^{l_i}_{m_i,\mu_i}(\hat{R}_i) Y^{m_i}_{l_i}(\theta_w,\phi_w) F^{m_i}_{l_i}(\rho), \tag{2.6}$$

$$\underline{\tilde{\Phi}_j}(\vec{\rho}) = \sum_{l_j,m_j,\mu_j} \mathcal{D}^{l_j}_{m_j,\mu_j}(\hat{R}_j)(-1)^{l_j} Y^{m_j}_{l_j}(\theta_w,\phi_w) F^{m_j}_{l_j}(\rho). \tag{2.7}$$

The usual spherical harmonics $Y^m_l(\theta,\phi)$ are defined by

$$Y^m_l(\theta,\phi) = \sqrt{\frac{(l-m)!}{(l+m)!}} P^m_l(\cos\theta)\exp(im\phi),$$

where $P^m_l(x)$ is the associated Legendre polynomial of degree l and order m, such that $\int_\Omega Y^m_l(\theta,\phi)$ $Y^{m'}_{l'}(\theta,\phi)d\Omega = \delta_{l,l'}\delta_{m,m'}$. A useful representation of the Wigner $\mathcal{D}^l_{m,\mu}$ function is based on quaternion representation of rotations as developed in [**55**]:

$$\mathcal{D}^l_{m,\mu} = \sqrt{\frac{(l+m)!\,(l-m)!}{(l+\mu)!\,(l-\mu)!}} |R_a|^{2l-2m} R_a^{m+\mu} R_b^{m-\mu} \sum_\rho \binom{l+\mu}{\rho} \binom{l-\mu}{l-\rho-m} \left(-\frac{|R_b|^2}{|R_a|^2}\right)^\rho \tag{2.8}$$

where $R_a = q_w + iq_z$ and $R_b = q_y + iq_x$ and $q = (q_w, \vec{q})$ is a normalized quaternion describing the orientation. The quantities F^m_l are the l^{th} order spherical Fourier-Bessel transforms of $\Phi(\vec{r})$ given by:

$$F^{m_i}_{l_i} = 4\pi(-i)^{l_i} \int \Phi_i(\vec{r})\overline{Y^{m_i}_{l_i}(\theta,\phi)} j_{l_i}(\rho r) r^2 dr \tag{2.9}$$

where $j_l(z)$ is the l^{th} order spherical Bessel function of the first kind. Multiplying Eqs. (2.6) and (2.7) and inverting back the transform yields the potential:

(2.10)

$$U_{ij}(\vec{r}_{ij}, \hat{R}_i, \hat{R}_j) = \sum_{\substack{l_i,m_i,\mu_i \\ l_j,m_j,\mu_j,L}} 8(-i)^L Y_L^{m_i+m_j}(\theta_{ij}, \phi_{ij}) \mathcal{D}^{l_i}_{m_i,\mu_i}(\hat{R}_i) \mathcal{D}^{l_j}_{m_j,\mu_j}(\hat{R}_j) \mathcal{F}^{m_i,m_j}_{L,l_i,l_j}(r_{ij}) \mathcal{C}^{m_i,m_j}_{L,l_i,l_j},$$

where

(2.11)
$$\mathcal{F}^{m_i,m_j}_{L,l_i,l_j}(r_{ij}) = \left(\frac{i^{l_i+l_j}}{(4\pi)^2} \int_0^\infty F^{m_i}_{l_i}(\rho) G^{m_j}_{l_j}(\rho) j_L(\rho r) \rho^2 d\rho \right)_{r=r_{ij}},$$

(2.12)
$$\mathcal{C}^{m_i,m_j}_{L,l_i,l_j} = \sqrt{\frac{(2l_i+1)(2l_j+1)}{4\pi(2L+1)}} \langle l_i, 0, l_j, 0, L, 0 \rangle \langle l_i, m_i, l_j, m_j, L, m_i+m_j \rangle$$

and $\langle l_i, m_i, l_j, m_j, L, M \rangle$ is a Clebsh-Gordan coefficient. This definition of $\mathcal{C}^{m_i,m_j}_{L,l_i,l_j}$ is equivalent to the Slater coefficients of [**54**]. In the general case, there is no known analytical representation of $\mathcal{F}(r)$, and it must be tabulated.

2.3.3. Numerical implementation

The coefficients $\mathcal{F}^{m_i,m_j}_{L,l_i,l_j}(r_{ij})$ are precomputed and compiled into tables. This can be done using known software packages (see provided files) or by fast Fourier-based methods [**56**]. For Monte Carlo simulations, potential energy given by Eq. 2.10 is sufficient for sampling. In order to time evolve the system in MD simulations, we must compute forces and torques. In Eq. 2.10, the position and rotation components are fully decoupled. Forces are given by spatial derivatives, while torques are given by angular derivatives of the Wigner functions. We tabulate the derivative of $\mathcal{F}$ using:

$$\frac{\partial \mathcal{F}_{L,l_i,l_j}^{m_i,m_j}}{\partial r} = \frac{i^{l_i+l_j}}{(4\pi^2)} \left(\int_0^\infty F_{l_i}^{m_i}(\rho) G_{l_j}^{m_j}(\rho) \left(\frac{L j_L(r\rho)}{r} - \rho j_{1+L}(r\rho) \right) \rho^2 d\rho \right)_{r=r_{ij}}. \tag{2.13}$$

Additional forces arise from the derivatives of the spherical harmonics. Their projection along direction k is calculated by using partial derivatives,

$$F_k \sim \frac{\partial Y_L^M(\theta,\phi)}{\partial \theta} \frac{\partial \theta}{\partial k} + \frac{\partial Y_L^M(\theta,\phi)}{\partial \phi} \frac{\partial \phi}{\partial k}. \tag{2.14}$$

Partial derivatives of the spherical harmonics are obtained by either multipling by iM or taking the derivative of the associated Legendre polynomial. In practice, since spherical harmonics are polynomials of $\cos(\theta)$, we simply calculate

$$F_k \sim \sqrt{\frac{(l-m)!}{(l+m)!}} \exp(iM\phi) \frac{\partial P_l^m(\cos\theta)}{\partial \cos\theta} \frac{\partial \cos\theta}{\partial k} + iM Y_L^M(\theta,\phi) \frac{\partial \phi}{\partial k}. \tag{2.15}$$

The force can then be computed by addition of all individual contributions. For instance, the $\hat{x}$ component is given by

$$F_x = \frac{\partial \mathcal{F}_{L,l_i,l_j}^{m_i,m_j}}{\partial r} \frac{x}{r} + \frac{\partial U}{\partial \cos\theta} \frac{-2xz}{r^3} + \frac{\partial U}{\partial \phi} \frac{-y}{x^2+y^2}. \tag{2.16}$$

In order to compute torques, we must take derivatives with respect to infinitesimal rotations along some set of axes. The composition of two rotations, $\hat{R}_1$ and $\hat{R}_2$, with corresponding quaternions q_1 and q_2, is given by the quaternion product $q_2 \cdot q_1$. This relation is used to obtain the

variation of the quaternion of a particle with respect to a rotation axis. For instance, a rotation along the $\hat{x}$ axis of the referential frame, u_x, will cause a variation in quaternion given by

$$\frac{\partial q}{\partial u_x} = \frac{1}{2}(0,1,0,0)\cdot(q_w,q_x,q_y,q_z). \tag{2.17}$$

The result is multiplied by the partial derivatives of $\mathcal{D}^{l_j}_{m_j,\mu_j}(\hat{R}_j)$ in order to obtain the full derivative. For instance, the derivative of $\mathcal{D}^{l_j}_{m_j,\mu_j}(\hat{R}_j)$ against a rotation along the axis $\hat{x}$ is given by

$$\frac{\partial \mathcal{D}^{l}_{m,\mu}}{\partial u_x} = \sum_k \frac{\partial D^{l}_{m,\mu}}{\partial q_k}\frac{\partial q_k}{\partial u_x} = -q_x\frac{\partial \mathcal{D}^{l}_{m,\mu}}{\partial q_w} + q_w\frac{\partial \mathcal{D}^{l}_{m,\mu}}{\partial q_x} - q_z\frac{\partial \mathcal{D}^{l}_{m,\mu}}{\partial q_y} + q_y\frac{\partial \mathcal{D}^{l}_{m,\mu}}{\partial q_z}. \tag{2.18}$$

The Wigner coefficients $\mathcal{D}^{l_j}_{m_j,\mu_j}(\hat{R}_j)$ are calculated directly from quaternions (see Eq. 2.8), providing straightforward implementations in MD packages. Since these coefficients and their derivatives are only dependent on individual particle orientations, they are updated once per timestep and not for each pair interaction. In principle, one can invert the multiplication order to obtain the torques in the body frame. This removes the μ_i index from the summation in Eq. 2.10 but requires calculating the Wigner functions once per pair interaction, instead of once per particle. It is not done in the supplied code as it would complicate the LAMMPS implementation without any obvious benefit in computational performance.

2.3.4. Gaussian patchy particles

To test the method's accuracy, we consider a case where the series in Eq. 2.10 terminates and does not require truncation, resulting in a spherical harmonic representation that is exact. In particular, we examine colloids with surfaces interacting through a Gaussian potential $\chi_G(r) = a\exp(-br^2)$,

where a and b are parameters of the potential. In order for the series to terminate, we use a surface density $\rho_S(\vec{r}) = \delta(|\vec{r}|-1)(1+\cos\theta)$, that is, a distribution located on the surface of a particle with radius $R = 1$. The interaction energy between two colloids is written as

$$U_{ij}^{sph} = a \int \rho_i(S_i)\rho_j(S_j)\exp(-br_{S_i,S_j}^2)dS_i dS_j, \tag{2.19}$$

where S_i is the surface of particle i and ρ_{S_i} is a continuous function on the surface of particle i.

We compare the cases where this integral is evaluated using a numerical quadrature with the case where the exact field method is used. Using a numerical quadrature, the integrand is evaluated at N points on each surface, yielding

$$U_{ij}^{sph} = a(4\pi)^2 N^{-2} \sum_i^N \sum_j^N \rho(\vec{r}_i)\rho(\vec{r}_j)\exp(-b|(\vec{r}_i - \vec{r}_j)|^2) + \mathcal{O}(N^{-2}). \tag{2.20}$$

Figure 2.1. Representation of the surface function $\rho(S)$ for two interacting particles of arbitrary orientations, where blue indicates $\rho = 0$ and red indicates $\rho = 1$.

Eq. 2.20 can be directly evaluated in standard MD packages by tessellating the surface of a sphere and assigning charges to each point proportional to $q = (1+\cos\theta)/N$, where N is the number of points per sphere, as sketched by Fig 2.1. The points are chosen according to

a Fibonacci mapping in order to obtain an approximately equal area for each point [**57**]. The interaction between points of the tessellation is taken as $U_{ij}^{tess} = aq_iq_j \exp(-br^2)$.

For the field representation, the integral in Eq. 2.4 can be written using the product of two equal fields due to special properties of Gaussian functions (see Appendix B). These two fields are given by $\Phi_i(\vec{r}) = \Phi_G * \rho_i$, where $\Phi_G = a^{1/2}2^{3/2}\pi^{-3/4}b^{3/4}\exp(-2br^2)$, obtained by inverting the square root of the Fourier transform of $\chi_G(r)$. The overall field for this case is then given by

$$\Phi_i(\vec{\rho}) = \Phi_G * \rho_i = \frac{8a^{1/2}\pi^{7/4}\exp(-\frac{\rho^2}{8b})}{b^{3/4}}\left(\sqrt{\pi}Y_0^0(\theta,\phi)j_0(\rho) + \sqrt{\frac{\pi}{3}}Y_1^0(\theta,\phi)j_1(\rho)\right). \tag{2.21}$$

2.3.5. Screened Janus particles

Using this method, we can now extend our recent study of charged Janus particles immersed in an ionic solution [**53**] to the cases where the screening length is on the order of the particle radius. Janus particles possess two sides with equal, but opposite charge density. The cap angle, θ_m, dictates the fraction of the surface covered by each charge. This system was previously simulated using a Kern-Frenkel potential, which is valid for very small Debye lengths, that is, $\lambda \ll R$, where λ is the Debye length and R is the particle radius.

In electrostatically screened environments, the coupling is non-trivial. For instance, dipole-dipole and charge-charge interactions generate terms with the same distance dependence [**58**]. These effects are included in our method.

To calculate interactions between colloids when $\lambda \sim R$, we use Eq. 2.3. The charge density is given by the series:

$$\tilde{q}(\vec{\rho}) = -8\pi^{3/2}R^2\left(\cos\theta_m j_0(\rho R)Y_0^0(\theta,\phi) + \sum_{l=1}^{\infty}\sqrt{1+2l}\frac{P_l^1(\cos\theta_m)\sin\theta_m}{l(l+1)}j_l(\rho R)Y_l^0(\theta,\phi)\right). \tag{2.22}$$

In reciprocal space, the potential $\chi_{es}(r)$ is convolved with the charge density by a multiplication using $\tilde{\chi}_{es}(\rho) = 8\pi^{3/2}(\lambda^{-2} + \rho^2)^{-1}$. The series is truncated at $l_{max} = 3$ in order to be evaluated numerically and a purely repulsive truncated Lennard-Jones potential (i.e. the Weeks-Chandler-Anderson potential) is added to represent the solid cores of the colloids.

One quickly notices the similarity between Eq. 2.22 and the usual multipole expansion for charges. A proof of equivalence for $\lambda \to \infty$ is found in Appendix A. Using tabulated integrals over traditional multipoles presents a major advantage since the integral is well-defined in the overlapping regime when $|\vec{r}_{ij}| < R_i + R_j$.

2.4. Results and discussion

2.4.1. Accuracy and computational performance

We first characterize the computational efficiency and accuracy of the field respresentation for the Gaussian charged particles. We implement the field representation and the Gaussian charge potential as new force fields in LAMMPS. The benchmark runs are performed with equilibrated systems at similar thermodynamic state points, i.e., number of particles, temperature and density. LAMMPS is built with the stable 31Mar17 release.

Both the coarse-grained (Gaussian charge) and the spherical harmonic (field) representations achieve strong scaling performance for our numerical implementations, as seen in Figure 2.2. The spherical harmonic representation is generally faster than the surface bead representation by a factor of 2.0-3.5, depending on the resolution of the latter. Finer resolution of the surface bead representation increases the computational overhead as N^2, where N is the number of beads discretizing the surface. Furthermore, the spherical harmonic representation exhibits a parallel efficiency as high as 55% at 125 particles per MPI process. The particularly high parallel efficiency at low particle counts per MPI process, compared to other conventional pairwise potentials (such as

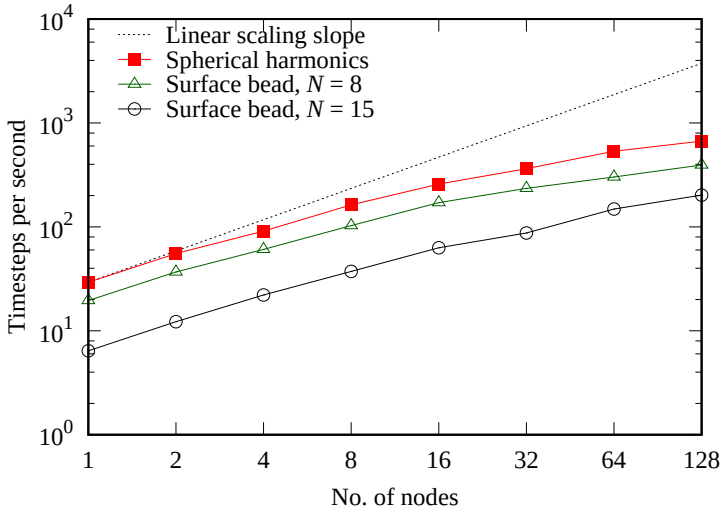

Figure 2.2. Strong scaling performance on the Titan XK7 supercomputer. The number of particles in each run is 32000. There are 16 MPI processes launched on each node.

Lennard-Jones and Yukawa potentials), implies that the field representation is computationally intensive and thus should further benefit from finer-grained parallelisms including GPU acceleration, as observed with Gay-Berne potentials [**59**].

For Gaussian patchy particles, the spherical harmonic representation is exact. Fig. 2.3 compares the average energies of the coarse-grain and field calculations as a function of the number of quadrature points N for a particle with radius $R = 1$ and volume fraction $v \approx 0.077$, using four sets of the potential parameters a, b. The slopes are approximately -2, indicating that the error of the coarse-grain simulation scales as $1/N^2$, consistent with Eq. 2.20.

Since the calculation speed of the coarse-grained simulations also scales as N^2, accuracy and computational efficiency must be balanced. For this specific system, very few points on the surface are required for accurate simulations. An accuracy of 1% of the mean energy of the system requires approximately 20 beads per surface. Even for this level of precision, however, the spherical harmonic potential method is faster than the coarse-grained representation. The calculation speeds become comparable only when $N \approx 6 - 8$. Finally, for the $a = 0.2, b = 2, N = 37$ case,

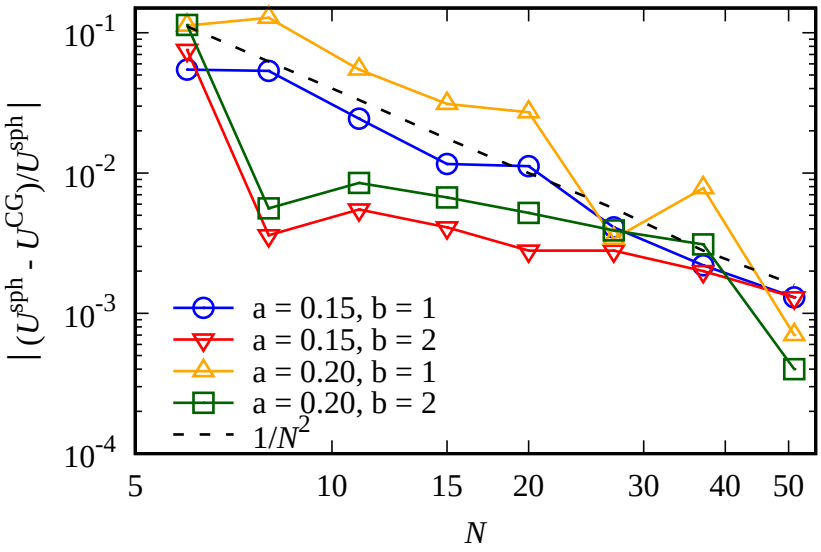

Figure 2.3. Relative error of the average energy of the system as a function of the number of tessellation points of the coarse-grained representation. Curves are plotted for $a = (0.15, 0.20)$ and $b = (1, 2)$. The system is in a liquid state with these parameters. An additional curve proportional to $1/N^2$ is drawn for comparison.

coarse-grained models achieve a calculation speed around 33 timesteps per second, compared to 652 timesteps per second for the spherical harmonic representation.

2.4.2. Janus particles morphologies

To characterize the phase behavior of Janus particles, we simulated particles with two opening angles ($\theta_m = \pi/2$ and $\theta_m = 1.40$) previously calculated using a Kern-Frenkel potential [**53**]. The simulations were run with 4000 colloids of radius $R = 1$ and a constant volume fraction of $v = 0.10$. The Debye length is varied over the range $0.16 \leq \lambda \leq 0.32$. The reduced temperature $T^* = \pi\epsilon k_B T R/2q^2$ is varied independently within $1.0 \leq T^* \leq 2.0$, where ϵ is the permittivity and q is the charge on one of the hemispheres of the balanced $\theta_m = \pi/2$ Janus particle. The system is equilibrated over 3×10^6 timesteps.

We observe four morphologies shown in Fig. 2.4. At very high temperatures, the system is in a vapor phase, labeled V. The system also exhibits a liquid state, labeled L, which seems to correspond to what we previously called a worm-like glass state in [**53**]. This liquid phase forms either very small droplets near the V / L boundary or elongated structures. This behavior is similar to that of hard dipole dumbbell systems [**60**], where it was observed that, while dumbbells with explicit charge or point dipoles exhibit a vapor-liquid transition, point dipole spheres do not [**61**]. Our simulations suggest that explicit charge representations of spheres also exhibit a vapor-liquid transition.

One should be careful making comparisons between Kern-Frenkel and the present orbital potentials. While they are both approximating the Yukawa potential, it is not the same approximation. Kern-Frenkel assumes that the charge density is locally constant (in a region which size depends on λ). The present orbital representation approximates it using a series. At the opening angle, Kern-Frenkel approximates the mean charge density as either $+1$ or -1 while the orbital gives a sine polynomial dependance. This has strong consequences for crystalline phases, which are very sensitive to the type of interaction used. For instance, crystal formed by colloids interacting through repulsive inverse power laws ($1/r^n$) will exhibit FCC-BCC transition around an exponent of $n \approx 6$ [**62**]. Due to these differences, we do not find that the crystal lattice match the previous calculations based on Kern-Frenkel. Nevertheless, the melting temperature of the crystal phase for $\theta_m = \pi/2, \lambda = 0.16R$, is around $T^* \approx 0.8$, which is similar to the critical temperature found in the work using the Kern-Frenkel approximation [**53**], where $T^* = 0.75$.

Interestingly, in the $\theta_m = \pi/2$ case, the liquid morphology only emerges for sufficiently large Debye lengths ($\lambda \gtrsim 0.20$) and sufficiently high temperatures. This phase was absent in our Kern-Frenkel simulations conducted at $\lambda = 0.16$. For very small Debye lengths or very low temperatures, it is replaced by a crystalline morphology. In all observed cases, the system first condenses

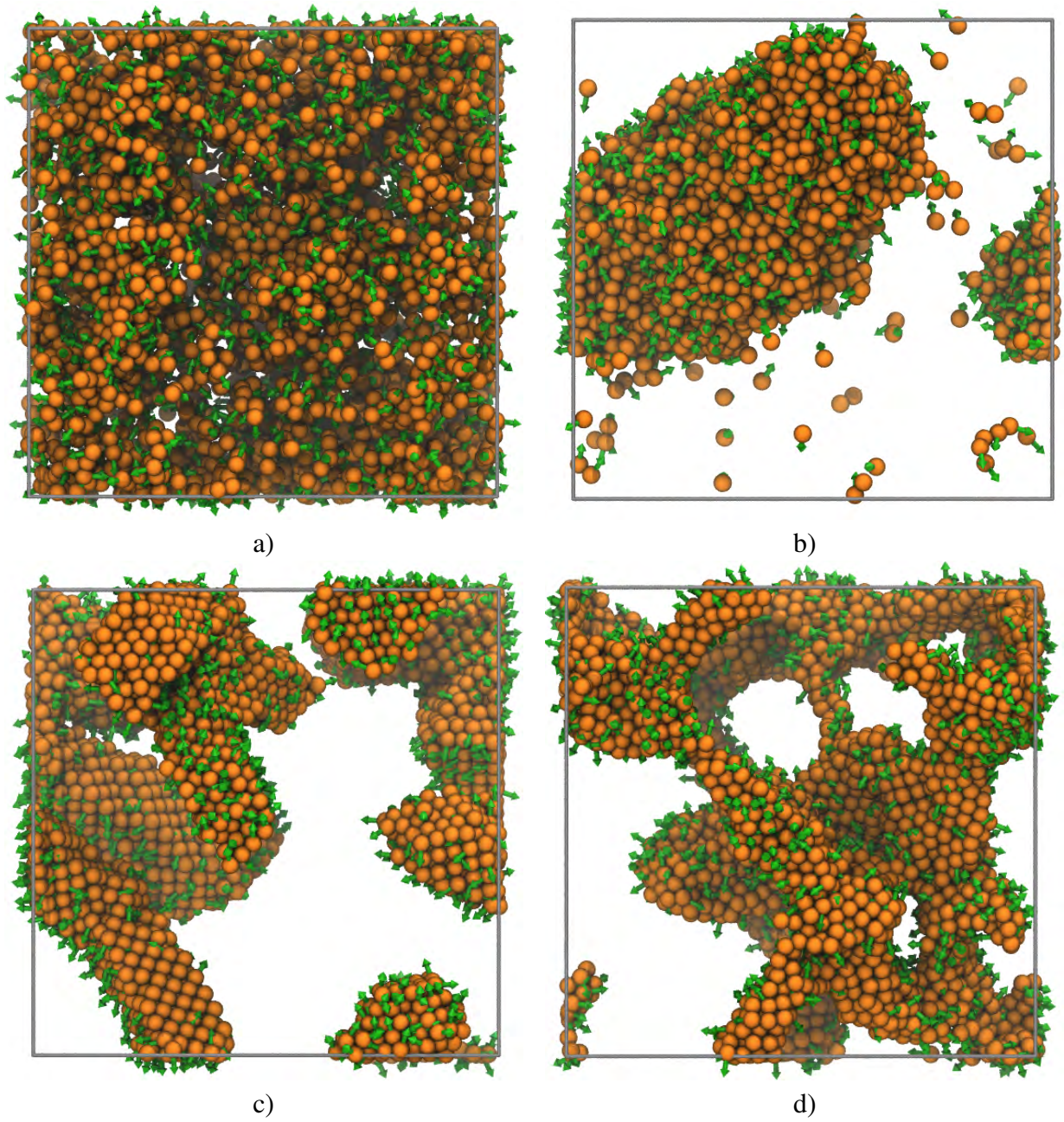

Figure 2.4. Snapshots of the simulations in different morphologies observed for symmetric ($\theta_m = \pi/2$) Janus particles a) Vapor V state at $T^* = 1.81$, $\lambda = 0.24$, b) Liquid L state at $T^* = 1.50$, $\lambda = 0.24$, c) Crystalline C state at $T^* = 1.20$, $\lambda = 0.24$, d) Gel state at $T^* = 1.0$, $\lambda = 0.32$. Arrows indicate north pole of the Janus particles.

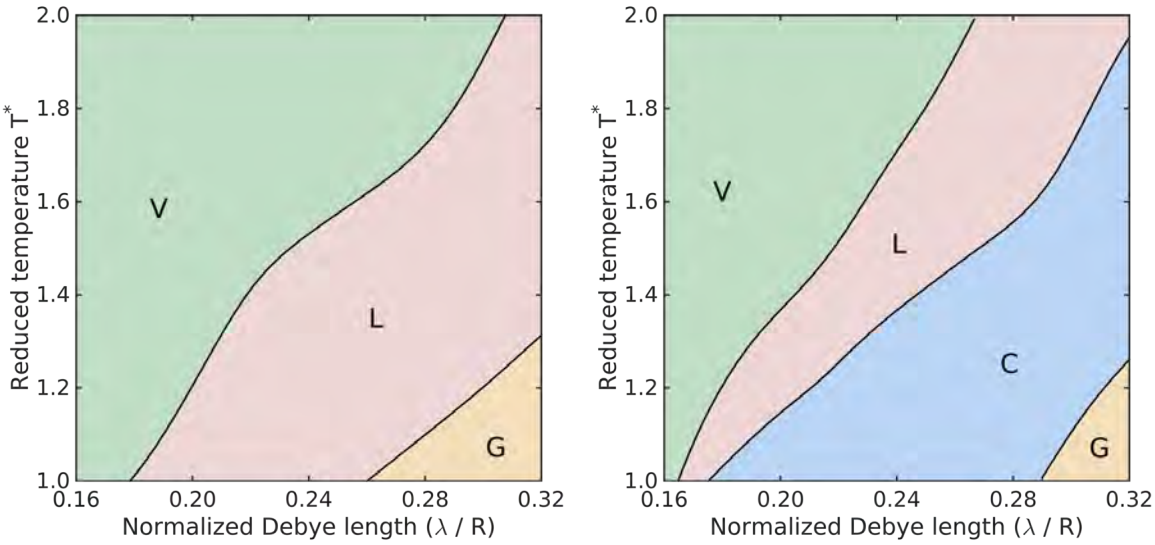

Figure 2.5. Regions of observed morphologies in simulations of charged Janus colloids for opening angles of a) $\theta_m = 1.40$ and b) $\theta_m = \pi/2$. The different morphologies indicate the main morphology observed. The phase is deemed as vapor by a clustering analysis if more than half the colloids are in clusters of size less than 50. Other morphologies are determined by visual inspection of the trajectories. A morphology is deemed crystalline if it forms at least one crystalline domain. Morphologies are determined for five values of λ and six ($\theta_m = 1.40$) or nine ($\theta_m = \pi/2$) values of temperature, totaling 30 simulated state points for $\theta_m = 1.40$ and 45 for $\theta_m = \pi/2$. Boundaries are obtained by drawing splines in between grid points of different morphologies and should be treated as a guide for the eyes. Coexistence of morphologies is often found along the boundaries.

to the L phase and then crystallizes. Consequently, multiple crystalline domains form on the elongated L structures, instead of single crystals. At large Debye lengths and low temperatures, the systems starts supporting thinner lines of colloids and the system forms a branched structure, eventually coalescing into a gel-like structure. Whether such a phase is thermodynamically stable or the result of kinetic traps is unknown. However, when $\theta_m = 1.40$, the system is liquid near the L / G boundary, which suggests a stable phase. We have performed additional simulations runs at this state point to confirm this hypothesis. More information on the liquid-gel morphology transition can be found in Appendix E.

2.4.3. Limitations of the method

As mentioned earlier, the current method has two limitations. First, the interaction potentials χ must possess a Fourier transform. A common source of soft potentials is excluded volumes, which diverge when the volumes overlap. While this is clear from the mathematical equations, the underlying physical reason lies with the fact that series truncation produces a spatial averaging of the densities. This averaging is inconsistent with systems that respond to infinite frequencies. To overcome this limitation, one may be able to represent excluded volumes by expanding Eq. 2.3 into a summation of integrals of powers of $\rho(\vec{r}, \hat{R})$ or by regularizing the potential function (see Appendix D for further details and derivations).

The second limitation is that density fields must be static in time, which makes the description unsuitable for system with strong deformations. Typical cases include colloids grafted with a low amount of flexible polymers. In such systems, when colloids come close to each other, the polymer coating may deform. In systems of DNA coated polyhedra, this has been shown to strongly affect broken symmetry regimes, driving transitions between different crystal lattices [**33**]. These deformations have been the starting point of the orbital topological model, which for polymer coated spheres predicts different equilibrium structures than a regular non-deformable potential [**63**]. In order to model such a system with our description, one would have to use a time-dependent density field and advance the field over time. We are currently working on such a model, which will be the subject of a future publication.

2.5. Conclusion

We have developed a field representation for describing the anisotropic interactions between colloids at mesoscopic scales based on an orbital-like decomposition. Using the field representation, several use cases are derived, including patchy particles and charged Janus particles. With

this approach, we demonstrate that charge-neutral Janus particles show qualitative agreement with studies of dipolar hard dumbbell systems. Interestingly, the vapor-liquid transition is supplanted by the liquid-crystal transition for very short screening lengths, yielding similar results from the Kern-Frenkel potentials. The liquid phase has previously been shown to be absent for point dipole spheres [**61**], which raises the question of whether it arises from inclusion of higher order hexapole terms or disapears at large Debye lengths. Addition of isotropic dispersion forces to systems of point dipole spheres has been shown to cause the liquid phase to appear, provided the dispersion force is sufficiently strong [**64**]. In our system, the additional hexapole force is entirely determined by the shape of the charges at the surface of the Janus particle. These particles are usually thought of as dipoles and whether the phase diagram can actually be controlled by the surface charge distribution remains an interesting question.

This technique enables simulations in solutions with screening lengths comparable to the size of the colloids without resorting to expensive and often inaccessible explicit ions simulations. The modest requirements for the type of potentials that can be used, make this field coarse-graining approach applicable to many types of interactions. With this flexibility, the technique could potentially be employed to calculate interactions between globular proteins of various shapes and surface compositions stemming from a combination of electrostatics and hydrophobicity. Indeed, our approach has the inherent capability of including position-orientation coupling of particles. It can in principle describe any anisotropic potential, as long as the potential has proper behavior in reciprocal space, and, in the present form, as long as the particles shape and surface composition remain constant as the particles interact.

In order to relax the assumptions made in the present study, namely that the density representing particle shapes is constant and that the surface composition does not change as the particles interact, the field coarse-graining approach has to be extended to directional and time-dependent

force fields. While the complexity of the derived field depends on the original interactions and increases with the target accuracy, the performance gain due to finer-grained parallelization can be significant and will be the focus of future studies. A major refinement is to include dynamic densities, which is necessary to efficiently simulate very soft colloids such as polymer-coated particles where the shape of the particle changes when two colloids interact [**63**]. This refinement is necessary also to make comparison between our approach and results of conventional approaches that include grafted chains such as DNA to nanoparticles explicitly [**33**].

Acknowledgement

This work was supported by the Center for Bio-Inspired Energy Science (CBES), which is an Energy Frontier Research Center funded by the U.S. Department of Energy, Office of Science, Office of Basic Energy Sciences under Award Number DE-SC0000989. MG acknowledges support from the Natural Sciences and Engineering Research Council of Canada (NSERC) for a graduate fellowship (grant PGS-D #6799-459278-2014).

A. Equivalence between multipole expansions

Eq. 2.22 expands the charge into spherical harmonics. Arbitrary rotations of this multipole are treated by Wigner $\mathcal{D}$ functions :

$$\tilde{q}_i(\rho) = -8\pi^{3/2}R_i^2\left(\cos\theta_m j_0(\rho R_i)Y_0^0(\theta,\phi) + \sum_{l=1,m}\mathcal{D}_l^{m,0}(\hat{R}_i)\sqrt{1+2l}\frac{P_l^1(\cos\theta_m)\sin\theta_m}{l(l+1)}j_l(\rho R_i)Y_l^0(\theta,\phi)\right). \tag{2.23}$$

When convolved with other charge distributions and the interaction potential, we get

$$U_{ij} = \sum_{L,M} 8i^{L-l_i-l_j} Y_L^M(\theta,\phi) \sum_{l_i,m_i,l_j,m_j} \mathcal{D}_{l_i}^{m_i}(\hat{R}_i)\mathcal{D}_{l_j}^{m_j}(\hat{R}_j)\mathcal{C}_{l_i,l_i,0}^{m_i,m_i,0}\mathcal{C}_{L,l_i,l_j}^{m_i,m_j} 8\pi^{3/2} c_{l_i} c_{l_j} \mathcal{I}_{L,l_i,l_j}, \tag{2.24}$$

where $\mathcal{I}$ is an integral defined by

$$\mathcal{I}_{L,l_i,l_j} = \int_0^\infty j_{l_j}(\rho R_j) j_{l_i}(\rho R_i) \frac{\rho^2}{\rho^2 + \lambda^{-2}} j_L(\rho r) d\rho. \tag{2.25}$$

To the best of our knowledge, this integral only has a known solution for $r > R_i + R_j$ and $\lambda = \infty$. Physically, this is two finite size multipoles without any overlap between their charge distributions for unscreened electrostatic interactions. In this specific case, the integral can be written as [**65**]

$$\mathcal{I}_{L,l_i,l_j} = \frac{\pi^{3/2}}{2^3} \frac{R^{l_i+l_j} r^{-1-l_i-l_j} \Gamma\left(\frac{1+l_i+l_j+L}{2}\right)}{\Gamma\left(l_i+3/2\right)\Gamma\left(l_j+3/2\right)\Gamma\left(1+\frac{L-l_i-l_j}{2}\right)} \times F_4\left(\frac{l_i+l_j-L}{2}, \frac{1+l_i+l_j+L}{2}; l_i+\frac{3}{2}, l_j+\frac{3}{2}; \frac{R_i^2}{r^2}, \frac{R_j^2}{r^2}\right), \tag{2.26}$$

where F_4 is the Appell hypergeometric function of the fourth kind. Due to $\Gamma(1+(L-l_i-l_j)/2)$ in the denominator and the Clebsch-Gordan coefficient of 2.24, it is only evaluated when $L = l_i + l_j$.

To see this, consider that $\max_L = l_i + l_j$, for which the Clebsch-Gordan coefficient is non-zero and the integral coefficient is non-zero. For $L = l_i + l_j - (2n+1)$, $n \in \mathbb{N}$, the symmetries are incompatible and the Clebsch-Gordan coefficient is zero. For $L = l_i + l_j - (2n)$, $n \in \mathbb{N}$, the Gamma function evaluates to a negative integer, which is a pole of the function.

Since the first coefficient of the function is zero, it is trivial $F_4(0, \beta; \gamma, \gamma'; x, y) = 1$, yielding the usual powers of r for multipole expensions. For instance the $L = l_i = l_j = 0$ contribution, which is the monopole-monopole term, yields the usual

$$U_{ij}^{L=l_i=l_j=0} = \frac{Q_i Q_j}{r}, \tag{2.27}$$

where $Q_i = -4\pi R_i^2 \cos\theta_m$. Note that we defined the energy between charges to be $q_i q_j / r$ in $\chi_{es}(r)$, so this result is consistent with the unit system used $4\pi/\epsilon = 1$.

B. Field equations from stretched exponential functions

In equation 2.3, we have defined the auxiliary field as an convolution between the pairwise interaction $\chi(r)$ and the density field $\rho_j(\vec{r})$. In, equation 2.5, we relate the total energy to the convolution of the auxiliary field with the density field $\rho_i(\vec{r})$, which is written as

$$U_{ij}(\vec{r}_{ij}, \hat{R}_i, \hat{R}_j) = \rho_i(\vec{r}, \hat{R}_i) * \chi(r) * \underline{\rho_j}(\vec{r}, \hat{R}_j). \tag{2.28}$$

This triple convolution is then related to products in reciprocal space,

$$\tilde{U}_{ij}(\vec{\rho}, \hat{R}_i, \hat{R}_j) = \tilde{\rho}_i(\vec{\rho}, \hat{R}_i)\tilde{\chi}(\rho)\underline{\tilde{\rho}_j}(\vec{\rho}, \hat{R}_j) = \left(\tilde{\rho}_i(\vec{\rho}, \hat{R}_i)\tilde{\chi}(\rho)^{1/2}\right)\left(\tilde{\chi}(\rho)^{1/2}\underline{\tilde{\rho}_j}(\vec{\rho}, \hat{R}_j)\right). \tag{2.29}$$

If there exists a well-defined inverse transform of $\tilde{\chi}^{1/2}(\rho)$ and assuming that $\rho_i(\vec{r}) = \rho_j(\vec{r})$, then we can define an new auxiliary field such that $\tilde{\Phi}_{\rho_i\chi}(\vec{\rho}, \hat{R}_i) = \tilde{\rho}_i(\vec{\rho}, \hat{R}_i)\tilde{\chi}(\rho)^{1/2}$. The energy is then defined as a self-convolution

$$U_{ij} = \Phi_{\rho_i \chi}(\vec{r}_i, \hat{R}_i) * \underline{\Phi_{\rho_i \chi}}(\vec{r}_j, \hat{R}_j) \tag{2.30}$$

The well-defineness of inverting $\tilde{\chi}(\rho)^{1/2}$ is quite limiting as we have only found that stretched exponentials $\chi(r) = \exp(-r^q)$ with $1/2 \leq q \leq 2$ fit this criteria.

C. Vector fields

In Section 2.3 we describe directional interactions under the assumption that energy can be expressed as an overlap of scalar fields. However, the approach is generalizable to tensor fields. For simplicity, let us look at an interaction that stems from the inner product of the vector field of two distinct particles Φ_i and Φ_j,

$$U_{ij} = \int_V \vec{\Phi}_i \cdot \vec{\Phi}_j dV. \tag{2.31}$$

This type of interaction can be used to describe electrostatic interactions through electric fields,

$$U_{ij}^E = \frac{1}{2} \int_V \epsilon |E|^2 dV = \frac{1}{2} \int_V \epsilon \left(|E_i|^2 + |E_j|^2 + 2\vec{E}_i \cdot \vec{E}_j \right) dV, \tag{2.32}$$

where the first two terms are constants and the last term is in the same form as equation 2.31. In order to evaluate 2.31, we separate the field into multiple components such that

$$\vec{\Phi}_i = \Phi^x \hat{x} + \Phi^y \hat{y} + \Phi^z \hat{z}. \tag{2.33}$$

in the reference frame of the particle. The additional difficulty stems from the fact that once the particle is rotated, Φ^z may now point in the $\hat{x}$ direction. This is resolved by considering the overlap of 9 fields, by taking rotation of unit vectors

$$U_{ij} = \sum_{k,k'} \int_V \Phi_i^k \Phi_j^{k'} \hat{R}_i \hat{k} \cdot \hat{R}_j \hat{k'} dV, \tag{2.34}$$

where $k, k' = x, y, z$ and $\hat{R}_i$ is the rotation operator of the i^{th} particle. Unlike the expansion done for interacting charges in equation 2.22, direct use of an electric field permits the use of charge distributions interacting in non isotropic media, that is, ϵ only has the restriction that it needs to be constant throughout the volume. This could be used for instance, to calculate charge interactions of colloids suspended in liquid crystal media, where ϵ is a tensor.

D. Excluded volumes and Van der Waals gas

In coarse-grained models, one generally uses Lennard-Jones forces to model interactions. This includes a short-ranged repulsive part which shows a r^{-12} dependance. This would suggest use of $\chi(r) \sim (\sigma/r)^{12} - (\sigma/r)^6$. However, the Fourier transform of such a function does not exists. One could regularize it by changing r to $r + \delta$, or adding other short ranged potentials to remove the divergence, but this hides a major problem in that we truncate the Fourier series or equivalently use spatial filtering. While Eq. 2.3 is strictly physical and exact, after truncation it is akin to

$$U_{ij} = \int_V \langle \rho_i(\vec{r}) \rangle \langle \Phi_{\rho_j}(\vec{r}) \rangle, \tag{2.35}$$

where $\langle\rangle$ is some kind of spatial average consistant with the Fourier series truncation. If one plots the pair distribution function for a Lennard-Jones system, it becomes trivial to see that no overlap is present for small values of r (or large $\chi(r)$). In order to evaluate the excluded volumes, we will need to use some spatial average of the Lennard-Jones interactions. As an approximation, one can still use regularization, but it has to be done carefully as it may impact the system behavior.

Instead of using a soft repulsive term, one can start with the Van der Walls equation of state, which writes the average enthalpy per particle of a gas of hard spheres of volume b as

$$H_{VdW}/N = k_B T \left(\frac{1}{1-\rho b} + \frac{3}{2} \right). \tag{2.36}$$

Here we assume that we can treat all excluded volume interactions as Van der Waals gas and write the overall energy as the integral of the spatially filtered enthalpy. We also assume that local density can be written as pairwise densities, such that $\rho = \rho_i + \rho_j$ in the local enthalpy. Disregarding the constant $3/2$ term, this leads to a local enthalpy defined by

$$H_{VdW}^{local} = k_B T \frac{1}{1-(\rho_i+\rho_j)b}. \tag{2.37}$$

In the present formalism, we cannot treat arbitrary potential in ρ. However, we can expand in power series,

$$H_{VdW}^{local} \approx k_B T \left(1 + b(\rho_i+\rho_j) + b^2(\rho_i+\rho_j)^2 + b^3(\rho_i+\rho_j)^3 + ... \right). \tag{2.38}$$

Given that powers of strictly ρ_i and ρ_j are not part of pairwise potentials of colloid, we do not have to deal with them. We are then left with the following interaction

$$\beta H_{VdW} = 2b^2 \int_V \rho_i(\vec{r}-\vec{r}_i,\hat{R}_i)\rho_j(\vec{r}-\vec{r}_j,\hat{R}_j) + 3b^3 \int_V \rho_i^2(\vec{r}-\vec{r}_i,\hat{R}_i)\rho_j(\vec{r}-\vec{r}_j,\hat{R}_j) + \rho_i(\vec{r}-\vec{r}_i,\hat{R}_i)\rho_j^2(\vec{r}-\vec{r}_j,\hat{R}_j) + ... \tag{2.39}$$

One can then produce fields for $\rho(\vec{r},\hat{R})$, $\rho^2(\vec{r},\hat{R})$, ..., for all colloids and trucate the series at some power of ρ.

E. Supplementary data for the liquid-gel transition

The liquid-gel morphology transition of asymmetric charged Janus particles is in appearance a continuous transition where the branches of the gel are thick near the liquid phase. This can be seen on Fig. 2.6. The transition is characterized by gradual changes of the pair correlation function, as shown on Fig.2.7.

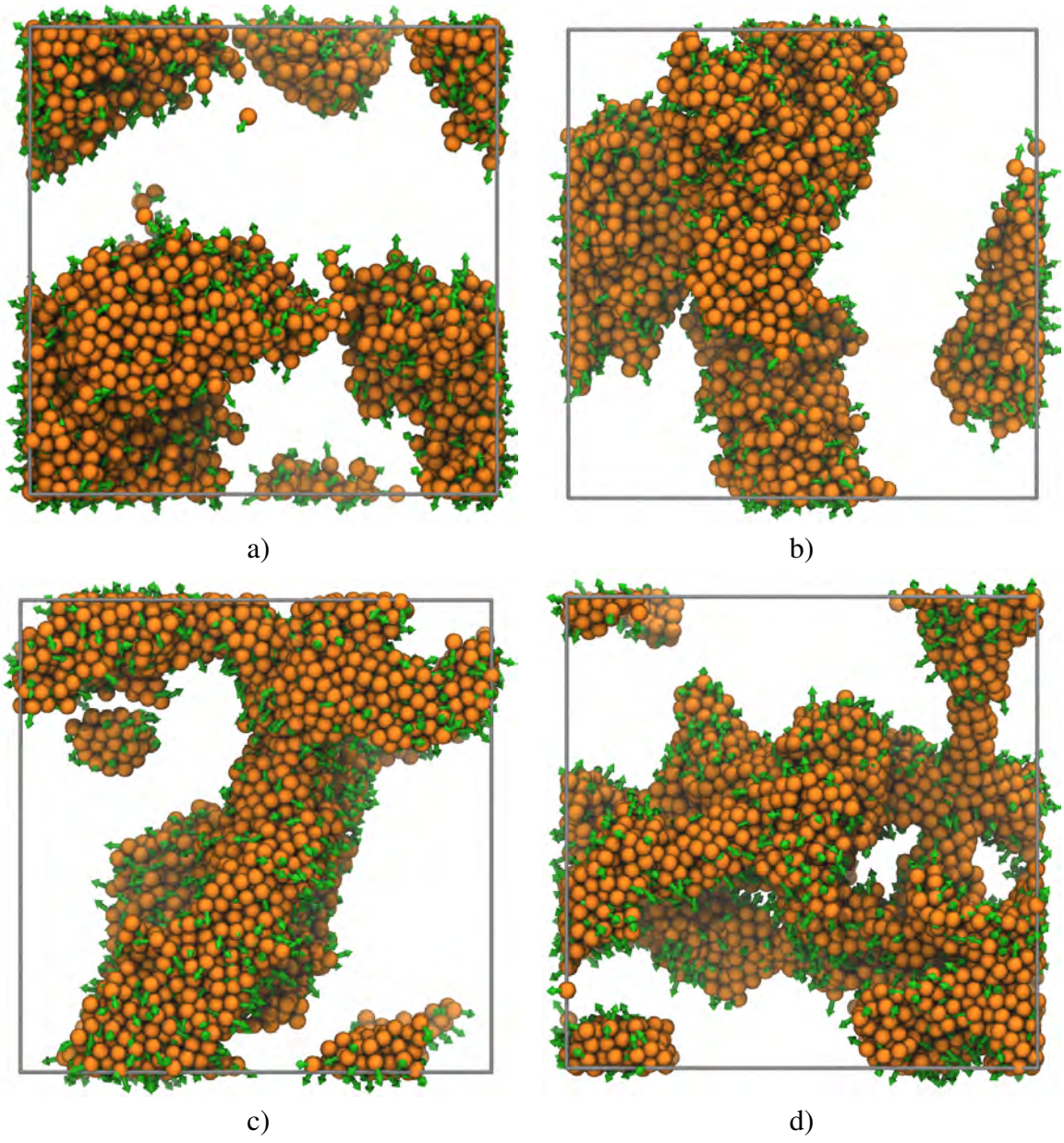

Figure 2.6. Snapshots of the simulations of charged Janus particles ($\theta_m = 1.40$) for different temperatures. a) $T = 1.62$, b) $T = 1.42$, c) $T = 1.20$, d) $T = 1.0$. Arrows indicate the north pole of the Janus particles

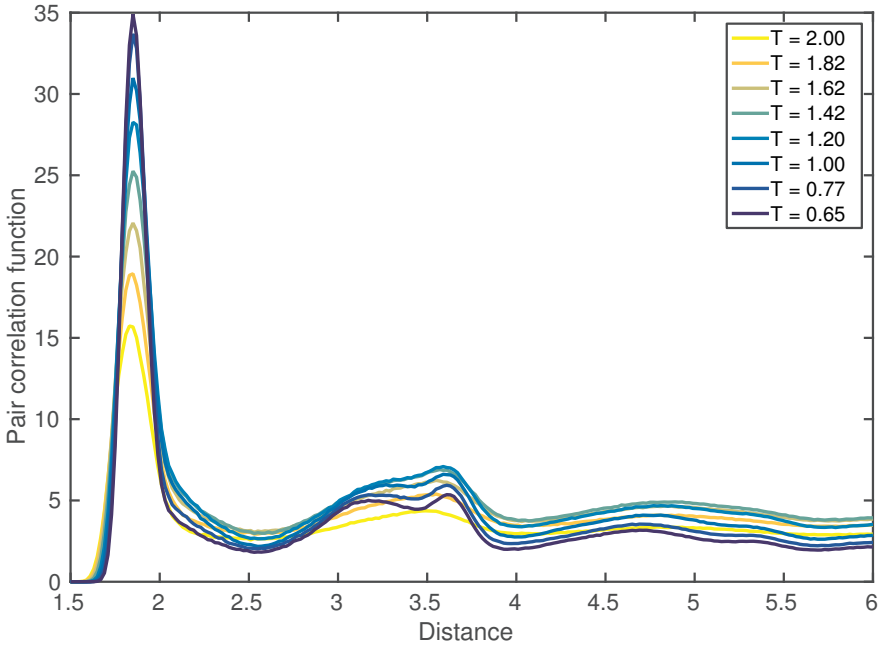

Figure 2.7. Pair correlation functions for different temperatures for the asymmetric ($\theta_m = 1.40$) Janus particles for $\lambda = 0.32$.

CHAPTER 3

Time dependent orbitals for coarse-grained polymer-coated colloids

Authors : Martin Girard, Trung Dac Nguyen, Monica Olvera de la Cruz

1. Abtract

Nanoparticles including proteins functionalized with thiols, polymers or DNA self assemble into one-, two-and three-dimensional structures or amorphous aggregates depending on the configurational changes of the grafted chains upon association. In these systems is often desire to reduce the degrees of freedom of the chains with a few collective variables that capture the effective interaction between the particles. We develop here an orbital model for coarse-graining anisotropic colloids including the deformation of the grafted chains. Pair interactions between the colloids induce the time-dependent deformation of the chain density fields, yielding implicit many-body effects. Using this model, we revisit some of the recently published work on deformation of the shell of grafted chains around nanoparticles. We show that for spherical particles, the energy of deformation increases with angular number, consistent with previously published results including the grafted chain explicitly. Unlike spherical models, however, this coarse-graining method is applicable to any anisotropic colloid.

Nanoparticles including proteins functionalized with thiols, polymers or DNA self assemble into one-, two-and three-dimensional structures or amorphous aggregates depending on the configurational changes of the grafted chains upon association. In these systems is often desire to reduce

the degrees of freedom of the chains with a few collective variables that capture the effective interaction between the particles. We develop here an orbital model for coarse-graining anisotropic colloids including the deformation of the grafted chains. Pair interactions between the colloids induce the time-dependent deformation of the chain density fields, yielding implicit many-body effects. Using this model, we revisit some of the recently published work on deformation of the shell of grafted chains around nanoparticles. We show that for spherical particles, the energy of deformation increases with angular number, consistent with previously published results including the grfted chain explicitly. Unlike spherical models, however, this coarse-graining method is applicable to any anisotropic colloid.

2. Introduction

Functionalizing nanoparticles and colloids with short ligands, polymers and complementary DNAs has been recognized as a promising approach to engineering nanostructures with desirable complexity such as higher-order assemblies and colloidal crystals [**66, 67**]. With the characteristic dimension of the assembling building blocks varies from 5-100 nm, the primary driving forces for the formation of the assembled nanostructures come from non-covalent interactions such as electrostatics, hydrophobicity and van der Waals attractions [**68, 69**]. The fact that these interactions are little sensitive to the atomic and molecular details of the building blocks inspires the development of generic computational models as long as they capture the most relevant physics of the phenomena of interest. Clearly, the geometry and physical properties of the polymer shell are the vital factors that determine the interactions between the polymer functionalized nanoparticles and colloids.

Coarse-grained models for colloids and nanoparticles coated with a soft corona of polymers or DNA strands have been developed and used extensively in the literature. To improve the computational efficiency of studies that involve a large number of particles, it is highly desirable to represent the degrees of freedom of the polymer chains with a few collective variables that implicitly capture the effective interaction between the particles. For colloids with arbitrary shapes, the collective variables need to handle relative orientations of the bodies using techniques such as the recently developed orbital expansion method [**70**]. While such approach in many cases provide sufficient fidelity, it is limited because it neglects any internal degree of freedom that the grafted chains may possess. For chain-coated colloids, the hidden variable is the deformation of the grafted shell of chains around the particle, which gives rise to multibody effects. We have recently observed these effects in DNA-coated cubes [**33**], where deformation of the DNA shell induces symmetry breaking from cubic to tetragonal symmetry. Multibody interactions in spheres coated with chains were also observed in Refs. [**71**] and [**72**] but discarded as being weak. Strong effect of shell deformation was observed in binary hydrocarbon-grafted gold particle assemblies [**21**]. In particular, the system shows strong deviation from the hard sphere packing considerations (see [**73**] for a discussion of packing of soft spheres), which can be explained by deformation of the shell of grafted chains [**20**]. It was demonstrated that the shell of a colloid only deforms if it has fewer than six nearest neighbors. Usage of three-body correction as done in [**74**] was nonetheless insufficient to reproduce the crystal lattices observed in [**21**]. Moreover, extension of three-body potentials or the approach of [**20**] to anisotropic bodies is obviously not straightforward.

Herein, we address the limitation of existing coarse-grained models by incorporating collective degrees of freedom representing the shell of grafted chains in terms of orbitals, in a similar fashion of our previous description of anisotropic bodies [**70**]. The approach is conceptually similar to the development of [**75**] but goes beyond the calculation of phonons. It is also close in spirit to

other normal mode techniques developed in [**76**], but makes use of localized basis sets. While the approach is mathematically exact only for small deformations, it captures general behaviors of these deformable systems and is applicable to arbitrary anisotropic bodies. We revisit the binary superlattice systems comprised of chains grafted colloids, validate the regimes in which the six neighbor rule is valid and provide means to evaluate whether deformation should be considered.

3. Mathematical formalism

The mathematical basis on which we rely has been described in our previous paper [**70**]. We relate the potential energy between two colloids i and j, located at coordinates $\vec{r}_i$ and $\vec{r}_j$, with orientation $\hat{R}_i$ and $\hat{R}_j$ with particle density ρ_i and ρ_j and interaction $\chi(r)$ through :

$$U_{ij}(\vec{r}_i, \hat{R}_i, \vec{r}_j, \hat{R}_j) = \int_V \rho_i(\vec{r} - \vec{r}_i, \hat{R}_i)\Phi_{\rho_j}(\vec{r} - \vec{r}_j, \hat{R}_j)d\vec{r} \tag{3.1}$$

Where Φ_{ρ_j} is an auxiliary field given by:

$$\Phi_{\rho_j}(\vec{r}_j, \hat{R}_j) = \rho_j(\vec{r}_j, \hat{R}_j) * \chi(r) \tag{3.2}$$

In our previous paper, we had described the field using Fourier transforms, which describe a transform into an continuous basis. This is unsuitable for time variant fields as we would have to update all the reciprocal space values of all colloids at every time step. Here we want to use a finite basis such that the density around a colloid can be written as :

$$\rho_i(\vec{r}) = \sum_{nlm} c_{nlm} Y_\ell^m(\theta, \phi) F_n^\ell(r) = c_{nlm} \left| nlm \right\rangle$$

Where we have introduced Ket notation for convenience and to highlight the similarities with quantum mechanical expressions. In order to obtain convergence and tractable calculation, we require that the basis form a complete and orthogonal set such that $\langle nlm \mid n'l'm' \rangle = \delta_n^{n'} \delta_l^{l'} \delta_m^{m'}$ and any spatial function can be exactly represented by equation 3. The vector of all coefficients c_{nlm} is written as $\vec{c}$. In order to treat rotations, we introduce Wigner functions $\mathcal{D}^l_{m,\mu}$. A rotation operator $\hat{R}$ takes a state $|nlm\rangle$ and transforms it such that :

$$\hat{R} \, |n\ell m\rangle = \sum_{\mu} \mathcal{D}^{\ell}_{m,\mu}(\hat{R}) \, |nl\mu\rangle$$

For simplicity of the notation, we write a set of indices n, l, m as k, so that $|n\ell m\rangle = |k\rangle$. We expend the density such that $\rho_i(t) = \rho_i^0 + \Delta\rho_i(t)$, which then yields a time dependent density for any colloid i:

$$\rho_i(\vec{r}, \hat{R}_i) = \sum_{n,\ell,m,\mu} \left(c_k^0 + c_k(t)\right) \mathcal{D}^{\ell}_{m,\mu} \left(\hat{R}_i\right) Y_{\ell}^{m}(\theta, \phi) F_n^{\ell}(r) \tag{3.3}$$

For isolated colloids the interactions between the internal degrees of freedom yields the self energy U_{ii}, given by:

$$U_{ii} = \left(\rho_i^0 + \Delta\rho_i(t)\right) * \chi(r) * \left(\rho_i^0 + \Delta\rho_i(t)\right) \tag{3.4}$$

Which can be expended into :

$$U_{ii} = \rho_i^0 * \chi * \rho_i^0 + 2\rho_i^0 * \chi * \Delta\rho_i(t) + \Delta\rho_i(t) * \chi * \Delta\rho_i(t) \tag{3.5}$$

Up to now, the development is entierly general, and we are free to choose any function for ρ_i^0 in equation 3.4. If we choose ρ_i^0 to be the time averaged value for an isolated colloid then the time varying density $\Delta\rho_i(t)$ can be viewed as fluctuations around the mean. If these fluctuations are sufficiently small, we have at first order $\int_V \Phi_{\rho_i^0}\Delta\rho_i(t) = 0$. Since $\rho_0 * \chi * \rho_0$ is time independant, it does not contribute to forces. The only term which is not static in time is given by :

$$U_{ii} = \int_V \Delta\rho_i \chi \Delta\rho_i = \vec{c}^T \bar{M} \vec{c} \tag{3.6}$$

Where the interaction matrix $\bar{M}$ is given in a shape analogous to quantum mechanics :

$$\bar{M}_{k,k'} = \int_V \Delta\rho_k \chi \Delta\rho_{k'} = \langle k \,|\chi|\, k' \rangle \tag{3.7}$$

The eigenvectors of $\bar{M}_{k,k'}$ are normal modes of the colloid as one would expect from linear theory. They can be represented by a set of independent oscillators: $U_{ii} = \sum_K 1/2 u_K c_K^2$. The time evolution of c_K is then given by a Langevin equation:

$$\ddot{c}_K = -\frac{dU}{dc_K} m_K - \gamma_K \dot{c}_K + \eta_K \tag{3.8}$$

where m_K has units of mass and represents a collective mass of the Kth eigenmode, γ_K is the associated friction and η_K a random force consistent with fluctuation-dissipation theorem. This sets the method apart from usual Car-Parrinello approaches, as here the temperature is not zero. While one might ponder on the significance of collective masses of the internal degrees of freedom, calculation of any realistic system where monomers experience friction will lead to an overdamped

equation of motion for relevant degrees of freedom. Therefore, choice of the collective mass is of no importance for calculations. Nevertheless, as we show later, one can extract a value for this parameter when coarse-graining the system.

4. Numerical Implementation

4.1. From explicit chain models to orbitals

In order to compute time evolving orbitals, the series coefficients c_k^0 and $c_k(t)$ must be obtained from single colloid MD simulations. For this purpose, we run simulations consisting of a single colloid pinned to the center of the simulation box. Since MD simulations only record coordinates of the center of beads, we need to replace every individual "atom" with a gaussian function. The with of this function is chosen to match bead diameter. For every frame, we then need to integrate the basis $\langle k|$ against the density $|\rho(t)\rangle$. Since this is a very expensive operation we use a few approximations. First, we define a grid in space on which we can define $|k\rangle$ at every point. For every frame, we then pin every MD bead to the closest point on that grid. The whole grid is then convolved with a gaussian kernel, which is identical to replacing every bead by a gaussian function centered around the center of mass of each bead. We then take the conjugate of $|k\rangle$ and multiply it pointwise against the density grid and sum the result. This produces the approximation of :

$$c_k(t) = \sum_i \langle k \mid \frac{1}{\sigma_i\sqrt{2\pi}} \exp(-|\vec{r} - \vec{r}_i|^2/2\sigma_i^2)\rangle$$

Where σ_i is the diameter of the ith bead and $\vec{r}_i$ it's position. For this calculation, we ignore any contribution coming from inside the colloid rigid core. We then obtain the average density vector components by a simple average: $c_k^0 = \langle c_k(t)\rangle_t$. The matrix $M_{k,k'}$ is then computed directly from fluctuations: $M_{k,k'} = \langle k - c_k^0 \mid k' - c_{k'}^0\rangle$. The matrix is then diagonalized, which

provides the eigenmode. The spring constant of each mode can be found either by the eigenvalue or mean occupancy $\langle c_K^* c_K \rangle$ which are equivalent. An estimate for the collective friction γ_K can be found by the frequency response of the oscillators to a damped oscillator with profile $a_K(\omega) \propto \omega_0^2/(\omega\sqrt{(2\omega_0\gamma_K)^2 + \omega^{-2}(\omega_0^2 - \omega^2)^2})$, where ω_0 is the intrinsic frequency of the Kth collective oscillator.

4.2. Choosing an appropriate $F_n^l(r)$ function set

As discussed in the previous section, the choice of $F_n^\ell(r)$ is arbitrary, with the requirement that it forms a complete orthogonal basis. If one uses an infinite number of basis function, results are independent on the exact form. However, we wish to truncate the series to only keep the lowest order modes, which implies that some functions are better than others.

Truncation of the series at $n = 1$ (a single spherical term in the series) yields a few interesting results. If fluctuations are completely discarded we have $\Delta\rho_i(t) = 0$. The density is thus spherically symmetric and time-independent. Error on the density can be minimized by choosing a set such that $F_1^0(r) = \rho_i^0(r)$. Furthermore, interactions between two colloids depends only on the distance between them and is completely determined by $\chi(r)$, which assumes the role of the potential of mean force. Standard approaches to determination of effective interactions can thus be viewed as a severe truncation of equation 3 to a single non-fluctuating internal degree of freedom.

To obtain sets of suitable functions for $F_n^\ell(r)$, one can take solutions to Stürm-Liouville problems which yield spherical harmonics for the angular part. In particular, the separable Laplace equation in spherical coordinates is well studied and occurs frequently in quantum mechanics :

$$-\frac{\partial^2}{\partial r^2}F(r) + \left(V(r) + \frac{\ell(\ell+1)}{r^2}\right)F(r) = -\lambda F(r) \tag{3.9}$$

Where $V(r)$ is an arbitrary smooth potential function. The typical boundary conditions associated with this problem in quantum mechanics is $F(\infty) = 0$. Some solutions are known for specific forms of $V(r)$. For instance, $V(r) = -Z/r$ yields solutions in the form of hydrogenoid wavefunctions. For coarse-graining purposes, one may wish to use $V(r > r_m) = \infty$. For the sake of simplicity, we restrict the study to hydrogenoid wavefunctions.

While the general form of $V(r)$ is fixed, we have to choose a "good" value of Z, which requires minimization of some error. This procedure must also be done for general optimization (not restricted to Z) of the basis set. For this purpose, we define the error on the density field as:

$$\text{Err} = \frac{||\rho(\vec{r}, \hat{R}) - \bar{\rho}(\vec{r}, \hat{R})||_2^{1/2}}{||\bar{\rho}(\vec{r}, \hat{R})||_1} \tag{3.10}$$

, where $\bar{\rho}(\vec{r}, \hat{R})$ is the true density measured from MD simulations and $||\cdot||_N$ is the L_N-norm.

One can see the close connections between equation 3.1 and the usual *ab initio* molecular dynamics (AIMD) potentials, with a few differences. Here, we expend the density $\rho(\vec{r})$ instead of the complex amplitude into fields. Obviously, the particles are classical so that we do not have to enforce fermion behavior such as parity of wavefunctions.

4.3. Implementation into an existing Molecular Dynamics simulation code

We implement our approach into LAMMPS [**49**], a massively parallel Molecular Dynamics code. The BODY package in LAMMPS provides a flexible framework for particles with user-defined internal degrees of freedom. The implementation involves three components: 1) a new data structure that stores the time-dependent eigenmodes as the internal degrees of individual particles; 2) a new force field that describes the interaction between the colloids, and 3) an integrator to evolve the eigenmodes over time. At a given time step, the force and torque between two colloids are

computed from their orbitals (Equation 3.7). The eigenmodes are evolved along with the colloids (3.8) in the velocity Verlet scheme. Our code is available for download at [url].

5. Polymer-coated spheres as a model

Spherical particles are ideal to study how this model performs. First, unlike our previous reserach on DNA-coated cubes in [**33**], we do not have to worry about a cube-like to sphere-like mean grafting density. The spherical symmetry results in modes with well defined orbitals that can be labeled by their atomic counterparts, S($\ell = 0$), P($\ell = 1$), D($\ell = 2$), ...

The system we are interested in are spheres of diameter $d = 6\sigma$, grafted with n_{gr} chains each comprised of L beads of diameter $\sigma = 1$. These beads are connected by a harmonic springs with potential energy $U_s = k_s(r - r_0^s)^2/2$, with $r_0^s = \sigma$ and $k_s = 5k_BT/\sigma^2$, where k_BT is the thermal energy. Non-connected beads interact through a WCA potential (12-6 Lennard-Jones with cutoff set to $2^{1/6}\sigma$), corresponding to polymer chains in a good solvent.

Error analysis based on optimized hydrogenoid wavefunction yield small typical RMS errors (see Fig. 3.1). The error decreases with either increased grafting density or polymer length.

5.1. Spectral analysis

A notable prediction in ref [**20**] is the limit on topological charge $q_T \leq 4$ or equivalently a restriction in angular number $\ell \leq 3$. This limited should be captured in the spectrum. In order to decompose the fluctuations into series of modes, we use a cutoff of $n = 5$ (55 modes), which should allow for modes with $\ell = 4$.

Three sets of data are considered, varying n_{gr} from 5 to 55 with $L = 15$ and varying L from 1 to 25 with either $n_{gr} = 5$ or $n_{gr} = 20$. The results, shown in Fig. 3.2, reveals interesting properties of the energy spectrum. Under reasonable grafting ($n_{gr} \lesssim 36$), hairy particles $L > d$, fluctuations are

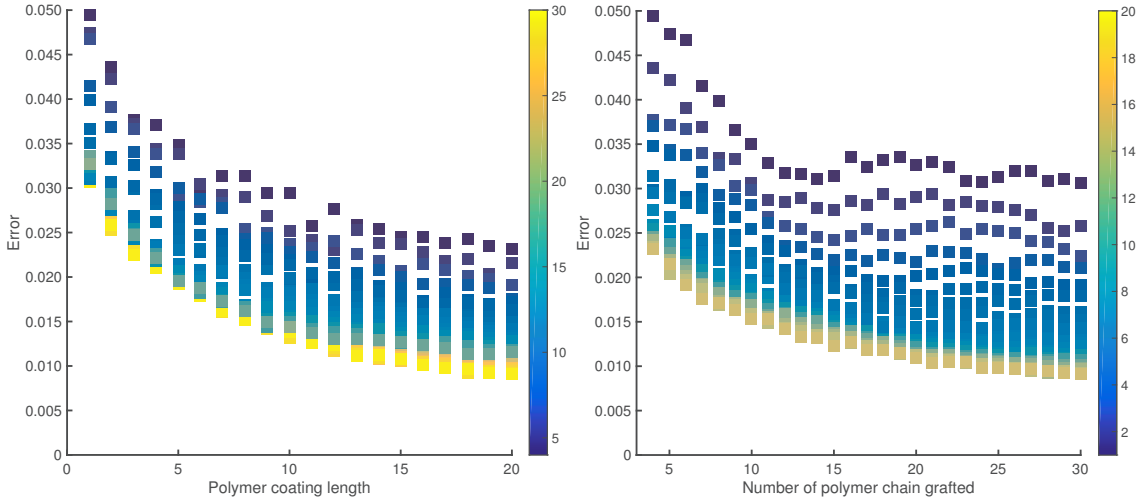

Figure 3.1. Error as defined by equation 3.10 as a function of polymer length (left) and coating density (right). Color indicate coating density and length respectively

proportional to n_{gr} so that the energy spectrum is nearly flat. Deviations seen for $n_{gr} > 36$ are due to the nematic ordering of the polymer strands near the particle core. Since the interaction with an external field is proportional to the number of grafted polymer strands, it follows that deformation amplitude relative to the overall number of strands is independent of the grafting density.

If the polymer length is increased, the energy of deformation goes down as expected (see Fig. 3.3). This decrease takes form of a power law $u_K \sim L^{-p(K)}$, where $p(K)$ is an exponent dependent on the mode number K. Generally, the cost of a higher order mode falls quicker with increasing polymer length than a low order. This strongly suggest that the topological charge limit observed in [**20**] is only valid for colloids with relatively low chain length.

6. Future work

There is remaining work on this subject. In particular, we want to use this method to simulate assembly of binary crystals made of particles A and B, with hydrodynamic radius ratio $r_A/r_B \approx 0.43$. Based on previous work, these assemble into CaB_6-type crystal in absense of deformation

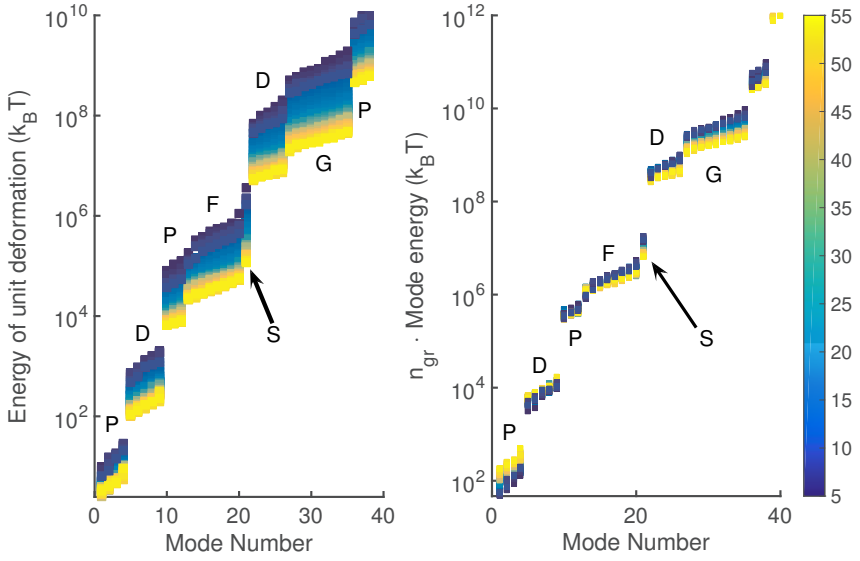

Figure 3.2. Energy spectrum of fluctuations around a sphere grafted with varying number of polymers chains of length $L = 15$. The deformation modes are labeled by their symmetry (S, P, D, F, G corresponds to values of $\ell = 0, 1, 2, 3, 4$). For a deformation of amplitude one, the energy is a strong function of the number of polymer chains (left), but this profile can be flattened by normalizing with the number of chains

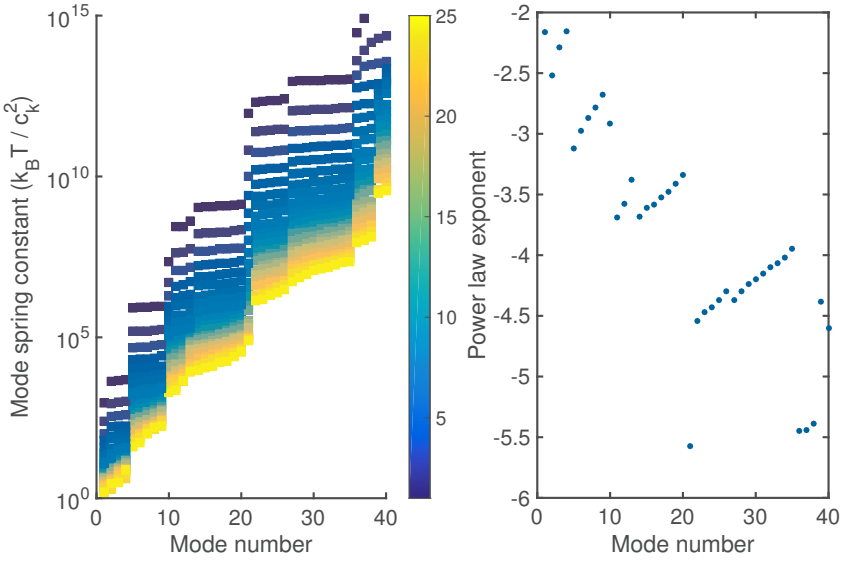

Figure 3.3. Energy spectrum of the normal modes as the length of the grafted polymer is increased from $L = 1$ to $L = 25$ (left). The spring constant falls as a power law with polymer length that depends strongly on the mode order (right)

and bccAB$_6$ in presence of deformation. This would produce an elegent confirmation that the method is able to match previous predictions.

We also intend to study spectral features of anisotropic particles such as cubes. Unlike spheres, their modes are not symmetrically pure. This means that the lowest eigenmode is not of type S but rather a sum of S, G, I, ... symmetries. This complicates analysis, but we intend to relate the energy of deformation to our previous results on DNA-coated cubes.

Part 2

Physics of real self-assembled systems

While the mean-field model developed captures information about colloid shape and deformation of polymer brushes, it is not entirely suitable for high-information polymers. The problem lies in the depletion of available binding sites: each base can only form a single bond. The mean-field approach assumes linearity with the density, so that if we have two types of DNA binding together, doubling the amount of each type quadruples the overall binding energy instead of doubling it. The progress made towards representing deformable polymer coated particles in the previous sections is thus not sufficient to fully model experimental systems. It also does not allow for inclusion of details such as ion-strand interactions.

For the experimental systems we are interested in, we used detailed models with explicit chains. In the following chapters, multiple different systems will be presented, each of which is described in a single paper either published or in preparation.

The first work concerns crystals assembled from anisotropic building blocks. The shapes studied have high symmetry: rhombic dodecahedrons, octahedrons and cubes. For very short strands, the crystal lattice is given by the close packing of the shapes: FCC, BCC and SC. For extremely long strands, the lattice is given by packing of spheres, FCC, and the particles are randomly oriented. Interestingly, we find symmetry breaking for cubic particles at intermediate DNA lengths.

The second work models growth of AB_2-type lattices (P6/mmm with filled 2d sites). Since the base unit cell contains three unique points, each set of Miller indices can represent up to three different planes. This has a unique effect on crystal growth as the final crystal habit can expose high energy planes instead of the low energy planes predicted by the Wulff construction. This is due to high energy barriers between different planes with the same Miller indices.

The third article looks at crystal growth at different salt concentrations in water. Addition of salt ions in the solution induces increased barriers to attachment of colloids to the crystal and slows down crystal growth. From the viewpoint of the crystal, the long ranged mass diffusion is faster

and each grain undergoes the interface-limited to diffusion-limited regime change at larger grain size, thus producing larger crystals.

The last article models a system assembled from a binary mixture of large ($\sim$10 nm) and small particles ($\sim$2 nm). The latter particles have a small amount of DNA strands grafted onto them. Large colloids have a number of bound strands approximately equal to the average binding fraction due to the law of large numbers. For smaller particles however, individual colloids have only a few strands and can even have all their strands unbound. This leaves them free to roam the crystal, behaving as electrons rather than atoms.

CHAPTER 4

Exploring the zone of anisotropy and broken symmetries in DNA-mediated nanoparticle crystallization

Authors: Matthew N. O'Brien*, Martin Girard*, Hai-Xin Lin, Jaime A. Millan, Monica Olvera de la Cruz, Chad A. Mirkin

1. Abstract

In this work, we present a joint experimental and molecular dynamics simulations effort to understand and map the crystallization behavior of polyhedral nanoparticles assembled via the interaction of DNA surface ligands. In these systems, we systematically investigated the interplay between the effects of particle core (via the particle symmetry and particle size) and ligands (via the ligand length) on crystallization behavior. This investigation revealed rich phase diagrams, previously unobserved phase transitions in polyhedral crystallization behavior, and an unexpected symmetry breaking in the ligand distribution on a particle surface. To understand these results, we introduce the concept of a zone of anisotropy, or the portion of the phase space where the anisotropy of the particle is preserved in the crystallization behavior. Through comparison of the zone of anisotropy for each particle we develop a foundational roadmap to guide future investigations.

2. Body

Over the past decade, major advances in the control of nanoparticle interactions have led to powerful methods to assemble colloidal crystals [**66, 77, 78, 79, 80, 81, 82, 83, 84**]. A high

degree of structural control can be achieved in these methods if surface-bound ligands are used as nanoscale bonding elements to control the specificity, spacing, and strength of interactions. DNA has emerged as a particularly versatile ligand whose chemically and structurally defined nature can be used to program the symmetry, lattice parameters, and habit of colloidal crystals [**66, 77, 82, 85, 86, 87, 8, 5, 88, 89, 90, 91, 92**]. The shape of the underlying nanoparticle influences the directionality of DNA interactions, which can result in correlated nanoparticle orientations and predictable crystal symmetries based on geometric considerations [**82, 8, 89, 92, 41**]. However, predictive control can be lost if the DNA shell does not preserve the anisotropy of the particle core [**8**], and thus key questions pertain to (i) the phase space over which predictable directional interactions persist and (ii) the nature of the phase transitions that occur as the anisotropy of the particle disappears. Identifying this "zone of anisotropy" and the broken symmetries that form are critical to establish design rules for work with nonspherical particles and to develop nanostructured materials with controlled properties.

Herein, we systematically investigate the phase space encoded by particle symmetry, particle size (L), and DNA length (D) to understand and map where directional interactions persist (Fig. 4.1). We show that particle symmetry dictates the crystalline states that can be accessed and how easily changes in L and D affect phase transitions between these states, which include transitions in Bravais lattice (i.e., the symmetry of how the particles are arranged within the unit cell) and particle orientation. The concepts introduced herein provide a roadmap to understand and predict particle crystallization behavior toward the construction of functional nanoparticle-based materials.

To map the zone of anisotropy in DNA-mediated nanoparticle crystallization, three common polyhedra were investigated: cubes, octahedra, and rhombic dodecahedra. These nanoparticles are primarily bound by a single crystallographic plane repeated across the structure 6, 8, or 12 times, respectively (Fig. 4.1A), and can be synthesized via a seed-mediated method that yields >95%

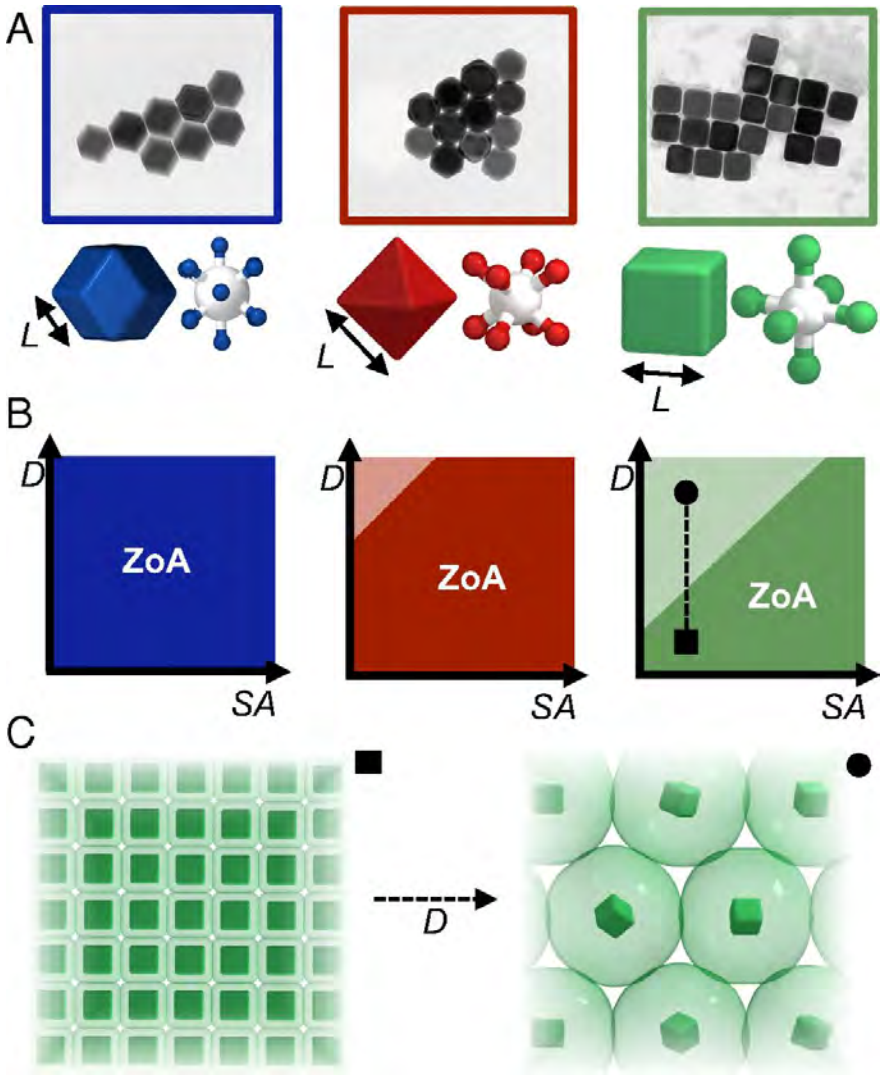

Figure 4.1. Polyhedral nanoparticles with different symmetries can be functionalized with DNA and used as building blocks to study nanoscale crystallization processes. (A) EM images of cube (green), octahedron (red), and rhombic dodecahedron (blue) nanoparticles used in this work shown in order of increasing particle symmetry. Below each image is a model of the particle shape and a corresponding ball-and-stick diagram to indicate the symmetry. Nanoparticle edge length (L) is indicated next to each shape. (B) The phase space encoded by DNA length (D) and nanoparticle surface area (SA) is depicted for each symmetry nanoparticle. The darker color region in each phase diagram indicates the zone of anisotropy (ZoA). (C) The phase transition depicted by the dashed line in B, wherein L is fixed as D is increased, is shown, wherein the anisotropy of the particle core is lost.

of the desired shape with <5% variation in size (Fig. 4.1A) [**6**]. Particle uniformity was rigorously analyzed with a recently reported and freely available program that algorithmically analyzes transmission electron microscopy (TEM) images to analytically determine nanoparticle structure [**7**]. As-synthesized gold nanoparticles were densely functionalized with DNA, and subsequently DNA "linkers" of programmable length (tuned in rigid 12-nm, double-stranded segments) were hybridized to the surface-bound DNA. Each DNA linker possesses a short, single-stranded "sticky end" with a self-complementary sequence that extends into solution (Table S1). Together, this design yields polyvalent building blocks that connect to each other through the collective hybridization of many DNA sticky ends. To facilitate comparison between different shapes, surface area (SA) was used instead of L, because this number correlates with the number of DNA strands given a similar DNA density.

Crystals were formed by slowly annealing DNA-functionalized nanoparticles from high to low temperature, which results in a slow increase in supersaturation that ensures nanoparticles crystallize into their lowest free energy configuration [**3**]. These crystals were analyzed in solution with small angle X-ray scattering (SAXS; Fig. S1 and Tables S2-S4) and in the solid state, after encapsulation in silica, with EM (Fig. S2). Scattering data were modeled using the pseudolattice factor approach (SI Materials and Methods) [**89, 93, 94**] and compared with experimental data to determine crystal symmetry, lattice parameters, and particle orientation. Importantly, use of a slow crystallization procedure and highly uniform building blocks minimizes the formation of defects and kinetically trapped states, which enables increased crystalline domain sizes, crystalline formation over a wider range of conditions, and more definitive assignments of thermodynamic phase boundaries relative to previous reports [**8**].

To elucidate the zone of anisotropy for each particle shape, five SA and five D were investigated, beginning with high-symmetry rhombic dodecahedra (Fig. 4.2 A and B, Fig. S1, and Table

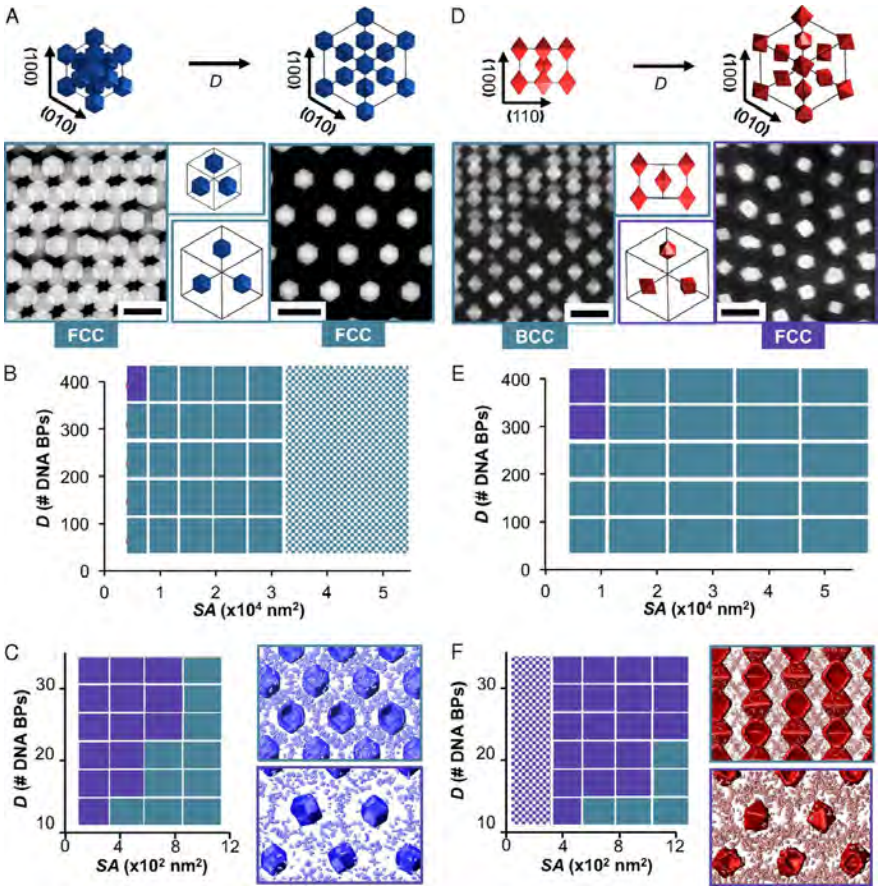

Figure 4.2. The crystallization behavior of high symmetry polyhedra exhibits limited complexity as a function of D and L. (A) An FCC crystalline phase is observed for the majority of the phase space investigated for rhombic dodecahedra. To-scale unit cells are shown at top, with lattice vectors, for small and large values of D. EM images corresponding to the unit cells are provided below, with an inset from the unit cell to show particles in the same lattice plane. Throughout this figure, turquoise represents the zone of anisotropy (i.e., a crystalline phase), and purple represents a plastic crystal phase. (Scale bars, 200 nm.) (B) The experimental phase diagram for rhombic dodecahedra is shown as a function of D and SA. The checkered region indicates an extrapolation for larger, more experimentally challenging sizes of rhombic dodecahedra. (C) MD simulations confirm the same phase transition observed for rhombic dodecahedra as experiments, for systems that have been scaled to smaller, computationally more accessible sizes in a manner consistent with experiments. The spatial distribution of DNA sticky ends is shown at right for each phase, where the DNA is localized between particles for the crystalline phase and more isotropically distributed for the plastic phase. (D) As D increases for the smallest L of octahedra investigated, a phase transition from a BCC crystalline phase to an FCC plastic crystal is observed. (E) Experimental phase diagram over the same range of D and L shows that the zone of anisotropy occupies a smaller area of the phase space relative to the rhombic dodecahedra. (F) MD simulations (for particles with similar SA as the rhombic dodecahedra) confirm the observed phase behavior.

S2). Rhombic dodecahedra can pack with 100% efficiency when the 12 rhombus-shaped facets on a given nanoparticle align face-to-face with their neighbors in a crystalline phase (i.e., both translational and orientational order) with face-centered cubic (FCC) symmetry [**41, 38**]. Soft interactions similarly predict an FCC crystalline phase, due to the greater number of DNA hybridization events that arise from face-to-face interactions [**8**]. As SA decreases in these experiments (for a fixed D), one might expect that fewer DNA strands per facet would lead to a smaller enthalpic driving force for the crystalline phase and thus a transition to a plastic crystal phase (i.e., translational order, but orientational disorder) with FCC symmetry, as expected for spheres. Similarly, as D increases (for a fixed SA), one might expect that the greater free volume available to each sticky end would lead to an entropic driving force that decreases the directionality of interparticle interactions and results in a plastic crystal transition. Contrary to these expectations, FCC crystalline phases (Fig. 4.2 A and B) were observed for all but the sample with the smallest SA and largest D, and thus the zone of anisotropy encompasses nearly the totality of the investigated phase space. A linear increase in the lattice parameter (a) with D supports the crystalline phase assignment, and the slope of ~ 0.28 nm per base pair agrees with previous work for face-to-face interactions (Table S2) [**8, 89**].

To further understand how nanoparticle symmetry affects the zone of anisotropy, the crystallization of octahedra was similarly investigated (Fig. 4.2 D and E, Fig. S1, and Table S3). The dense packing of hard octahedra varies based on corner truncation or rounding [**95, 96, 97**], where body-centered cubic (BCC) or body-centered tetragonal (BCT) crystalline phases are favored for truncated octahedra [**38, 97**], and BCC or FCC plastic crystals are favored for rounded octahedra [**96, 98**]. In experimental systems, the hydrodynamic particle shape deviates from an ideal octahedron in favor of a BCC crystalline phase [**8**]. Similar to the rhombic dodecahedra described above, the zone of anisotropy for octahedra (i.e., a crystalline phase with BCC symmetry) fills the majority of the investigated phase space (Fig. 4.2E). Unlike the rhombic dodecahedra, however,

a phase transition and lattice compression occurred for larger SA octahedra at shorter D - from a BCC crystalline phase to a FCC plastic crystal, as D increased (Fig. 4.2D).

To understand the origin of these phase transitions, nanoparticles were modeled with molecular dynamics (MD) simulations. These simulations build upon previous work that has been shown to accurately predict the DNA-mediated crystallization behavior of spherical particles [**3, 14, 4, 13, 99, 100**]; however, the broken symmetry of polyhedra requires additional considerations (SI Discussion and Tables S5-S7). Although the experimentally investigated samples are too large to model exactly, SA and D were scaled to a computationally accessible size regime in a manner consistent with experiments, and DNA density was set based on experiments (Fig. S3 and Tables S8 and S9). In these simulations, a collection of particles was fixed into a lattice with a specified symmetry then allowed to relax at a temperature slightly below the crystal melting temperature to evaluate stability (i.e., whether the structure reaches equilibrium). Through comparison of different lattices for each particle symmetry and size (e.g., a BCC crystalline phase and an FCC plastic crystal), one can evaluate the thermodynamically preferred phase and extract structural parameters from the system, including lattice parameters, the fraction of DNA strands hybridized per particle (F, enthalpic contributions), and the closest average distance between two adjacent DNA strands on a single particle (entropic contributions).

As observed with experiments, the crystalline phase for rhombic dodecahedra was preferred for smaller SA and larger D compared with octahedra (Fig. 4.2 C and F), with both shapes eventually transitioning to plastic FCC crystals. Furthermore, a linearly increased with D for all sizes of rhombic dodecahedra (Table S8) and lattice compression was observed for octahedra in plastic FCC crystals (Table S9), consistent with experiments. Calculations show that the observed transitions originate from ligand-based entropic and enthalpic contributions. In particular, an increased average inter-DNA spacing on the particle and lattice compression both indicate a wider range of

less-oriented DNA states, and thus an increased free volume accessible to each DNA sticky end [**4**]. This flexibility also allows for more DNA connections to be made between particles, as indicated by a greater F.

Based on these results, it was hypothesized that a further reduction in particle symmetry should lead to a smaller zone of anisotropy with a phase transition at larger SA and shorter D. More specifically, the increased sphericity of high-symmetry particles should result in a more diffuse DNA distribution (i.e., reduced number of DNA strands per facet) and a greater free volume available to each DNA strand. Thus, as D increases, the resultant increase in charge repulsion and free volume should not contribute as significantly as they do for lower-symmetry particles.

To test this hypothesis, the crystallization of cubes with comparable SA and D was investigated (Fig. 4.3, Figs. S1 and S2, and Table S4). Cubes densely pack into a simple cubic (SC) crystalline phase, with slight distortions in orientation for mildly truncated or rounded corners, or a plastic or crystalline FCC phase for high degrees of imperfection [**41, 95, 96, 97, 98, 39, 101, 102**]. Indeed, a smaller zone of anisotropy was observed for cubes relative to octahedra and rhombic dodecahedra, consistent with the above hypothesis. Outside of this zone, two phase transitions were observed as SA decreases and D increases that involve a change of Bravais lattice: a first-order transition from an SC crystalline phase to a BCT crystalline phase, followed by a continuous transition to a BCT plastic crystal (Fig. 4.3). The presence of an intermediate crystalline phase with an interaction symmetry distinct from the nanoparticle shape represents an unexpected observation. Interestingly, despite the change from cubic to tetragonal for the first transition, a (i.e., the minor dimension in the square plane for the BCT phase and the only dimension for the cubic phases) increases linearly with D for all investigated SA, with the same rise per base pair as observed for rhombic dodecahedra and octahedra (Fig. 4.3). This result suggests that nanoparticles consistently hybridize to one another along two axes, the (100) and (010) as defined by the symmetry of the final

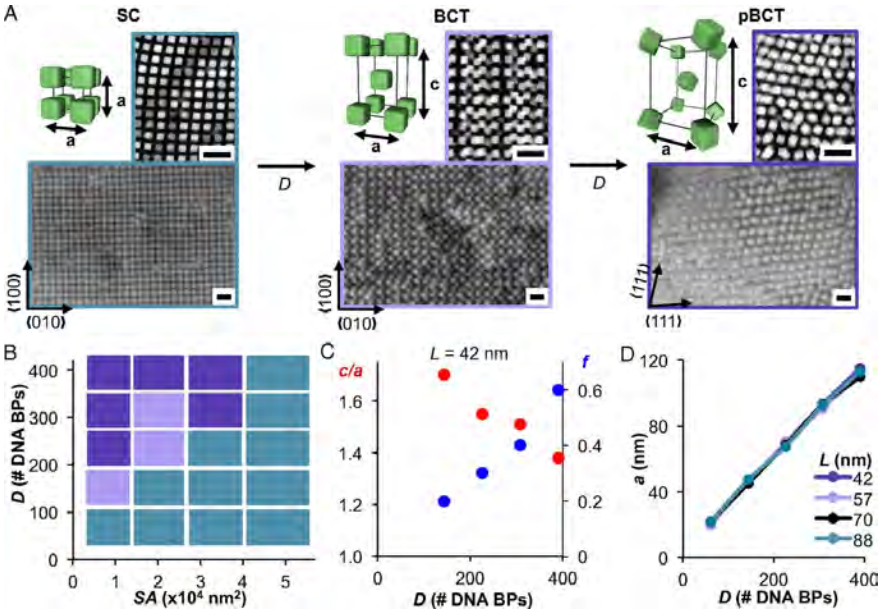

Figure 4.3. Experimental investigation into cube crystallization behavior shows two continuous phase transitions as a function of D and L. (A) As D increases for a given L (shown here as L = 57 nm), cubes crystallize with (from left to right) SC (crystalline), BCT (crystalline), and FCC (plastic) symmetries. For each symmetry, a unit cell is given, with the lattice parameters a and c indicated. Next to each unit cell is a TEM image of silica-embedded lattices sectioned along a particular crystallographic plane. Below each unit cell is an SEM image of silica-embedded lattices, with the lattice vectors indicated at bottom left. (Scale bars, 200 nm.) (B) Phase diagram for cubes as a function of D and SA, colored based on the symmetry - SC (turquoise) or BCT (purple) - where each box is centered on a single experimental data point. (C) For the smallest cube size investigated (L = 42 nm), the data for BCT phases are shown as a function of D. As D increases, c/a decreases and f increases. (D) The lattice parameter, a, increases linearly with D for all L investigated.

lattice, whereas symmetry breaks along the third axis, the (001). The continuous nature of the latter transition can be seen from an orientational order factor (f, ranges from 0 for perfectly oriented to 1 for randomly oriented) determined from comparison between experimental and modeled SAXS data (Fig. 4.3C and Table S4). This change in f occurs as the c/a ratio for the tetragonal unit cell decreases from ~ 1.7 to ~ 1.4 (consistent with an FCC symmetry) (Fig. 4.3C). These results are consistent with our hypothesis that lower-symmetry particles would possess a smaller crystalline region of the phase space, but with more complexity than expected.

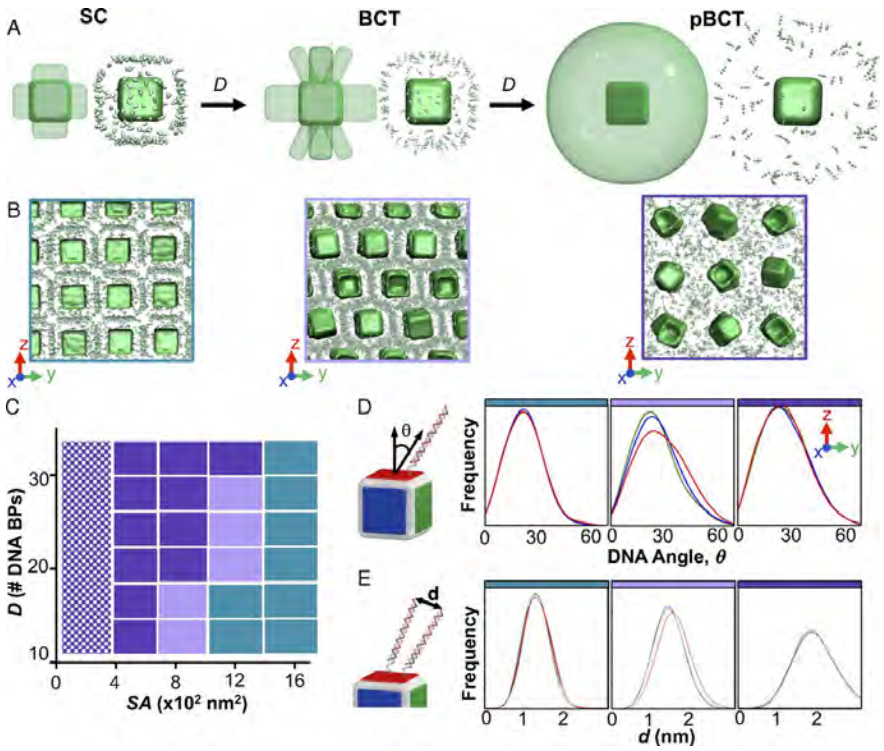

Figure 4.4. MD simulations of cube crystallization reveal that phase transitions occur due to a novel symmetry breaking of the ligand distribution. (A) As D increases in these systems, the distribution of DNA ligands breaks symmetry along the (001). Specifically, the DNA originally on the (001) splits apart and begins to points toward the edges of the (001), such that it can attach to four cubes. As D is increased further, these four interactions become increasingly spaced apart due to electrostatic and free volume arguments. A model (Left) and image from an MD simulation (Right) are shown to indicate the distribution of DNA sticky ends. (B) MD simulations along particular crystallographic planes reveal the distribution of DNA sticky ends between particles. Planes shown are (100) for SC, (100) for BCT, and (110) for the plastic BCT. (C) A phase diagram based on simulation results confirms the same trends in phase and particle orientation as observed in experiment. The colors are consistent with Fig. 4.3 and the checkered region indicates an extrapolation. (D) DNA angle (θ) with respect to an ideal angle of 0 (perpendicular to the surface) shows a broken symmetry for the DNA on the (001) of the BCT crystalline phase only (red). (E) Distance between DNA sticky ends (d) similarly shows that symmetry breaking for the BCT phase occurs away from the particle surface (red). Comparison between the three symmetries further shows that as DNA length increases, the distribution of DNA distances also increases due to the greater free volume accessible.

To understand the origins of these phase transitions, cubes were simulated with MD (Fig. 4.4, Figs. S4-S8, and Table S10). Importantly, phase transitions and lattice parameters consistent with

experiments were observed as a function of SA and D (Fig. 4.4). Close inspection of the spatial distribution and angles of DNA engaged in hybridization shows that the symmetry breaking from SC to BCT phases originates from an unexpected symmetry breaking in the ligand distribution (Figs. S5 and S6). More specifically, the distances between DNA sticky ends are greater on the BCT (001), relative to the BCT (100) and (010), whereas all faces possess equivalent DNA distances in the SC and plastic BCT phases. Similar behavior is observed in the orientation angle of DNA molecules with respect to the nanoparticle surface, wherein larger angles on the BCT (001) indicate reduced face-to-face interactions. Interestingly, the broken symmetry of the DNA distribution becomes more pronounced away from the particle surface, where the DNA can explore a greater free volume. This occurs, in part, because the dense DNA shell near the surface of the particle restricts the position of the DNA. Simulations with and without a dense DNA shell near the surface indeed show that this dense shell is necessary to observe the transition to a BCT symmetry (Fig. S8).

Collectively, these deviations allow each cube in the crystalline BCT lattice to hybridize to four neighbors in a face-to-face fashion along the BCT (100) and (010), similar to SC lattices, but to four neighbors above and four below along the BCT (001). Simulations indicate that the observed transitions predominantly originate from the enthalpy and entropy of the DNA, rather than the packing entropy of the particle shape (Fig. 4.4) [**41, 98**]. In particular, we hypothesize that the DNA shell breaks symmetry as D increases to (i) reduce the electrostatic repulsion associated with a longer DNA backbone, (ii) increase the free volume available to the DNA, especially at the sticky ends (as discussed above), and (iii) ultimately increase the number of DNA hybridization events that connect nanoparticles within the lattice. The lack of a corollary symmetry in the nanoparticle, or preferred orientation of the (001) with respect to the experimental environment or crystallization conditions, suggests that symmetry breaks upon addition to the lattice, driven by

the local DNA environment. These hypotheses are consistent with the transition from crystalline BCT to plastic BCT, and the decrease in the plastic BCT c/a ratio, as D further increases - both of which coincide with an increase in the distance between DNA strands and DNA angle. This unique behavior highlights the importance of considering both particle and ligand effects in nanoparticle crystallization.

This work defines the phase space where directional interactions persist for programmable atom equivalents consisting of anisotropic nanoparticle cores as "atoms" and DNA ligands as "bonds". The understanding gained from this work establishes the range of conditions where design rules based on geometric considerations can be used to predict crystal structure. If these results were extended to lower-symmetry particles (e.g., tetrahedra), one would imagine an even smaller zone of anisotropy and richer phase diagram, including the possibility of quasicrystal or diamond lattices [**41, 98, 39, 103**]. Due to the highly modular and programmable nature of nucleic acids, the location of these phase transitions can likely be tuned depending on the desired structure, via modulation of the design (e.g., flexibility) [**104**] or the type of nucleic acid used (e.g., locked nucleic acid or RNA) [**105**]. Beyond defining the zone of anisotropy, this work also establishes a strategy to assemble nonspherical building blocks into a rich set of different phases based on the interplay of the particle and ligand structure.

CHAPTER 5

Kinetically Controlled Non-Equilibrium Anisotropic Colloidal Single Crystal Growth

Authors: Soyoung E. Seo*, Martin Girard*, Monica Olvera de la Cruz, Chad A. Mirkin

1. Abstract

Anisotropic colloidal crystals are materials with novel optical and electronic properties. However, experimental observations of colloidal single crystals have been limited to relatively isotropic habits. Here, we show that DNA-mediated crystallization of two types of nanoparticles with different hydrodynamic radii leads to the formation of highly anisotropic, hexagonal prism microcrystals with AB2 crystallographic symmetry. We find that the DNA directs the nanoparticles to assemble into a kinetic Wulff crystal structure that is enclosed by the highest surface energy facets ($AB_2(10\bar{1}0)$ and $AB_2(0001)$), an observation supported by molecular dynamics and Monte-Carlo simulations. This behavior is a consequence of the large energy barriers between different terminations of the $AB_2(10\bar{1}0)$ facet, which results in a significant deceleration of the $(10\bar{1}0)$ facet growth rate. In addition to describing a hexagonal crystal habit, which has high enhancement of electromagnetic fields for applications in nonlinear optics and photocatalysis, this work represents an advance where the interface kinetics control the formation of the experimentally observed habit of colloidal microcrystals.

2. Body

The crystal shape (habit) of atomic systems is an external expression of internal structure. The shape that a set of atoms adopts is largely dictated by the configurations of valence electrons unique to each atom and crystallization conditions. In general, an equilibrium shape emerges from the anisotropy of the surface energy, where preferential growth of the lowest surface energy facet is thermodynamically favored[**106, 107**]. Various factors (e.g., pressure, temperature, concentrations) can be used to generate single crystals with different structures and properties[**108**], which inform their use in a variety of applications, including solar cells[**109, 110**] and optical devices[**111, 112**]. For colloidal crystals, recent a priori findings on the properties of three-dimensional (3D) microcrystals composed of inorganic nanoparticles suggest that the use of shape anisotropy is a promising path to designing and controlling optical responses in metamaterials[**113, 114, 19**]. In particular, nano- and microstructures with hexagonal cross-section (e.g., hexagonal wires), which occur naturally in GaN, are interesting because these structures support whispering gallery modes that exhibit low power loss and high quality factors[**115, 116**]. These crystals can be used for nonlinear optics[**117**], an area where nanocomposites excel due to enhancement of nonlinear susceptibility[**118**], or for photocatalysis[**119**]. For colloidal crystals, recent a priori findings on the properties of three-dimensional (3D) microcrystals composed of inorganic nanoparticles suggest that the use of shape anisotropy is a promising path to designing and controlling optical responses in metamaterials[**117, 118, 119**]. However, despite significant interest in emergent properties associated with such structures, this is, as of yet, done empirically because little is known about ways to control mesoscale crystal shape and morphology. Although atomic crystals with unique geometric features have been synthesized by kinetically controlling the growth, kinetic structures in colloidal crystal engineering have been avoided because they are usually random and have many defects.

There are experimental studies reporting unique optical properties of noble metal nanoparticle-based metamaterials. However, these materials are produced through drying and sedimentation techniques that prevent the controllable formation of specific crystal habits[**120, 121, 122**].

To this end, the use of programmable atom equivalents (PAEs) generated from nanoparticles and synthetically tunable DNA ligand shells is a promising route for making ordered, crystalline structures with diverse crystallographic symmetries in a manner that is analogous to atomic crystallization[**5, 87**]. Here, particle interactions driven by the DNA bond afford deliberate architectural control with tunable bond length and strength[**117, 123, 124, 82, 125**]. Indeed, one of the attractive features of this approach is that design rules have been established that allow one to control crystal symmetry, lattice parameter, and habit, independent of particle composition but dependent on particle size and shape[**126, 127, 9**]. Using a slow cooling approach, high-quality 3D single crystals can be produced[**3, 128**]. This strategy has been used to prepare several types of single crystalline architectures, including rhombic dodecahedra, cubes, and octahedra.[**3, 128**] Importantly, all single crystal systems studied thus far have been limited to structures with cubic symmetry, and therefore the high symmetry internal packing provides access to only a small number of isotropic crystalline shapes.

Experimental observations of single crystals have been restricted to PAEs with similar hydrodynamic radii (a combination of the nanoparticle radius and the DNA length). Here, we show that combining nanoparticles of different sizes can alter the interface kinetics in the system, leading to the formation of highly anisotropic single crystals. The AB_2 (isostructural with the intermetallic phase aluminum diboride) structure yields elongated hexagonal prism microcrystals upon slow cooling. Importantly, these anisotropic microcrystals can be realized from the AB_2 structure with different lattice parameters. The experimental results are corroborated with theoretical studies and suggest that the formation of highly anisotropic single crystals is facilitated by anisotropy in the

interface kinetics, where the fast-growing facets "grow out" and disappear, and the slow-growing facets, $AB_2(10\bar{1}0)$ and $AB_2(0001)$ (the facet normal to the $AB_2(10\bar{1}0)$), are present in the final shape. It is important to note that based on molecular dynamics (MD) simulation results, the facets enclosing the crystals have the highest surface energies contrary to usual equilibrium Wulff constructions. Such crystal growth behavior stems from the nucleation barrier between each termination of $AB_2(10\bar{1}0)$, which significantly decelerates the growth rate due to the energetic penalty involved in nucleation of a layer with a high surface energy atop a layer with a low surface energy. The results shown in this work present a solution to a synthetic and materials challenge in colloidal crystal engineering that had not been addressed previously, where the deviation from minimal energy shapes and the broken bond model picture enables the synthesis of anisotropic colloidal crystals, and suggest that external parameters, such as ionic strength, temperature, and stress, could be used to control colloidal crystallization. The ability to design and generate colloidal crystals with desired crystal shape is crucial for the fabrication of next-generation optoelectronic devices since optical modes are dependent on crystal shape. [**113, 19**]

In order to realize colloidal crystals with a highly anisotropic shape, three main principles were identified: (i) the combination of two types of particles should form lattices with a crystallographic symmetry other than cubic (e.g., the hexagonal single crystals can only be generated from hexagonal lattices), (ii) the selected structure should have no competing structures to minimize defects which will inhibit single crystal growth, and (iii) the difference in growth rates of different planes should be large enough to favor the dominant growth of a specific surface facet(s) and, therefore, one preferred type of single crystal. DNA-mediated assembly of nanoparticles represents an ideal means to control the internal packing because the assembly behavior of PAEs is well-understood based on the complementary contact model[**5**] and potential energy calculations[**129**]. PAEs enable one to deliberately and independently toggle nanoparticle size, composition, bond strength,

and interparticle spacings, while maintaining a desired crystal symmetry in a controllable fashion. Specifically, the ratio between the hydrodynamic radii of the building blocks was used as a design parameter to produce the microcrystals presented in this work. To test our principles for the assembly of highly anisotropic microcrystals, superlattices with crystallographic symmetry identical to AlB_2 were chosen as a model system as this structure meets our criteria.

In order to make colloidal crystals with AB_2 symmetry, pairs of PAEs (with hydrodynamic radius ratios between 0.5 and 0.8) were synthesized based upon the previously established colloidal crystal engineering design rules[**5**]. The slow cooling of two sets of PAEs with complementary DNA linker strands produces microcrystals with the AB_2 packing when hydrodynamic radius ratio (β/α) of the PAEs falls within this range (Fig. 5.1a). The hydrodynamic radius of each PAE was determined by calculating the DNA length and adding it to the core radius (Supplementary Eq. 1). The internal ordering of the PAE superlattices was confirmed by 1D radial line averages of the small angle X-ray scattering (SAXS) patterns (Fig. 5.1b). The surface features and the overall crystal shape were determined by scanning electron microscopy (SEM), where images of the hexagonal prismatic microcrystals reveal uniform single crystals defined by six rectangular-shaped faces and two hexagonal-shaped bases (Fig. 5.1c, d(i)). In addition, high-resolution SEM images show extraordinarily well-formed crystals with smooth crystal facets, consisting of highly ordered nanoparticles (Fig. 5.1d(ii)).

Faceted hexagonal prism microcrystals were obtained with ten different unit cells that are isostructural with the AlB_2 lattice, but with different a and c values (Fig. 5.2). The AB_2 colloidal crystal superlattice (space group 191) is a hexagonal unit cell with two distinct types of particles, where the structure consists of layers of hexagonally arranged large particles with small particles in every trigonal prismatic interstice (Fig. 5.1b bottom). Unlike the AlB_2 structure found in atomic systems where the c/a ratio is fixed to 1.08, the c/a ratio for PAE superlattices is tunable

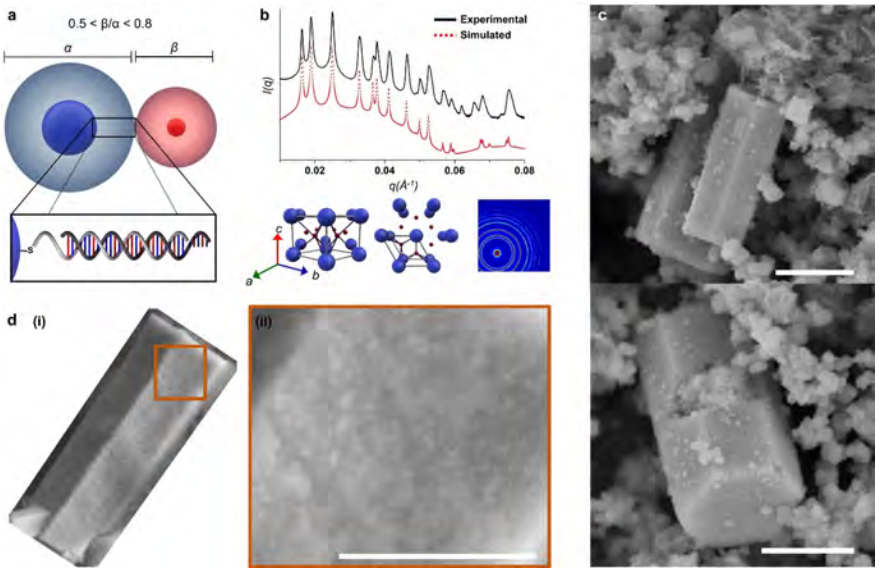

Figure 5.1. **Hexagonal prism microcrystals formed from DNA-functionalized nanoparticles. a,** Scheme of a set of DNA-functionalized gold nanoparticles with a hydrodynamic radius ratio (β/α) between 0.5 and 0.8 used to produce superlattices with AB_2 crystallographic symmetry. α and β denote hydrodynamic radii of particles A and B. **b,** Representative one-dimensional (top) and two-dimensional (bottom, right) SAXS data for AB_2 superlattices assembled from the slow cooling approach. Different views of the AB_2 unit cell (bottom, left) are shown for reference. SAXS data are shown as plots of the overall scattering intensity from a crystal domain ($I(q)$, in arbitrary units) versus scattering vector (q, in units of -1). **c,** SEM images of hexagonal prism microcrystals in different orientations. **d,** SEM images of a representative microcrystal with visible faceting (**i**) where constituent nanoparticles can be seen (**ii**). Scale bars are 1 μm. Courtesy of Eileen Soyoung Seo

and controlled by the hydrodynamic radius of each component, which can be varied by changing either the nanoparticle size or DNA length (Fig. 5.2). The rationale for achieving a range of c/a ratios with identical crystallographic symmetries can be described using a basic principle in DNA-driven nanoparticle superlattice engineering: colloidal crystals generated from rigid nanoparticles and soft, DNA ligand shells can tolerate unfavorable repulsive interactions if the system can access a more thermodynamically stable structure (i.e., the PAEs can elastically compress along the c-axis or across the ab-plane if they can be in more thermodynamically favorable positions)[**129, 130, 12**]. Importantly, the fact that the c/a ratio is tunable suggests that the relative strength of attractive and

repulsive forces between PAEs can be varied using individual PAE structure as a design parameter. Furthermore, we show that salt concentration can alter the c/a ratio. The DNA shells around the nanoparticle core can be compressed with the addition of salt, which decreases the repulsion between DNA strands within the overlap region and results in compression of the superlattice. Significantly, this is not isotropic since the lattice itself is not symmetric. With these observations, one can choose PAEs and salt conditions to produce microcrystals with structural parameters that favor the Wulff shape.

To fully understand why such crystals form, one needs to understand the growth kinetics of such structures. Indeed, the formation of hexagonal prisms from an AB_2 packing of nanoparticles can be explained by the kinetic growth of the exposed facets, where the crystal is enclosed by the slowest-growing facets. In other words, kinetic anisotropy in the growth rates can dictate shape selection, as described by the kinetic Wulff construction[**131**]. Wulff made a direct correlation between the surface energy and growth rate[**106**]. This assumption led to the conclusion that the lowest surface energy facet, which has the slowest growth rate in simple systems, is exposed in the final shape. Previously observed Wulff polyhedra were formed from one-component systems[**3, 128**], where all particles are equivalent from a kinetic standpoint, and thus the surface energy can be directly correlated to the growth rate to predict the thermodynamic shape. This correlation does not hold in all cases, specifically in multicomponent crystallization. In a binary system such as an AB_2 lattice, the diffusion and attachment kinetics of each component (A and B) are expected to be different, and this can significantly contribute to the observed crystal shape, resulting from either diffusion-limited or interface-limited growth[**131, 132, 133**]. Furthermore, unlike one-component cubic lattices, the same Miller indices can be assigned to different planes. Indeed, unlike previously observed Wulff polyhedra[**3**], the lowest surface energy facet is not exposed in these AB_2 crystals (Fig. 5.7). Based on the calculation of relative effective surface energies ($\gamma^{\S}$)

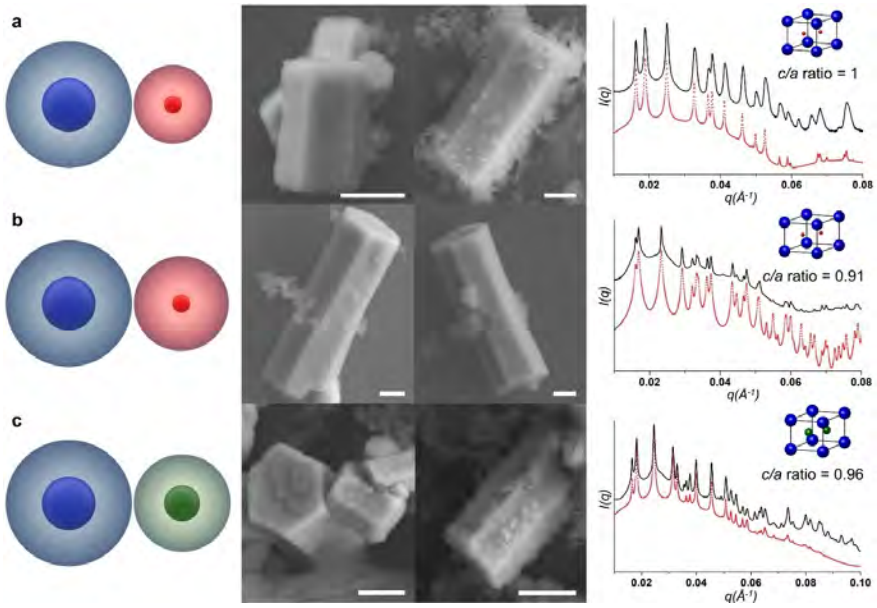

Figure 5.2. **Hexagonal prisms with varying unit cell compositions. a-c,** SEM images (middle) and one-dimensional SAXS patterns (right) of hexagonal prism microcrystals from an AB_2 lattice synthesized from different sets of PAEs to achieve a range of (β/α): (**a**) 0.67, (**b**) 0.73, and (**c**) 0.80 (scheme shown on left). The systems shown in (**a**) and (**b**) each consist of a pair of nanoparticles; one has an Au core diameter of 15 nm and the other is 5 nm. In the case of the small particle, the hydrodynamic radius was deliberately changed by changing the thickness of the DNA shell so that the β/α in (**b**) is greater than in (**a**). The system in (**c**) used the same 15 nm Au core PAEs that were used in (**a**) and (**b**), but the hydrodynamic radius was varied by changing the Au core diameter of the small particle (10 nm in diameter) so that the β/α in (**c**) is greater than in (**a**). In the SAXS patterns, the black trace is the experimentally obtained scattering pattern, and the red trace is the predicted scattering pattern for a model lattice. The lattice parameters from SAXS results were used to calculate the c/a ratio of each unit cell. Scale bars are 1 μm. Courtesy of Eileen Soyoung Seo

for different AB_2 facets (Table 5.4), the $AB_2(11\bar{2}0)$ plane has the lowest surface energy. The equilibrium crystal structure predicted from a Wulff construction is not the experimentally observed elongated hexagonal prism morphology, confirming that the observed hexagonal prismatic crystals are kinetic products (Fig. 5.7, 5.8). Consistent with this conclusion, SEM analysis of the surface of the microcrystal reveals that the hexagonal prisms are enclosed by the highest surface energy

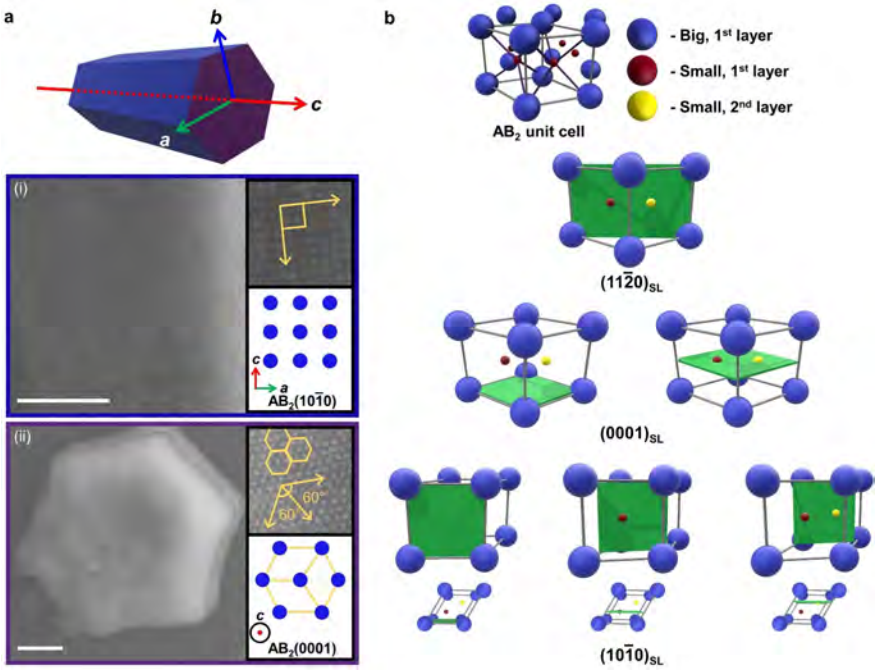

Figure 5.3. **Surface features of hexagonal prism microcrystals. a,** Scheme of a hexagonal prism (top) and SEM images (bottom) of (**i**) a rectangular face with a $(10\bar{1}0)$SL (inset) and (**ii**) a hexagonal base with a (0001)SL (inset) of a hexagonal prism. For clarity, rectangular faces and a hexagonal base are color coded as blue and purple both in scheme and SEM images, respectively. b, Scheme of an AB2 unit cell and the projections of the $(11\bar{2}0)$SL, (0001)SL, and $(10\bar{1}0)$SL planes. The plane multiplicity can be determined by counting the number of different planes (green slabs) that correspond to the same Miller indices. Nanoparticles in different colors may occupy different layers of a plane with identical Miller indices. Grey and purple lines in the model lattice denote the edges of the unit cell and the bonds that connect complementary particles, respectively. Top-down views of different planes of the $(10\bar{1}0)$SL facet is shown for clarity. Courtesy of Eileen Soyoung Seo

facets: the rectangular faces are $(10\bar{1}0)$ facets (Fig. 5.3a(i), b, c(i)) and the hexagonal ends are (0001) facets (the facet normal to the $(10\bar{1}0)$ facet; Fig. 5.3a(ii), b, c(ii)).

The crystal growth rate is dependent upon many variables (e.g., PAE diffusion rate, chemical potential, termination effect) that vary as a function of both particle and facet type[**131, 132**]. For the PAE system where the crystals are grown by slow cooling over several days through the melting temperature (i.e., particles were given enough time to equilibrate), we hypothesize that single crystal formation is less likely to be diffusion-limited. To explore whether the difference between

the chemical potentials of each component plays a role in crystal growth, off-stoichiometry (i.e., a ratio of A:B particle mixtures not equivalent to 1:2) experiments were carried out with 1:3 and 1:6 molar ratios of A:B. The observed crystal habits in these systems are the same as those observed in the stoichiometric system, suggesting that the chemical potential difference has a negligible influence on crystal shape (Fig. 5.4). For multicomponent systems, the composition of the particle (type) terminating the crystal surface can affect the overall growth kinetics, as described by termination effects observed in atomic crystals, for example, III-V semiconductors such as GaAs36. For an AB_2 lattice, each crystal plane corresponding to a set of identical Miller indices can exhibit a multiplicity up to three; that is, the number of distinct planes with the same Miller indices is three (Fig. 5.3b). For example, the $AB_2(10\bar{1}0)$ plane has a multiplicity of three (blue, red, or yellow) while the $AB_2(11\bar{2}0)$ plane has a multiplicity of one as it intersects all particles within a unit cell (Fig. 5.3b, Fig. 5.2). We therefore calculated the actual surface energies for different surface terminations using molecular dynamics simulations. These calculations reveal that different surface terminations have different surface energies when a set of Miller indices exhibits a multiplicity greater than one, and this difference in surface energy, which is the largest for the $AB_2(10\bar{1}0)$ plane, creates a nucleation barrier for the growth of the subsequent layer (Table 5.1). This is especially true when a layer with a higher surface energy nucleates atop of a layer with a lower energy.

For the typical kinetic Wulff shape construction, the growth of layers occurs through the formation of a terrace, which then forms a complete monolayer before the subsequent growth of the next layer (Fig. 5.5a top). For such growth, the growth rate, r, can be expressed as $r = f_0 \exp(-E/k_B T)$, where f_0 is the prefactor and E is the nucleation barrier ($E = -\pi(\gamma_e)^2/\Delta\mu$; γ_e is the edge energy per atom of a terrace and $\Delta\mu$ is the bulk chemical potential drive, which is negative for crystal growth)[**131**]. For facets with a multiplicity greater than one, the nucleation of an additional particle results in a change in the overall surface energy akin to a change in the

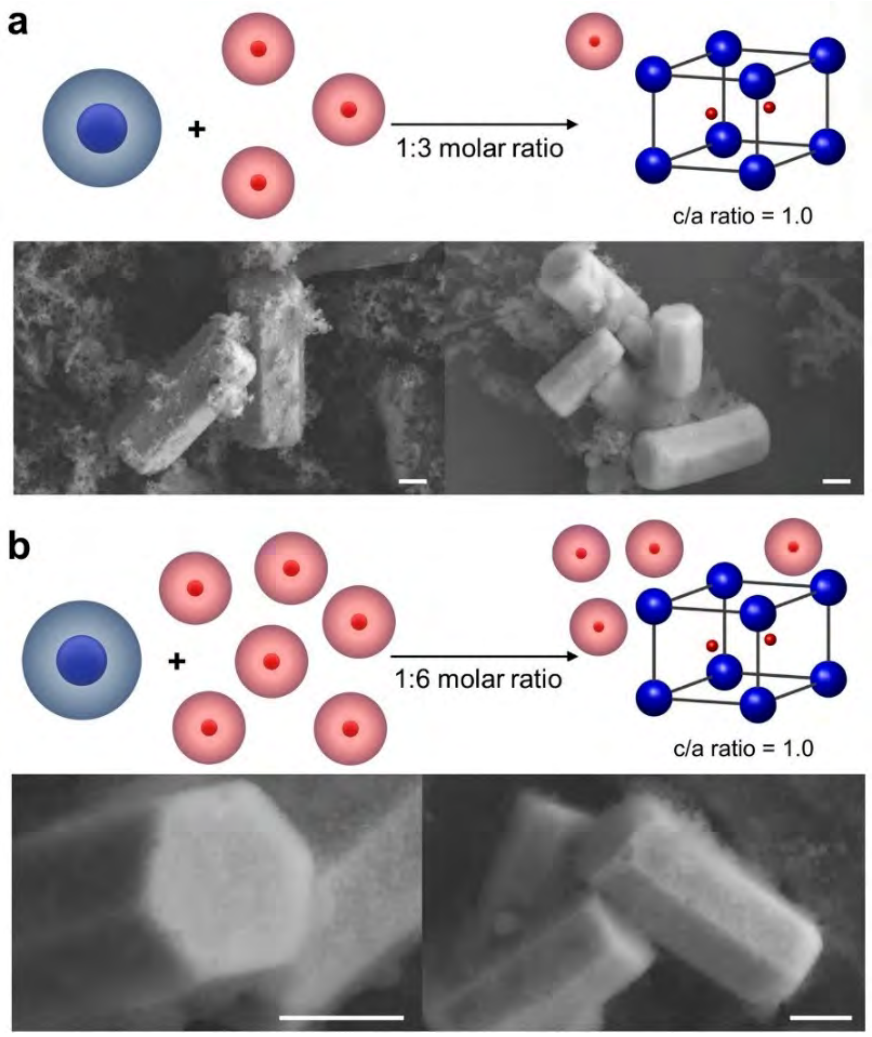

Figure 5.4. **Hexagonal prisms produced upon addition of off-stoichiometric ratios of PAEs. a-b**, Scheme (top) and SEM images (bottom) of hexagonal prism microcrystals when different molar ratios of A:B particles, (**a**) 1:3 and (**b**) 1:6, were added. In both cases, AB_2 lattices have a similar c/a ratio to the one formed using a stoichiometric ratio of PAEs (1:2). Scale bars are 1 μm. Courtesy of Eileen Soyoung Seo

bulk chemical potential (Table 5.1). When the growth of a layer is energetically unfavorable, the nucleation of a subsequent layer may occur before growth of the initial layer is complete, resulting in multi-terrace type growth (Fig. 5.5a bottom). To better understand the growth mechanism relevant to our system, we derived equations for a simple two-layer system, where layer "A" has lower surface energy than layer "B". The energy barrier E for the growth of A on B and B on A are given

by $E_{A/B} = -\pi(\gamma_e)^2/(\Delta\mu + \Delta\gamma_{AB})$ and $E_{B/A} = -\pi(\gamma_e)^2/(\Delta\mu - \Delta\gamma_{AB})$, respectively, where $\Delta\gamma_{AB}$is the difference in surface energy of layers A and B (measured per particle). Based on this model, when $|\Delta\mu|$ is same as $|\Delta\gamma_{AB}|$,there is no thermodynamic driving force for the nucleation of the higher surface energy layer B. In this case, the crystal growth proceeds through the growth of a BA bilayer as the growth of A on B occurs significantly faster than the growth of B on A. Therefore, E_{BA} can be written as$-2\pi(\gamma_e)^2/\Delta\mu$. If this is the growth mechanism that the PAEs undergo, one would expect to recover the thermodynamic Wulff shape, however, this is not experimentally observed (Supplementary Fig. 5.3). Therefore, we hypothesize that the growth mechanism that leads to the formation of hexagonal prism microcrystals from an AB_2 packing of nanoparticles is layer-by-layer growth, as described in the kinetic Wulff construction.

To investigate this hypothesis, we used a solid-on-solid model in kinetic Monte-Carlo simulations to evaluate the effect of a nucleation barrier on the growth kinetics for the plane with a multiplicity of two. Here, layer growth can proceed through two different pathways as illustrated in Fig. 5.5c-h (see Section 5.2 for additional discussion). At lower values of $\Delta\gamma_{AB}$ (below 0.3 k_BT in Fig. 5.5b), layer growth is significantly slowed but still proceeds in a layer-by-layer fashion. Whereas, when the $\Delta\gamma_{AB}$ value is above $\sim$0.24 k_BT (where the curve starts to plateau), we observe the formation of BA terraces (Fig. 5.5a bottom, e, h). Thus, for the microcrystals experimentally observed, the PAEs are expected to exhibit a layer-by-layer growth behavior, which results in a kinetic Wulff crystal (Fig. 5.5c). The strong parallels between the energy barrier calculations and simulation results indicate that the plane with the largest $\Delta\gamma_{AB}$ is present in the final shape through a layer-by-layer growth mechanism. Importantly, the kinetic Wulff shape, a hexagonal prismatic crystal bounded by the $(10\bar{1}0)$ and (0001) facets, is predicted by setting the growth speed of the $AB_2(10\bar{1}0)$ (the facet with the greatest $\Delta\gamma_{AB}$ in our system) to zero (Supplementary Fig. 4).

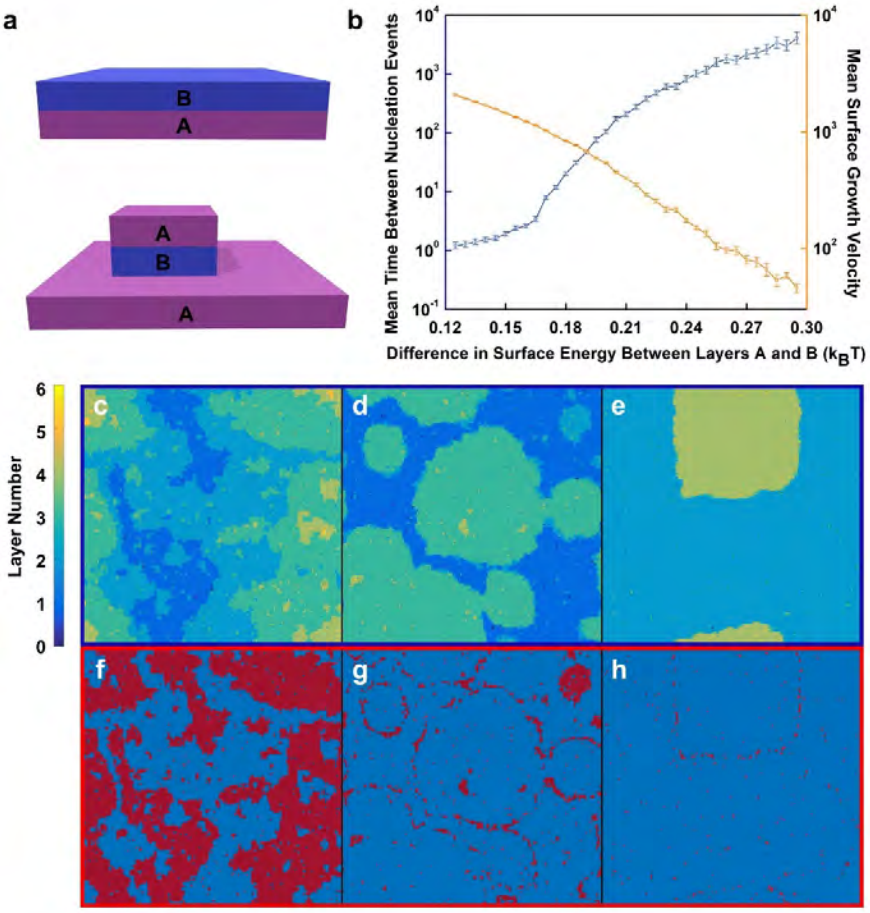

Figure 5.5. **Kinetics of epitaxial growth of alternating layers of A and B calculated using Monte-Carlo simulations** ($_e = 0.65k_BT$, $\Delta\mu = -0.3k_BT$). **a,** Representative scheme of layer growth mechanisms in the presence of a minimal or no energy barrier (top) and a substantial energy barrier between A and B layers (bottom). **b,** The mean time between nucleation events and the mean surface growth velocity plotted as a function of the energy barrier between layer growth. Error bars indicate 95% confidence interval. **c, d, e,** Typical surface profiles for $\Delta\gamma_{AB}$ = 0 k_BT, 0.12 k_BT and 0.29 k_BT, respectively. **f, g, h,** The same surface profiles colored with the low energy layer in blue and the high energy layer in red. The color scheme presented in **f, g, h** allows one to clearly view the placement of the high energy layer. As the energy barrier increases between layers, the presence of layer B is suppressed and is eventually only found near the terrace edges.

In conclusion, this work is important for the following reasons. First, this work documents the first example of non-equilibrium colloidal single crystals with uniform shapes. We have further elucidated a guide for designing and synthesizing crystal habits via kinetic control, which can in turn

lead to rational design of colloidal single crystals with better optical properties. Moreover, it shows for the first time how DNA programmable assembly can be used to synthesize highly anisotropic, hexagonal prisms. Importantly, different nanoparticle sizes and oligonucleotide lengths can be used to realize crystals that are isostructural on the mesoscale but with deliberately varied nanoscale interiors. The combination of experiment, theory, and simulation convincingly shows that the observed anisotropic products are a consequence of kinetically controlled crystal growth, exposing the highest surface energy planes. Collectively, this work expands the design space of colloidal crystal engineering where macroscopic control over crystal habit is possible, thereby potentially resulting in structures that have potential for a wide range of applications, spanning sensing and single crystal optics.

3. Methods Summary

All oligonucleotides used in this work were synthesized on a solid-support MM12 synthesizer using phosphoramidites purchased from Glen Research. Sequences can be found in the Supplementary Information. DNA-functionalized nanoparticles were synthesized and assembled according to published literature protocols[**5, 123**]. A solution containing PAE aggregates were slow cooled to room temperature in a temperature cycler (Life Technologies) at a starting temperature above the aggregate melting temperature and at a rate of 0.01 °C min^{-1}. Structures of superlattices were characterized by synchrotron SAXS experiments conducted at the Advanced Photon Source at Argonne National Laboratory. For visualization by SEM (Hitachi SU8030), superlattices were embedded in silica for transfer to the solid state[**134**]. More experimental and simulation details, and surface energy calculation values can be found in the Supplementary Information.

4. Acknowledgments

We thank Prof. Laurence Marks and Prof. Michael Bedzyk for their helpful discussions about crystal growth. This work was supported by the following awards: the Center for Bio-Inspired Energy Science, an Energy Frontier Research Center funded by the U.S. Department of Energy, Office of Science, Basic Energy Sciences Award DE-SC0000989 (oligonucleotide syntheses and purification, simulations and theory); the Air Force Office of Scientific Research Award FA9550-17-1-0348 (DNA-functionalization of gold nanoparticles); the Asian Office of Aerospace Research and Development Award FA2386-13-1-4124 (nanoparticle superlattice assembly); and the National Science Foundations Materials Research Science and Engineering Center program (DMR-1121262) and made use of its Shared Facilities at the Materials Research Center of Northwestern University (SEM characterization). SAXS experiments were carried out at beamline 5-ID of the DuPont-Northwestern-Dow Collaborative Access Team at the Advanced Photon Source. Use of the Advanced Photon Source at Argonne National laboratory was supported by the U.S. Department of Energy, Office of Science, Office of Basic Energy Sciences, under Contract No. DE-AC02-06CH11357 (SAXS characterization). S.E.S. acknowledges partial support from the Center for Computation and Theory of Soft Materials Fellowship. We thank Prof. Laurence Marks and Prof. Michael Bedzyk for their helpful discussions about crystal growth. Author Contributions S.E.S. and C.A.M. designed experiments and analyzed data. M.G. developed the theoretical model and performed simulation. M.G. and M.O.d.l.C analyzed simulation data. All authors contributed to writing the manuscript.

Layer type	$\Delta\gamma_p(11\bar{2}0)$	$\Delta\gamma_p(0001)$	$\Delta\gamma_p(10\bar{1}0)$	$\Delta\gamma_p(11\bar{2}1)$	$\Delta\gamma_p(10\bar{1}1)$
1	-	0.093	-0.079	-0.030	0.022
2	-	-0.093	-0.122	0.030	-0.142
3	-	-	0.201	-	0.120

Table 5.1. Relative difference in surface energy values between different layers calculated for DNA-gold nanoparticle superlattices

5. Supplementary information

5.1. Surface energy calculations and Wulff shape prediction

To explore the contribution of surface energies of different facets on the shape selection, molecular dynamics simulations were carried out to understand the origin of facet yield changes. The coarse-grained approach used in this work is the same as the one demonstrated in previous literature, which used a model first developed by Knorowski et al[**13**] and then adapted for double-stranded DNA (dsDNA) by Li et al[**14**]. MD simulations used a PAE design similar to the one used in experiments.

To calculate the surface energies of a unit cell, we used two different systems, a perfect 3D crystal and a slab of finite thickness in the $z-$direction, with a defined surface plane (Fig. 5.6). Distances between the nanoparticles were determined from the equilibrated lattices. To equilibrate a lattice, we initialized colloids in a perfect crystal and let the system relax using the isobaric-isothermal ensemble (NpT). We equilibrated systems of $4 \times 4 \times 4$ and $6 \times 6 \times 6$ unit cells with relative differences in mean energy and lattice parameters of less than 10^{-3}. We considered a few, different systems with varying DNA lengths to find the system similar to the experimental one, while keeping the particle sizes constant. The double-stranded portion was fixed for all systems while the single-stranded segment (ssDNA), which represents the PEG linker region in our DNA design, was varied. Table 5.2 summarizes the values used for lattice equilibration.

System	dsDNA length (# of bases)	Particle A ssDNA length (# of bases)	Particle B ssDNA length (# of bases)	a (nm)	c (nm)	c/a
A	16	10	4	40.52	36.51	0.901
B	20	10	4	44.34	39.56	0.892
C	16	10	10	42.31	37.00	0.875
D	16	14	14	44.50	38.82	0.872

Table 5.2. DNA Lengths and Equilibrated Lattices

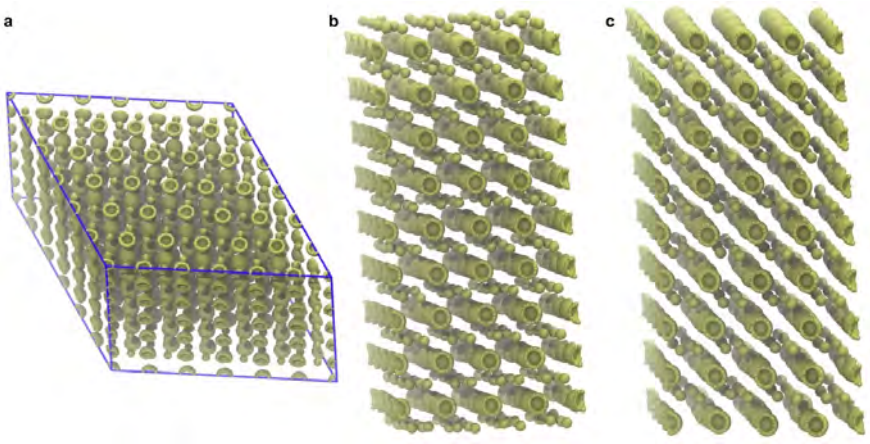

Figure 5.6. Simulation snapshots of **a**, a perfect 3D crystal with $6 \times 6 \times 6$ unit cells, and **b** and **c**, surface slabs showing two different terminations of the (0001) plane.

As for our previous surface energy calculations[**128**], we did not fix the positions of the colloids. This allows the surfaces to undergo simple reconstructions where the colloids are displaced with respect to the bulk crystal lattice. Each crystal slab has at least six crystal periods in the $z-$direction and 4 periods in the $x-$ and $y-$directions. Crystal slabs typically have 112 to 160 colloids of type A and 256 to 320 colloids of type B, yielding a typical 650k to 1M beads in the system. Since the unit cell of an AB_2 crystal has three distinct points, we have up to three different surface terminations. The three different terminations were evaluated for all Miller indices, including the ones that are equivalent to confirm that the surface energies calculated herein are

Plane	$(11\bar{2}0)$	(0001)	$(1\bar{1}0)$	$(11\bar{2}1)$	$(10\bar{1}1)$
Multiplicity	1	2	3	2	3

Table 5.3. Summary of Multiplicity of Different Set of Miller Indices

reproducible. Calculations were performed twice for each set of Miller indices. Tools to generate initial configurations can be found online (https://bitbucket.org/NUaztec/hoobas). The number of distinct surface terminations for a given set of Miller indices depends on the number of points crossed in the unit cell (Fig. 5.3). Multiplicity numbers for different planes are given in Table S5.3.

5.1.1. Surface Energies. The surface energy of a given crystal plane was obtained using the difference in enthalpy between the crystal slab with exposed facets (Fig. S5.6) and a perfect crystal. The surface enthalpy is given by:

$$\gamma_p = \frac{U_p - U_A n_A - U_B n_B}{A_p} \tag{5.1}$$

where γ_p is the surface energy of a given plane, U_p is the enthalpy of the crystal slab with exposed plane p, U_A (or U_B) is the mean energy of colloids of type A (or B) in a perfect crystal, and n_A (or n_B) is the number of colloids of type A (or B) in the crystal slab. The mean of the relative variation between repeat calculations of the surface enthalpy is around 4%.

Simulations are performed in the NVT ensemble using a Langevin thermostat (friction coefficients of 1.0). The crystal structure is thermally equilibrated over 1.5×10^6 timesteps, while energy is measured with 500 values taken over 2.5×10^6 timesteps with a timestep of $\Delta t = 3 \times 10^{-3} \delta t$ and $\delta t = (m\sigma^2/\epsilon)^{1/2}$.

5.1.2. Wulff shape identification. The thermodynamic equilibrium shape of a lattice is governed by the stability of crystal surfaces, and thus the shape can be computationally predicted based on

Name	$\gamma^{\S}(11\bar{2}0)$	$\gamma^{\S}(0001)$	$\gamma^{\S}(1\bar{1}0)$	$\gamma^{\S}(11\bar{2}1)$	$\gamma^{\S}(10\bar{1}1)$	Ratio of surface energies
A	0.508	0.721	0.529	0.534	0.510	1:1.42:1.04:1.05:1
B	0.411	0.571	0.431	0.424	0.404	1:1.39:1.05:1.03:0.98
C	0.474	0.649	0.485	0.487	0.470	1:1.37:1.02:1.03:0.99
D	0.425	0.590	0.440	0.445	0.434	1:1.39:1.04:1.05:1.02

Table 5.4. Effective Surface Energy Values Calculated AB_2 Superlattice. $\gamma^{\S}$ represents effective surface energies (in kJ/mol/nm^2), which is the lowest surface energy value among values calculated for different terminations

Name	Termination type	$\gamma_p(11\bar{2}0)$	$\gamma_p(0001)$	$\gamma_p(1\bar{1}0)$	$\gamma_p(11\bar{2}1)$	$\gamma_p(10\bar{1}1)$
A	1	0.508	0.814	0.651	0.534	0.652
A	2		0.721	0.529	0.564	0.510
A	3			0.730		0.630
B	1	0.411	0.614	0.546	0.424	0.528
B	2		0.571	0.431	0.451	0.404
B	3			0.576		0.495
C	1	0.474	0.717	0.612	0.487	0.608
C	2		0.649	0.485	0.539	0.470
C	3			0.685		0.569
D	1	0.425	0.662	0.573	0.445	0.547
D	2		0.590	0.440	0.472	0.434
D	3			0.597		0.518

Table 5.5. Slab Calculation Values for Different Terminations. γ_p represents surface energy values (in kJ/mol/nm^2) for different terminations of a plane with identical Miller indices. Termination type 1 always has the large particles on the surface.

surface energy values. Using surface energy values estimated from the MD simulations, we calculated the ratio of surface energies and used the WulffMaker software to predict corresponding Wulff polyhedra[**135**]. Fig. 5.7 shows the corresponding thermodynamic Wulff polyhedra predicted from the surface energies for the lattice with experimentally determined lattice parameters.

5.2. Kinetic Monte-Carlo simulations

5.2.1. Methods. To probe the termination effect on the growth speed of facets, we performed a kinetic Monte-Carlo simulation of epitaxial growth of a surface with alternating layers of A and B.

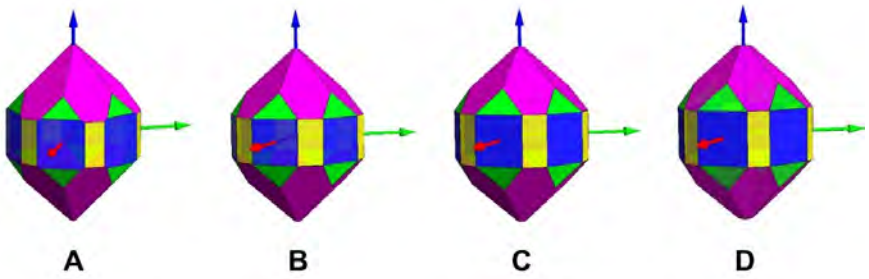

Figure 5.7. Wulff polyhedra simulated for different systems (Table 5.2) exhibit similar crystal habits and deviate from the experimental results. All crystals are truncated by the $AB_2(11\bar{2}0)$ blue, $AB_2(0001)$ purple, $AB_2(10\bar{1}0)$ yellow, $AB_2(11\bar{2}1)$ green, and $AB_2(10\bar{1}1)$ magenta facets.

As a toy model, we used a square lattice for the growth of a 160×160 unit cell. The bulk chemical potential of each layer was set to $\Delta\mu = -0.30 k_B T$, with an edge energy of $\gamma_e = 0.65 k_B T$. The surface energy difference $\Delta\gamma_{AB}$ was varied from 0 to 0.29 $k_B T$ and the mean surface height (as a function of time) was recorded to generate a graph shown in Fig. 5.9. This allowed us to calculate the mean growth rate of a system with different energy barriers. We recorded the mean time spent on low energy layers, discarding the results where multiple growth events occurred at the same time. A clear increase in the mean time is observed when $\Delta\gamma_{AB} > 0.15$. This indicates that beyond certain amount of $\Delta\gamma_{AB}$, the epitaxial growth transitions from a monolayer to a multilayer growth (Fig. 5.5). In the case where a very low number of layers is grown for large $\Delta\gamma_{AB}$ ($2 - 3$ layers), it generates a large confidence interval. For small values of $\Delta\gamma_{AB}$, particle nucleation proceeds quickly and can be faster than the time it takes for a terrace to fully grow, yielding no plateau. These values are discarded from the fitting process. Confidence intervals for the mean surface growth is determined by splitting the mean surface height in 10 different bins and calculating their standard deviation.

5.2.2. Choice of parameters and growth mechanism. As illustrated in Fig. 5c, at $\Delta\gamma_{AB} = 0$, the $\Delta\mu$ and γ_e values considered in these simulations results in rough surface. For the Wulff

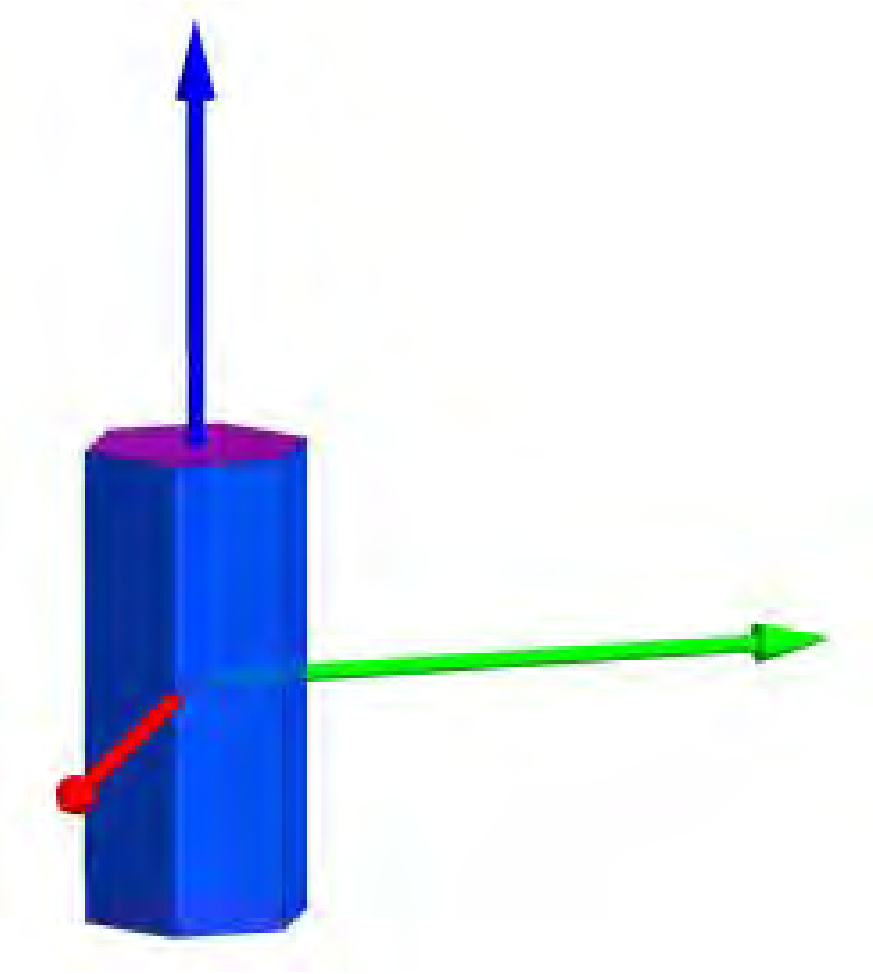

Figure 5.8. Wulff equilibrium shape is predicted for the case when the growth velocity of the $AB_2(10\bar{1}0)$ is assumed to be very slow. Because the Wulffmaker software can only generate the shape based on the surface energy values, the surface energy of the $AB_2(10\bar{1}0)$ was set as the lowest value, which is equivalent to the slowest growth velocity). Hexagonal prism is truncated by blue $(10\bar{1}0)$ and purple (0001) faces.

equilibrium crystal structures observed in previous experiments[**97, 3**], all colloids are equivalent to each other, and thus $\Delta\gamma_{AB} = 0$. Therefore, the simulation results displayed do not agree well with the experimental results. Although the parameters chosen in this study are not ideal values to model experiments, we will discuss several reasons why these parameters were chosen.

Based on the equations derived in the main text, for small values of $\Delta\gamma_{AB}$ the mean growth velocity is predicted to be inversely proportional to $E_{A/B} + E_{B/A}$. For large values of $\Delta\gamma_{AB}$, it should be inversely proportional to E_{BA}. These values can be directly correlated to the mean time between nucleation events shown in Fig. 5.5b; yet, a more dramatic change is observed for the mean time than the growth velocity. This is because multiple nucleation events are occurring within the time frame of a monolayer growth. For the expected layer-by-layer growth, these two curves should display stronger correlations.

Using either a smaller value of $\Delta\mu$ (in magnitude) or a greater value of γ_e in the simulations leads to a smooth surface (Fig. 5.10) as observed in previous experiments. However, in this case, the growth is significantly slowed, especially with large $\Delta\gamma_{AB}$ and poor statistics, resulting in growth of only a few layers in the simulations. Nevertheless, Fig. 5.10 illustrates that the calculations performed in this work exhibit an anticipated trend where the growth is dramatically slowed and the mean time between nucleation events increases. The full curve beyond $\Delta\gamma_{AB} = 0.3k_BT$ cannot be obtained.

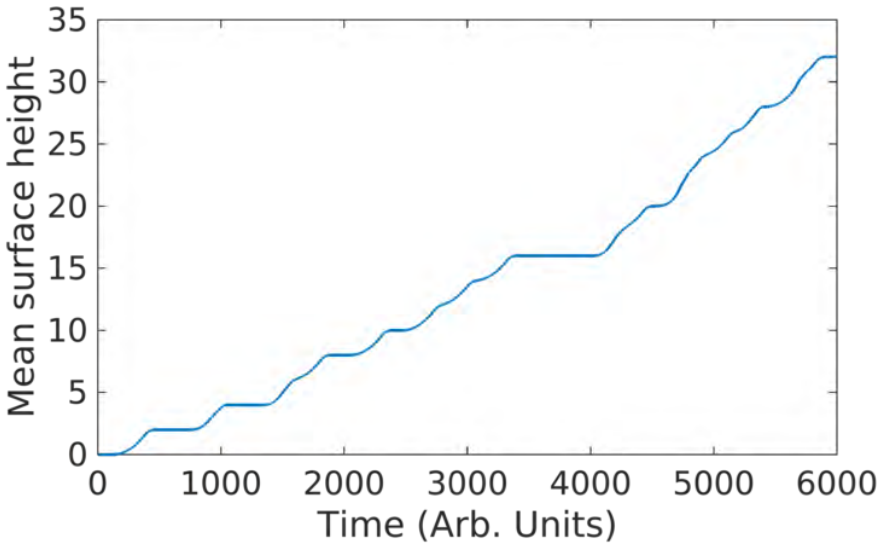

Figure 5.9. Mean surface height of the thin film graphed as a function of time for the case $\Delta\gamma_{AB} = 0.198 k_B T$. Even (odd) number of monolayers correspond to low (high) energy surfaces.

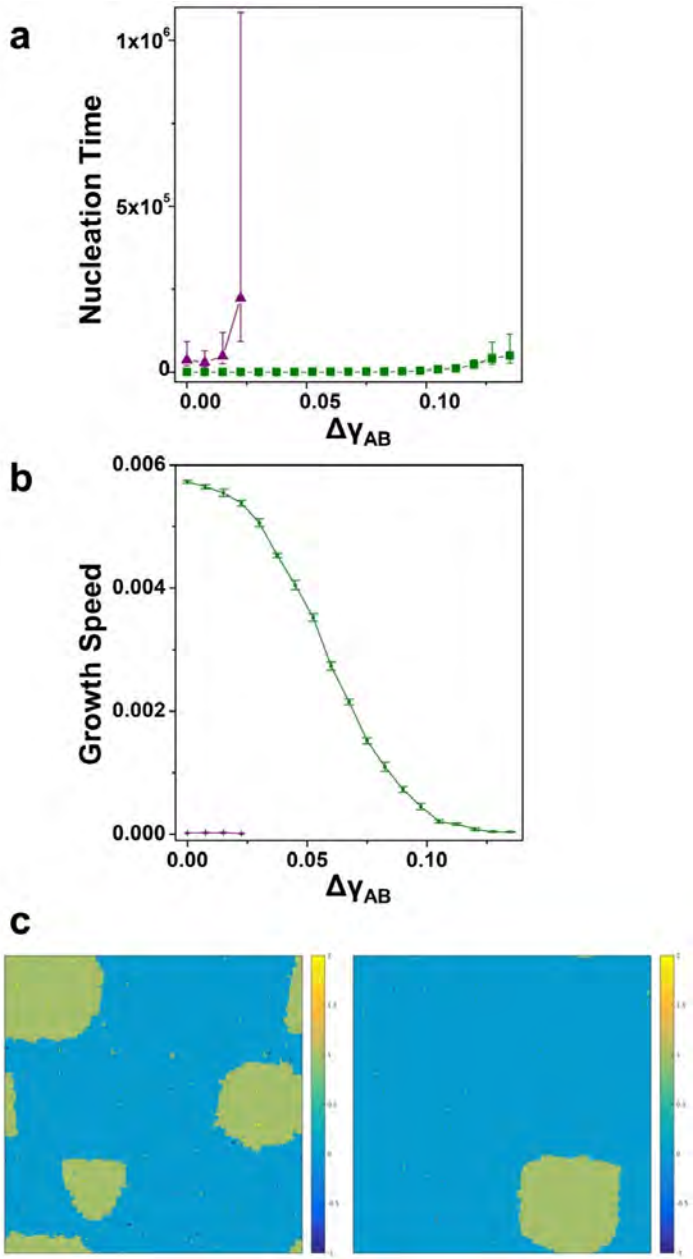

Figure 5.10. **a**, Mean time between sequential nucleation events. **b**, Mean surface growth velocity. For both **a** and **b**, green points represent $\gamma_e = 0.80 k_B T$ and purple points represent $\gamma_e = 0.95 k_B T$. **c**, Typical surface profile at $\Delta\gamma_{AB} = 0$ (left; $\gamma_e = 0.80 k_B T$ and right; $\gamma_e = 0.95 k_B T$).

CHAPTER 6

The Role of Salt and Repulsion in the Hybridization Kinetics of DNA-Functionalized Nanoparticles

Authors: Soyoung E. Seo*, Martin Girard*, Monica Olvera de la Cruz, Chad A. Mirkin

1. Abstract

Colloidal crystallization with programmable atom equivalents (PAEs) composed of DNA-modified spherical nanoparticles allows one to program in a sequence-specific manner crystal symmetry, lattice parameter, and, in certain cases, crystal habit. Despite the high level of structural control afforded by this approach, less is known about ways to control the size of the resulting microcrystals. Here, we explore the possibilities of using salt and the electrostatic properties of DNA as a polyelectrolyte brush to regulate the attachment kinetics between PAEs. Counterintuitively, simulations and theory show that at high salt concentrations (1 M NaCl), the hybridization kinetics increase by over an order of magnitude compared to low concentration (0.3 M), resulting in a transition from interface-limited to diffusion-limited crystal growth at larger crystal sizes. Remarkably, at elevated salt concentrations, well-formed rhombic dodecahedron-shaped microcrystals up to 21 μm in size grow, whereas at low salt concentration, the crystal size typically does not exceed 2 μm. Simulations show an increased barrier to hybridization between complementary PAEs at elevated salt concentrations, consistent with previous simulations linking long-range interactions to ionic clustering. These clusters are involved in compensating the charge of the PAEs, but they sterically impact hybridization. Therefore, although one might intuitively conclude that higher salt

concentration would lead to less electrostatic repulsion and faster PAE-to-PAE hybridization kinetics, the opposite is the case, especially at larger inter-PAE distances. This ion clustering effect becomes most pronounced at salt concentrations greater than 0.5 M. These observations provide an understanding of how solution ionic strength can be used to control the attachment kinetics of colloids coated with charged polymeric materials in general and DNA in particular.

2. Body

Colloidal crystals composed of nanoparticles are structures that can be designed to have interesting optical and electronic properties, based upon nanoparticle composition, crystal lattice symmetry and spacing, and mesoscopic crystal habit and size [**113, 19, 136, 137, 138**]. Because of their chemical programmability and sequence-specific interactions, oligonucleotides have emerged as versatile ligands to direct the assembly of nanoparticles into higher order crystalline architectures[**125, 85, 87, 5**]. Indeed, nanoparticles functionalized with a dense shell of upright and oriented DNA behave as "programmable atom equivalents" (PAEs) that can be assembled into a diverse set of crystalline structures following well-established design rules[**125, 85, 5, 3, 11, 86**].

The size of colloidal crystals is an important design parameter for the preparation of device architectures, particularly those requiring control over the optical path length (i.e., the distance that light travels across the crystal in the orientation of interest)[**113, 19, 139**]; however, methods for realizing single crystals with tunable sizes have yet to be developed using this approach. The size of three-dimensional single crystals generated by slow cooling is typically 2 μm or less[**3**]. Previously, molecular intercalators were introduced to post-synthetically modulate the strength of the DNA bonds within these crystals[**140, 123**], which were used as seeds for controlling the extended

growth of PAE crystal structures.15 While this approach provides a powerful way to generate core-shell crystals with variation in nanoparticle composition, it requires a stepwise, chemically-guided iterative growth process.

In atomic systems, large crystals can be realized by kinetically impeding the formation of critical nuclei. This can occur by either (i) suppressing the formation of new nuclei or (ii) expediting the growth of existing crystals to deplete the solution of the atom source (e.g., heterogeneous nucleation and growth)[**141**]. In the context of DNA-mediated nanoparticle crystallization, salt concentration can be used to control the kinetics of DNA bond formation[**142**]. At moderate monovalent salt concentrations (below 0.5 M), the kinetics of PAE reorganization in superlattices change as a function of solution ionic strength mainly because the additional charge screening stabilizes the DNA linkages between adjacent PAEs once formed[**143**]. However, at high salt concentrations (above 0.5 M), the kinetics of PAE interactions cannot be explained solely by charge screening. When monovalent ions are extremely crowded in aqueous solution, the association of ions becomes favorable via ionic correlations, resulting in the formation of ion clusters[**144, 145, 146**]. These ion clusters contain some water molecules and a large number of Na+ ions in the core, while most of the Cl- ions are pushed to the surface[**144**]. Full atom and coarse-grained simulations show that the fraction of clusters with 5 to 8 ions increase rapidly as the salt concentration increases from 0.3 to 1 M[**146**]. We hypothesize that these clusters electrostatically interact with the DNA corona surrounding the nanoparticle and incur a significant energetic penalty associated with charge repulsion when the PAEs are in close proximity, resulting in a reduction of the attachment kinetics during PAE crystallization.

To explore the free-energy landscape across which nucleation takes place with varying salt concentrations, molecular dynamics (MD) simulations were used to calculate PAE interaction potential energies (Fig. 6.1A). These simulations used a PAE design consisting of two 15-nm spherical gold

nanoparticles each functionalized with one of two DNA sequences bound to linker strands with complementary "sticky ends" (Fig. 6.1). These PAEs assemble into bcc superlattices. The foundation for these simulations is based on the assumptions that: (i) the interaction between the complementary PAEs is the main driving force for crystallization, (ii) the interaction with the second nearest neighbors (i.e., non-complementary PAEs) are negligible, and (iii) similar trends in the free energy are observed at room temperature (25C) and elevated temperatures. Effective pair potential energies were calculated by modeling two complementary PAEs at 25C with the 3SPN force-field, which included DNA-hybridization attraction, stacking interactions, excluded volume repulsion, and electrostatic interactions between phosphate groups and explicit ions[**15, 16**]. The strong parallels between the modeled and experimental results (DNA melting temperature increases with salt concentration) indicate that the binding energy between the PAEs increases with salt concentration (Fig. 6.1B).

The impact of salt concentration on the interaction potential between a pair of PAEs was studied by calculating the potential energies as a function of interparticle distance (i.e., core-to-core distance) ranging from 30 to 40 nm. Previous studies on nanoparticles with non-complementary DNA strands exhibit repulsion forces between nanoparticles that are longer range than the repulsion predicted by DLVO theory when the salt concentration increases above 0.3 M[**146**], which is in agreement with experiments on repulsion between charged surfaces at high monovalent salt concentrations[**147**]. For colloids grafted with strongly charged polymer chains (e.g., PAEs), the effective screening length was measured to be between 2 to 5 nm as opposed to the sub-nm length predicted by DLVO[**146**]. Consistently, above certain salt concentrations, simulations that include hybridization interactions show short-range attraction from hybridization interactions at distances where the DNA coronae overlap and longer range repulsion extending to distances where the DNA coronae do not overlap (Fig. 6.1B). This results in an energetic barrier greater than the thermal

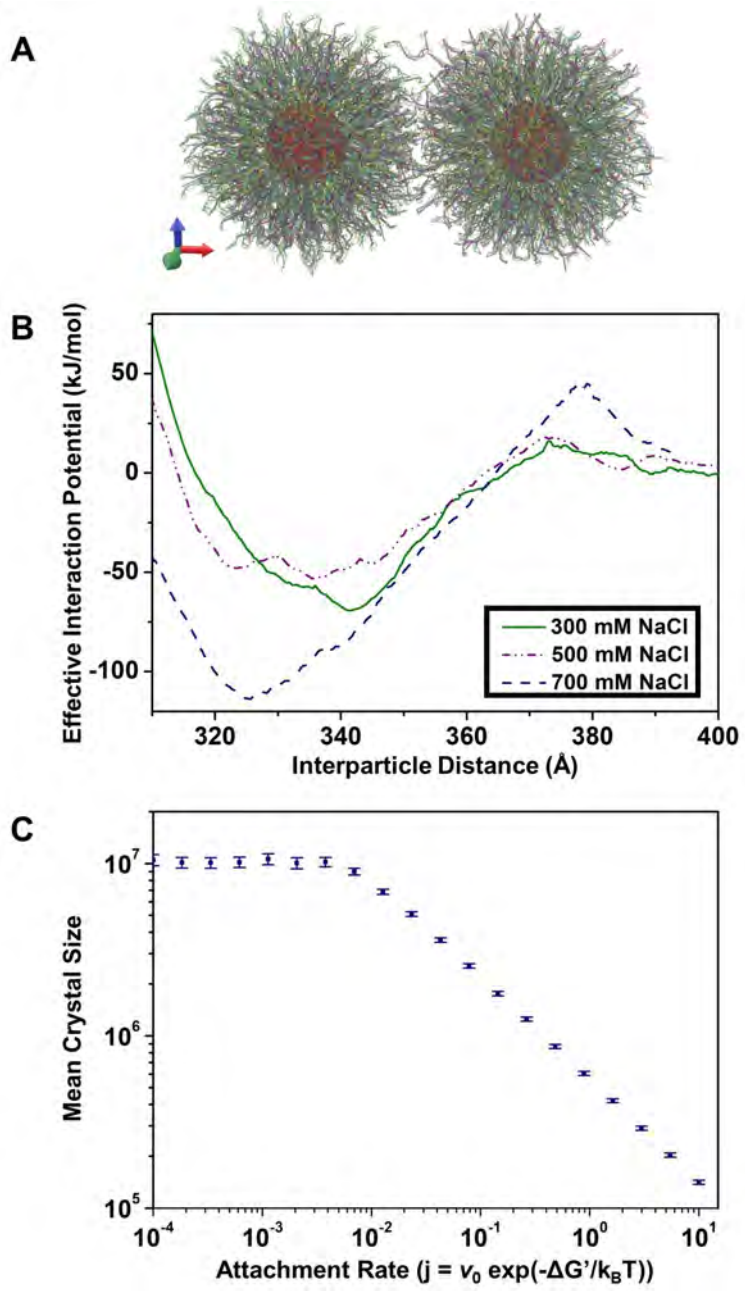

Figure 6.1. (**A**) A snapshot of two complementary PAEs at different salt concentrations in simulations. The centers of the 15-nm nanoparticles are 370 apart in this snapshot. (**B**) Pair potential energies between complementary PAEs were calculated across a range of interparticle distances. PAEs exhibit a well-defined equilibrium interparticle distance at potential minimum. At an interparticle distance of 380 Å, the attachment barrier peaks; this increases with increasing salt concentration. (**C**) Mean crystal size obtained without coarsening as a function of the attachment rate to the surface.

energy (k_BT) (i.e., the thermal fluctuation of the system must cross over the nucleation barrier to initiate crystallization), which slows the attachment kinetics between complementary PAEs. Thus, we hypothesize that the PAEs assemble to form larger crystals at higher solution ionic strengths due to this nucleation barrier (Fig. 6.1C, 6.5, 6.6).

To investigate whether PAE assembly at elevated salt concentrations leads to the growth of larger microcrystals, two sets of 15-nm spherical PAEs with complementary DNA sequences were prepared. Each sample was assembled in solution at three different salt concentrations (0.3, 0.5, and 1 M NaCl) and then slow cooled. This process enables DNA-driven crystallization that favors the formation of single crystalline rhombic dodecahedra with the gold nanoparticles in a bcc crystallographic symmetry (over a polycrystalline assembly)[**5, 3**]. Single crystals were chosen as the subject of this study because crystal domain size is easier to identify and quantify. Superlattices were then characterized by small-angle X-ray scattering (SAXS), electron microscopy (EM), and selected area diffraction (SAD).

First, SAXS lineshape analysis was used to deconvolute peak broadening arising from grain size and microstrain, and the grain sizes were compared using a Williamson-Hall analysis (Figs. 6.2A). Stokes-Wilson strain broadening can be combined with Scherrer size broadening in scattering peaks to extract information about grain size (Eq. S12-13)[**148**]. Consistent with both the hypotheses and the calculations of interaction potentials, a significant increase in average grain size is observed when the salt concentration was increased from 0.5 to 1 M (Fig. 6.2A). Although the grain size generally increases with increasing salt concentration, it decreases with increasing particle concentration. A decrease in mean crystal size with increasing particle concentration can be attributed to the increase in chemical potential (Eq. S2). Since the nucleation rate is strongly dependent on the chemical potential of the system, increasing the chemical potential leads to a faster nucleation rate (i.e., a greater number of nuclei forms) and thus, the formation of smaller

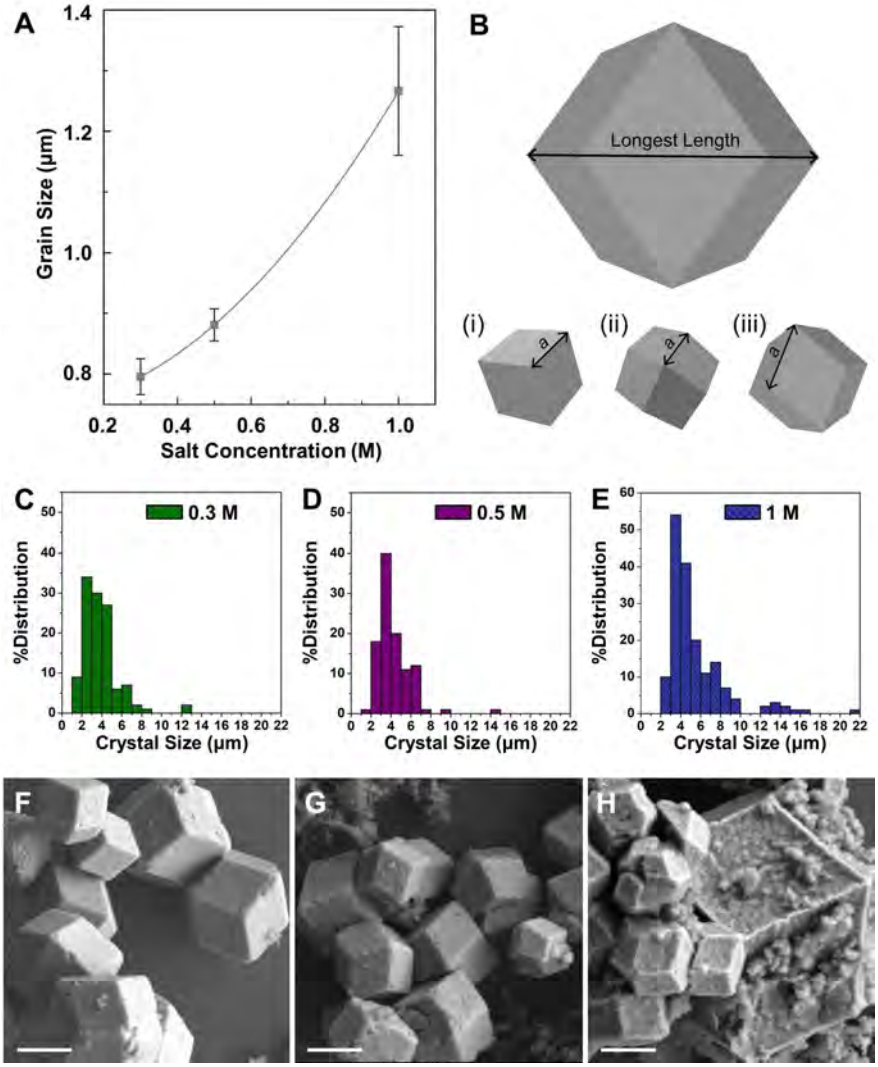

Figure 6.2. (**A**) Williamson-Hall analysis of SAXS data can be used to deconvolute peak broadening arising from grain size (intercept) and microstrain (slope). (**B**) Scheme (top) showing the dimension that was measured for the statistical analysis of crystal size distribution using SEM images. (i), (ii), and (iii) are schematic representations of three different orientations of the microcrystals commonly observed on the substrate. The length a (edge length) was measured and mathematically converted to convey the length shown in the top drawing. Size analyses of approximately 150 microcrystals, assembled at (**C**) 0.3, (**D**) 0.5, and (**E**) 1 M NaCl, show an increase in average crystal size with increasing salt concentration. SEM images of silica-encapsulated bcc gold nanoparticle microcrystals, interlinked with DNA and assembled at (**F**) 0.3, (**G**) 0.5, and (**H**) 1 M NaCl confirm faceted rhombic dodecahedra. Scale bars are 2 μm. Courtesy of Eileen Soyoung Seo

microcrystals is expected. Note that the chemical potential difference is a thermodynamic driving force for crystallization.

To further examine the effect of salt on crystal size along with crystal habit (e.g., facet), we used SEM to determine the size distribution of approximately 150 microcrystals for each salt concentration. Since the formation of microcrystals mediated by the slow cooling approach is similar to conventional homogeneous nucleation (i.e., the crystallization starts from dispersed precursors), a broad range of crystal sizes is expected. To prepare samples for SEM imaging, slow-cooled samples were encapsulated in silica using a sol-gel process[**134**], dispersed in 50% EtOH in water, and slowly dried on a silicon substrate. Remarkably, microcrystals generated in solution of different salt concentrations are all consistent with the rhombic dodecahedron crystal habit (Fig. 6.2F-H), and the overall crystal size increases with increasing salt concentration (Fig. 6.2C-E). Because the microcrystals dried on a substrate lie in different orientations on the substrate, mathematical corrections on each measurement of a (edge length) were performed (Fig. 6.2B). SEM results show similar size distributions for the 0.3 and 0.5 M salt concentration samples with mean sizes of 3.6 ± 1.6 and 3.5 ± 1.3 μm, respectively (Fig. 6.2D, E). However, similar to the conclusions drawn based on the SAXS data, a noticeable increase in the crystal size distribution is observed for the 1 M NaCl sample with a calculated mean size of 4.9 ± 2.6 μm (Fig. 6.2F). Remarkably, these crystals can grow up to 21 μm (the length shown in Fig. 6.2B, top) when the PAEs are assembled in high solution ionic strength (Fig. 6.2H).

The crystallization process is usually described by the formation of critical nuclei (i.e., nucleation) followed by subsequent growth. Generally, the nucleation rate is dependent on both the energy barrier of nanoparticle cluster formation and the attachment rate of the interacting nanoparticles. An emergence of long-range repulsion at high salt concentration, as shown in Fig. 6.1B,

results in a reduction of the attachment rate A, which can be understood from the following relationship:

$$j = \nu_0 \exp(-\Delta G'/k_B T)$$

where j is the frequency at which two nanoparticles come together, ν_0 is the trial rate (constant, units in 1/time), and $\Delta G'$ is the repulsion barrier that nanoparticles must overcome to initiate crystallization (see Simulation section in the SI for detailed discussion). Thus, from this equation, one can extract that the frequency of nanoparticle attachment events decreases exponentially with increasing energy barrier. In the case where the long-range diffusion is required, two rate-limiting processes, interface- and diffusion-limited, affect the growth rate. The initial stage of crystal growth is limited by interfacial attachment barriers. In this regime, crystal size increases linearly with time (crystal size $\sim At$, where A is the growth rate proportional to j and t is the time)[**149**]. In the case where the nanoparticle attachment occurs extremely fast (i.e., nanoparticle interactions are extremely favorable), no interface-limited regime is present, and this results in crystals with irregular shapes and disordered nanoparticles[**131**]. However, in our case, j is very small and we observe faceted microcrystals. When most of the nanoparticles are consumed, diffusion can no longer sufficiently transport materials to the crystal-solution interface. Beyond this regime, crystal growth is limited by diffusion, where the growth rate is significantly slowed (crystal size $\sim t^{1/2}$)[**108**]. The growth rate in this regime is entirely determined by the diffusion constant and the supersaturation, given by $c - c_{eq}$, where c and c_{eq} are current and equilibrium concentrations of the free nanoparticles in solution, respectively. The transition between the interface-limited to diffusion-limited regimes has been reported for colloidal crystals using MD simulations[**150**].

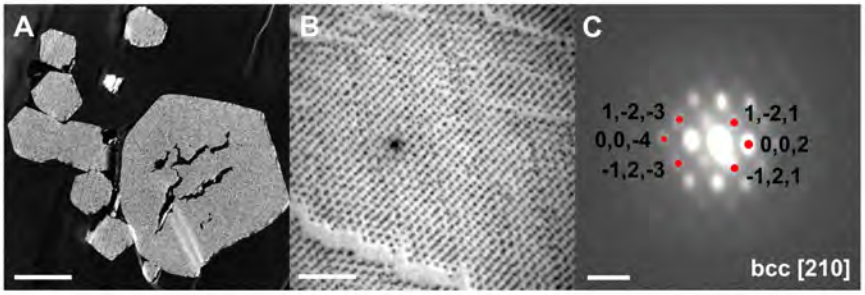

Figure 6.3. (**A**) and (**B**) Transmission electron microscopy (TEM) images of a thin ($\sim$100 nm) section of silica-encapsulated microcrystals, initially crystallized in 1 M NaCl. (**C**) Well-defined SAD patterns were obtained by subjecting a parallel beam of high-energy electrons to a thin section of one of the large microcrystals shown in (**B**). Scale bars are 5 μm, 200 nm, and 100 μm^{-1} for (**A**), (**B**), and (**C**), respectively. Courtesy of Eileen Soyoung Seo

The combination of MD simulations and experiments suggests that the reduction in the PAE attachment rate at 1 M NaCl likely impedes the formation of stable clusters/critical nuclei and drastically slows the interface-limited regime, meaning the system at high salt conditions enters the diffusion-limited regime much later than the other two systems. Thus, by suppressing the nuclei formation, large single crystals are realized. We presume that a similar trend will be observed when the rate of cooling is changed. It is worth noting that there is a possibility of large crystal growth occurring through coalescence and restructuring processes, where two or more stable crystals merge to form a single crystal. In atomic systems, coarsening typically occurs by Ostwald-like ripening processes; however, this process is very slow and unlikely to be observed in colloidal systems. On the other hand, it has been shown that the coarsening in colloidal systems could happen by grain-rotation induced coalescence[**151**]. Similar coarsening has been observed for PAE systems in MD simulations (see Simulation section in the SI for further discussion)[**150**].

Because defects and inhomogeneity in the superlattice can affect the optical response of these materials, it is crucial to produce high-quality crystals[**152**]. Each SAXS pattern shows, regardless of the solution ionic strength, a high degree of single-crystalline ordering of nanoparticles arranged

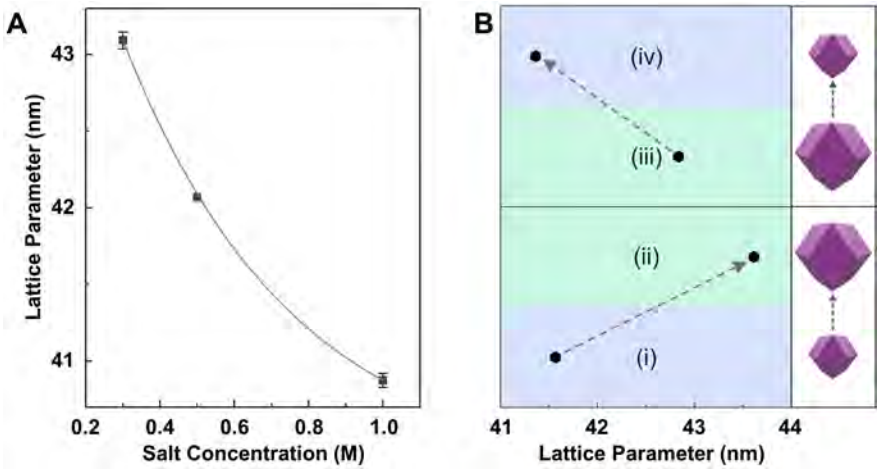

Figure 6.4. (**A**) The bcc unit cell lattice parameter at different salt concentrations. (**B**) The change in lattice parameters induced by salt is reversible. Courtesy of Eileen Soyoung Seo

into a bcc crystallographic symmetry. The crystallinity was further characterized by performing SAD using a transmission electron microscope (TEM) (Fig. 6.3). This characterization technique provides a diffraction pattern of a thin crystalline specimen within a selected area, which can be used to identify local crystal structures and examine defects, such as twinning and dislocations. Here, we used SAD to qualitatively evaluate the crystallinity of local areas within these microcrystals. Indeed, the appearance of distinct spots in the diffraction patterns of a large single crystals indicates high-quality crystals and that the microstrain is mostly isotropic without random defects (Fig. 6.3C).

Furthermore, it is important to have independent control over the interparticle distance, while retaining crystallinity and habit, because each structural control can be used to dictate the material properties. A uniform shift in peak position, however, indicates that there is a 5% decrease in the DNA bond length as the salt concentration is raised from 0.3 to 1 M (Fig. 6.4A). However, since the interactions between the DNA bonds and ions are electrostatic in nature, the lattice parameters of these superlattices can be altered simply by salt exchange (Fig. 6.4B). By changing the salt concentration after the crystals are grown, the salt-induced transition in interparticle spacing is

fully reversible and SAXS patterns collected before and after salt exchange do not show noticeable changes in the SAXS peak widths (Fig. 6.4). A uniform shift in peak position, however, indicates that there is a 5% decrease in the DNA bond length as the salt concentration is raised from 0.3 to 1 M (Fig. 6.4A). However, since the interactions between the DNA bonds and ions are electrostatic in nature, the lattice parameters of these superlattices can be altered simply by salt exchange (Fig. 6.4B).

Taken together, the conclusions presented here reveal the properties of polyelectrolyte brushes of nanoparticle-based DNA bonds and provide a powerful approach to alter the attachment kinetics of PAEs to control mesoscale crystal size. Importantly, PAE crystallization at elevated salt concentrations can be used to synthesize colloidal single crystals over a significantly larger length scale. Furthermore, through post-synthetic salt exchange process, the salt-induced transition is fully reversible. The extension of this work to different annealing conditions, multivalent cations, and DNA loading should enhance our fundamental understanding of tuning kinetics to control materials properties and lead to new possibilities for the realization of kinetically-controlled superlattice structures. The high-level of structural control over colloidal single crystals will enable researchers to probe the effect of crystal size on the optoelectronic and mechanical properties of these materials.

3. Associated content

Supporting Information. Experimental procedures, including simulation details, oligonucleotide sequences, nanoparticle functionalization and assembly, and characterization/analysis techniques (SAXS, SEM, and TEM), and additional figures are available in the SI.

4. Acknowledgements

We thank Dr. Andrew J. Senesi for his helpful discussion on SAXS data analysis. This work was supported by the following awards: the Center for Bio-Inspired Energy Science, an Energy Frontier Research Center funded by the U.S. Department of Energy, Office of Science, Basic Energy Sciences Award DE-SC0000989 (oligonucleotide syntheses and purification, simulations); the Air Force Office of Scientific Research Award FA9550-17-1-0348 (DNA-functionalization of gold nanoparticles); and the National Science Foundation's Materials Research Science and Engineering Center program (DMR-1121262) and made use of its Shared Facilities at the Materials Research Center of Northwestern University (EM characterization). SAXS experiments were carried out at beamline 5-ID of the DuPont-Northwestern-Dow Collaborative Access Team at the Advanced Photon Source. Use of the Advanced Photon Source at Argonne National laboratory was supported by the U.S. Department of Energy, Office of Science, Office of Basic Energy Sciences, under Contract No. DE-AC02-06CH11357 (SAXS characterization). S.E.S. acknowledges partial support from the Center for Computation and Theory of Soft Materials Fellowship.

5. Supplementary information

5.1. Molecular dynamics simulations

Effective pair potentials, including electrostatic repulsion and short-range attraction between the colloids, were calculated via molecular dynamics (MD) simulations to study the crystallization of charged colloids. In previous studies, colloidal models were extended to predict the shape of grains of DNA-coated nanoparticle crystals[**3**]. Here, MD simulations were carried out to understand the change in interaction between nanoparticles as the salt concentration is increased above the regime where the Debye-Hückel theory is valid. The DNA model that we used previously[**14**] is not

detailed enough to provide attachment barriers, which is critical in nucleation theory. For this reason, we implemented the 3SPN model from the de Pablo group with point ions[**15, 16**] in the HOOMD-blue molecular dynamics engine[**99, 100**].

5.1.1. Calculating Potential of Mean Force for DNA-Coated Nanoparticles. Initial configurations were generated using HOOBAS [**33**], which uses X3DNA software [**153**]. The simulation size is set to $dx = dy = 60$ nm for the $x-$ and $y-$dimensions and $dz = 120$ nm for the $z-$dimension. Simulations were carried out in the canonical ensemble using Langevin dynamics with a drag coefficient γ of the ith particle which was set to $\gamma_i = \sigma_i/2$ (σ_i is the diameter of the ith particle). These coefficients were chosen to be smaller than the value expected from the Stokes law and water dynamical viscosity for numerical equilibration times. With this setup, simulations contain up to 3.85×10^5 ions. Nanoparticles were constrained to move along the z direction only. An additional spring was added between the two nanoparticles with potential energy $U_{bias} = K_{bias}(z - z_0)^2$, with $K_{bias} = 0.25$ kJ/mol/Å^2. Each simulation ran at a given value of z_0 which represents one window for umbrella sampling. Each window was sampled for 5×10^6 timesteps of $\Delta t = 0.07\delta t$, where δt is the time unit, which is approximately equal to 10^{-13} s. Windows were separated by at most 3 Å. In the barrier region around 380 Å, the potential of mean force was sampled more finely with distances between windows around 1 Å. The final potential is reconstructed by Multistate Benett Acceptance Ratio (MBAR) method in the molecular analysis package from the Computational Biophysics Research Team at RIKEN (http://www.riken.jp/TMS2012/cbp/en/research/software/index.html, package available online: https://github.com/ymatsunaga/mdtoolbox).

An additional biasing potential was added between complementary bases of the linker DNA strand attached to different nanoparticles. This biasing takes the form of a Morse potential:

$$U_{morse} = D_e \left(1 - \exp(-\alpha(r - r_0))\right)^2 - D_e \tag{6.1}$$

with $\alpha = 0.33$ Å^{-1}, $D_e = B2.65$ kJ/mol for G-C pair, and $D_e = B4.18$ kJ/mol for the A-T pair. The quantity B is the amount of biasing introduced in the simulation. We used Hamiltonian replica exchange to exchange configurations between 4 different replicas that have $B = 0$, 0.5, 1 and 1.5 to overcome the long diffusion times between two complementary sticky ends finding each other. The system was equilibrated for 3×10^4 timesteps after each swap. The data for the potential of mean force was gathered over 5×10^4 timesteps before another swap attempt was made. Swapping probabilities vary from 30% for close separations up to 100% for large separations as the biasing force only acts between complementary linker strands.

5.2. Crystal growth

The number of crystals growing at any point, k, increases at a rate given by:

$$\frac{dk}{dt} = j \exp(\frac{-16\pi\gamma^3}{3\Delta\mu^2}) \tag{6.2}$$

where γ is the surface energy, $\Delta\mu$ is the chemical potential given by $\Delta\mu = \Delta\mu_0 + log(c/c_0)$, where c is the current concentration and $\Delta\mu_0$ is the drive at concentration c_0. We assumed the Zeldovitch factor to be 1. Two different rates of crystal growth can be derived. In interface-limited regimes, the rate of growth of the number of atoms of the ith crystal is given by:

$$\frac{dn_i}{dt} = j\Delta\mu n_i^{2/3}\tau \tag{6.3}$$

where τ is a proportionality constant and n_i is the number of atoms in the ith crystal. In diffusion-limited regimes, the growth rate is given by:

$$\frac{dn_i}{dt} = 3V_m\Omega D n_i^{1/3} \tag{6.4}$$

where Ω is the supersaturation given by $\Omega = (c - c_{eq})$ for spherical particles, c_{eq} is the equilibrium concentration, V_m is the molar volume, and D is the diffusion constant. For small values of n_i, the growth is interface-limited while for the large values of n_i, the growth is diffusion-limited. While one would generally assume a mixture of rates when the growth is neither limited by diffusion or interface, in this study, we assumed that the growth rate is at its minimum of the diffusion or interface-limited rates. The evolution of concentration of the solution is given by:

$$\frac{dc}{dt} = -\sum_i^k \frac{dn_i}{dt}\frac{1}{V} \tag{6.5}$$

where V is the total volume. Since numerical integration requires the number of dimensions of the differential equations to be an integer, we used stochastic integration for Eq. 6.2. During a timestep, the chance of increasing the number of dimensions by one (forming a new nuclei) is given by:

$$P(k+1) = \Delta t \times j \exp(\frac{-16\pi\gamma^3}{3\Delta\mu^2}) \tag{6.6}$$

where $\Delta t = 0.001$ is the size of a time step. This implicitly discards any chances of having two or more nucleation events occurring in the same timestep. In the case a nuclei forms, we assumed that it is of a critical size, $n_c = (2\gamma/\Delta\mu)^3$. The number of atoms in the ith nuclei was integrated using the following equation:

$$\frac{dn_i}{dt} = \min\left(j\Delta\mu n_i^{2/3}\tau, 3V_m\Omega D n_i^{1/3}\right) \tag{6.7}$$

This assumes that the growth rate is at its minimum between the interface-limited and diffusion-limited regimes. Usually an additional contribution is added to $\Delta\mu$ from the surface tension which results in Ostwald ripening. We ignored this contribution in our calculations for two reasons. First, this process is extremely slow and is not seen in timescales at which crystallization occurs in molecular dynamics[**150, 154**]. Second, Ostwald ripening results in a distribution with a negative skew, which is inconsistent with experimental results. Therefore, for numerical simulations, we used $\tau = 3$, $V_m D = 0.05$, $V = 10^8$, $c_0 = 1$, $\Delta\mu_0 = 2$, and $\gamma = 2$. Changes in these values results in different quantitative but similar qualitative behavior.

5.2.1. Coalescence. In previous work on DNA-mediated assemblies, it has been shown that crystals assembled with PAEs can grow by coalescence[**150**]. We included coalescence in our simulations by assuming that the probability of the ith and jth crystals coalescencing during a timestep is: $P(coal) = \Delta t k_{coal}(D_i + D_j)$, where k_{coal} is a rate of coalescence and D_i is the diffusion constant of crystal i, which we assumed to follow Stokes equation $D_i = 1/n_i^{1/3}$. When two crystals

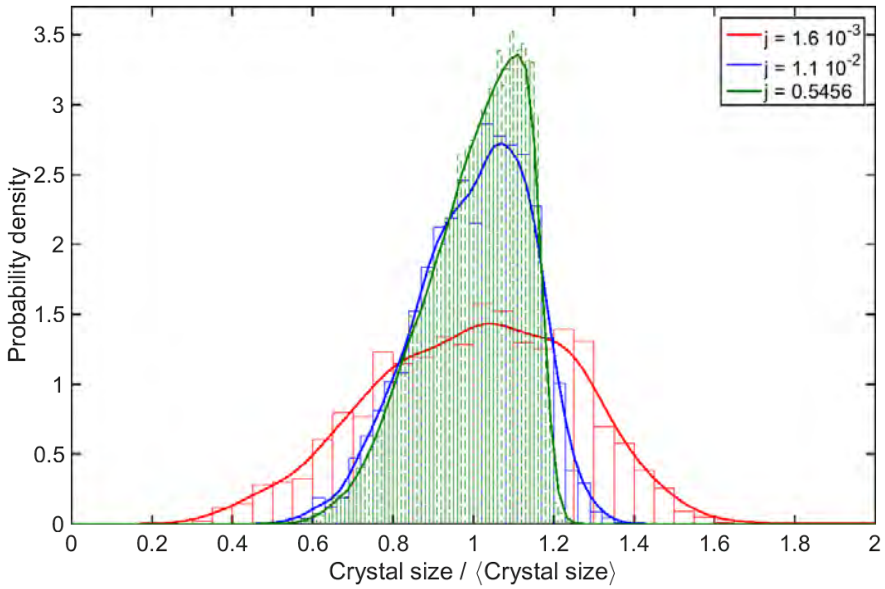

Figure 6.5. The distribution of normalized crystal size for attachment rates of 0.0016, 0.011 and 0.55. Evolution towards a narrow negative-skew distribution for increasing attachment rates is clearly seen. Histogram is obtained from raw data while curves are estimated from the kernel density estimation.

coalesce, we assumed that they instantly equilibrate to a spherical shape with $n_i = (n_i + n_j)$ and $n_j = 0$. While not entirely physical, it produces reasonable results provided k_{coal} is low and the surface diffusion of the PAE is sufficiently large.

5.2.2. Size distributions. The distribution of crystal size is an interesting quantity to compare simulations to experiments. The distributions generated with $k_{coal} = 0$ provide crystal size distributions with mostly negative skew (Fig. 6.5). For crystals via nearly fully interface-limited growth, the skew is small. However, crystals grown mostly in the diffusion-limited regimes show highly negative skew. For instance, using an attachment rate of 0.0016, we find a skew of -0.16, while an attachment rate of 0.54 shows a skew of -0.67. Neither of these distribution match the positive skew, doubly-peaked experimental distributions shown in Fig. 6.2C-E.

None of these distributions characterize the experimental results which is a doubly peaked distribution. Setting a non-zero value to kcoal produces interesting results. For sufficiently low values

of kcoal, we observe an initial growth phase followed by a coarsening phase (Fig. 6.6). During coarsening, the distribution exhibits two maximums akin to what is observed in experiments. Furthermore, the skewness initially drops during growth, but grows during coarsening, eventually settling at a value slightly above 1.5, even for systems with high attachment rates.

This would suggest that some coarsening of crystals happen in our experiments. However, the coarsening process is typically very slow. Moreover, TEM images show quenched, coalesced crystals, which were ignored in our statistics. This is in agreement with prediction from previous simulations[**150**], which were calculated at finite undercooling. It is unknown whether the observed quenched states on TEM images are created during coalescence events during the crystallization process at elevated temperatures or afterwards. Furthermore, the elevated melting temperatures at higher ionic strengths could promote higher diffusion on crystal surfaces and favor relaxation of coalesced crystals.

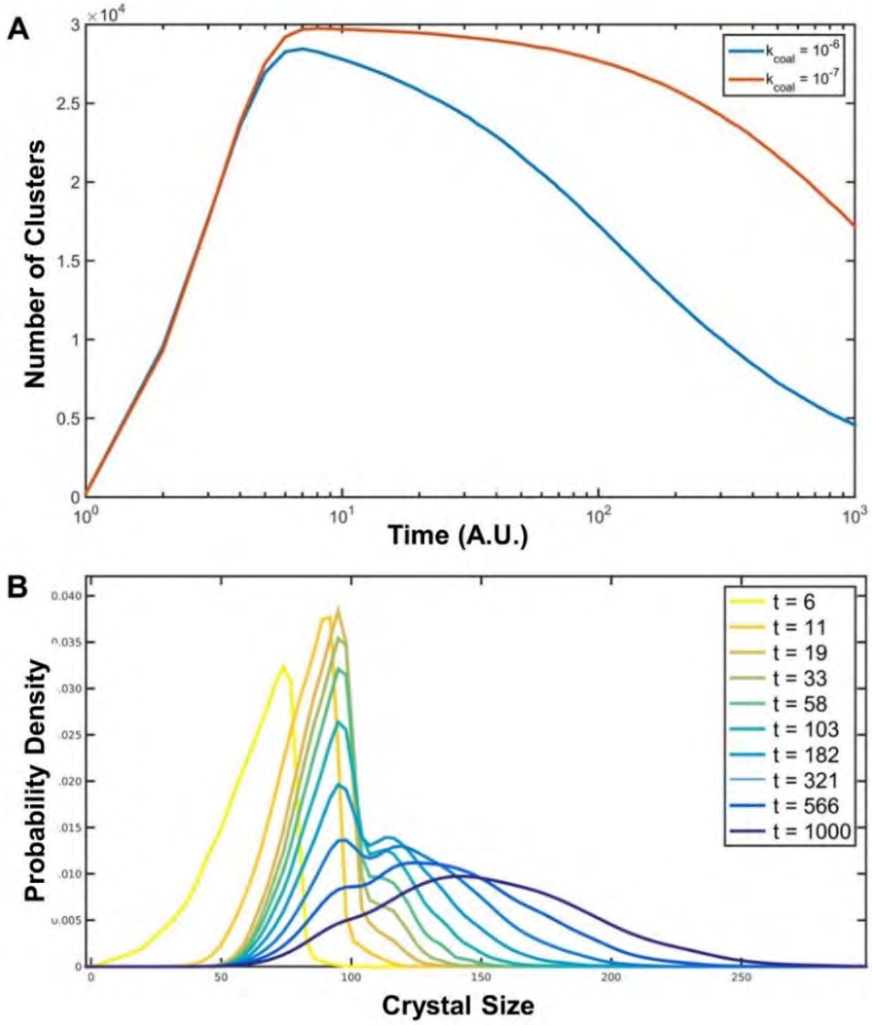

Figure 6.6. (**A**) The number of crystals as a function of time for two values of k_{coal}, clearly showing the initial growth and subsequent coarsening. (**B**) The distribution of crystal sizes during the coarsening with $k_{coal} = 10^{-6}$ for different times. The curve shows a second peak for intermediate times. Attachment rate is set to 0.5456.

CHAPTER 7

Electron - atom duality of nanoparticles in DNA-guided assembly

Authors: Martin Girard, Monica Olvera de la Cruz

Collaborative work with: Anindita Das, Shunxi Wang, Chad A. Mirkin

This is part of a collaborative work that is still going on and where experiments are trying to measure simulation predictions.

1. Abstract

Surface functionalization of colloids has led to crystalline compounds with various symmetries and functions. In particular, DNA-guided assemblies based on spherical colloids grafted with complementary DNA have yielded phases that can be directly compared to atom equivalents. Here we show that in mixtures of large and small DNA functionalized nanoparticles, the smaller particles when grafted with few DNA strands roam the crystal acting as classical electrons in metals, with an adjustable metal valency. As the number of strands on the smaller particles is increased or temperature is decreased, the smaller particles localize yielding a phase transition from metal to compounds, including intermetallics. The metallic nature of these crystals thus has new design rules that add degree of freedoms based on metal valency.

2. Body

DNA-mediated assembly has emerged as a powerful tool in colloid science to obtain crystal lattices with controllable symmetries, lattice parameters and crystal habits [**3, 5, 128**]. In this paradigm, colloids grafted with DNA become equivalent of atoms in regular crystal and are called

particle atom equivalent (PAE). The original design rules obtained by MacFarlane based on DNA and particle size ratios for binary systems of spheres predict only a handful of phases[**5**]. Other approaches also include anisotropic DNA coverage of proteins [**155**], usage of like-charge attractions by ionic correlations [**156**] and incorporating DNA scaffold structures[**157**].

In all of these approaches, crystals formed are always of ionic nature where the stoichiometric ratio between different particles is fixed and their position in the lattice well defined. One can interpret the DNA linkers of the PAE as equivalent to the atomic orbitals of atoms, where bonding between atoms occurs in regions of DNA overlap. In this picture of atomic systems, electrons are confined the neighboring regions of atoms and cannot form extended states in the crystal due to their lack of wave properties. In contrast to ionic compounds, metallic crystals allow for formation of complex alloys, with the well-known example of the Ho-Mg-Zn quasicrystal which led to the 2011 physics Nobel prize [**158**]. In classical metals, ions are interacting with a sea of electrons. In order to replicate this behavior in PAE systems, one needs to have highly mobile PAEs. The DNA bonds in PAE systems is dynamical and the fraction of linkers bound at any given time is relatively low [**159**]. Due to the large number of linkers per particle (> 30), the number of DNA bonds per particle do not differ much from the average. We hypothesize that for colloids grafted with very few DNA strands (< 10), individual particles can have their DNA linkers unbound and diffuse in the crystal, behaving like classical electrons in metals.

Here, we use a model system consisting of DNA-functionalized nanoparticles varying drastically in size and DNA surface density to test our hypothesis. In this scheme, commercially available AuNPs (10 nm-20 nm diameter) were densely functionalized with propylthiolated DNA to yield conjugates modified with 190 strands (ssDNA). To achieve maximum particle size difference and DNA loading densities, ultra-small gold nanoparticles ($\leq$ 2 nm diameter), henceforth referred to as gold nanoclusters (AuNCs), were chosen as the second particle core. In particular, a

structurally well-characterized Au_{102} nanocluster was functionalized with 8 DNA strands. Complementary DNA "linkers" were then hybridized to the surface-bound DNA of each particle, yielding PAEs bearing a rigid, double-stranded DNA (dsDNA) region and an exposed, non-self complementary 5' overhang "sticky end" to drive PAE assembly. Combining complementary AuNPs with significantly higher amounts of AuNC conjugates (≥ 5 times) in 0.5 M NaCl solution led to formation of aggregates.

Previous experiments with similar but larger particles predict AB_2 or AB_6 (Cs_6C_{60}) phases [**5**]. In the AB_2 phases, the large A particle occupy positions of a hexagonal lattice, while the smaller B PAE occupy the 2d Wyckoff positions. In the AB_6 crystal, the large A PAE occupy positions of a BCC lattice and the smaller B PAE occupy the 12d Wyckoff positions. SAXS measurements reveal that the position of the larger PAE can take the positions of either BCC, Frank-Kasper (FK) A15 or FCC crystal lattices (Fig. 7.1C). Further characterization by means of transmission electron microscopy reveal that the smaller particles are disordered in the lattice of large particles. This suggests that the smaller particles are in a phase akin to a liquid, freely moving between crystal cells. The smaller PAEs are behaving as electron in classical metals with a valency prescribed by the incorporated small PAEs in the lattice.

Unlike previous ionic-like crystals, the stoichiometric ratio between large and small particles is continuously tunable. Indeed, crystal grown using a ratio of 8:1 yields large A particles still occupying BCC positions even if there are only six crystal sites available, without any measurable nascent phase left. As valency is raised to 10, competition between the BCC and FCC lattices is seen on SAXS patterns, with only FCC measured at higher valencies (see Fig. 7.1D-F). A15 phase is obtained when the number of ssDNA on AuNC is ≥ 10. The average number of linkers on the Au_{102} NC is 6.

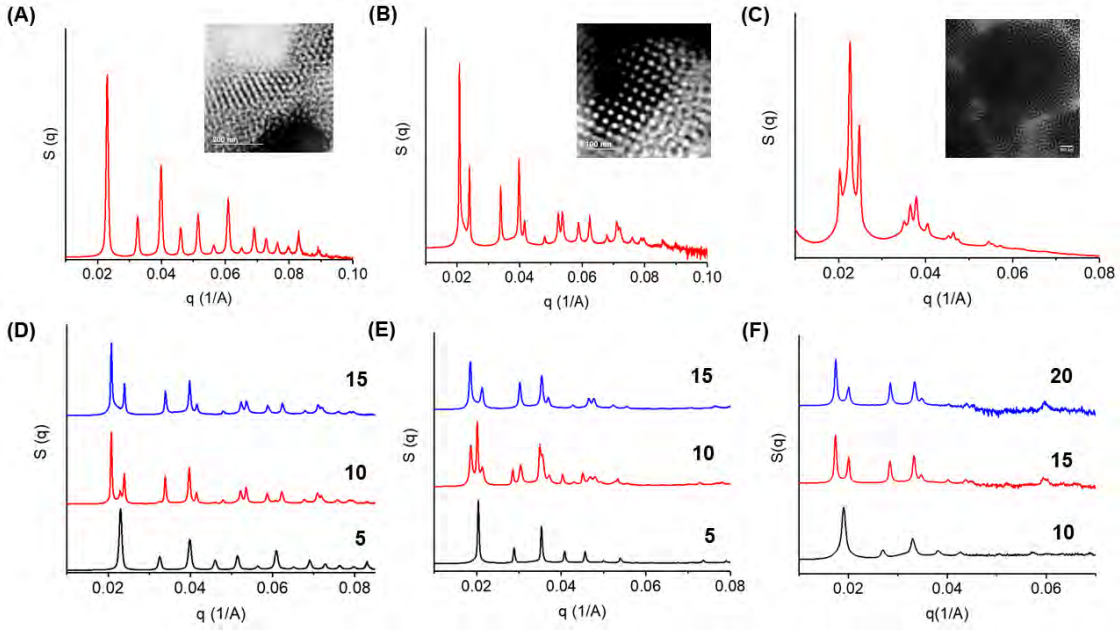

Figure 7.1. SAXS patterns and TEM of (**A**) BCC (**B**) FCC and (**C**) A15 lattices composed of DNA conjugated AuNPs (10 nm diameter) and AuNCs. BCC to FCC transition with increasing valency in (**D**) 10 nm- and (**E**) 15 nm- and (**F**) 20nm AuNP-AuNC systems. Courtesy of Anindita Das

In simulations, the A15 phase doesn't possess a trivial geometrical relation with either BCC or FCC and are always stable at $k_BT = 1.30$. Elevating temperatures to compare relative stability reveals that melting temperatures of both phases are very close. For systems with a low number of duplexed strands on the small B particles BCC phase is more stable than A15. For a large number of duplexed strands, the A15 is more stable, suggesting that there is a relation between observed phases and the overall number of linkers on the small particles, an effect not observed in previously established design rules.

We carried molecular dynamics simulations using previously established coarse-grained model [**14, 13**] to verify stability of the crystal phases. Just as in experiments, BCC, FK A15 and FCC phases can be stabilized by tuning the stoichiometric ratio between A and B particles (Fig. 1E). A weak dependence on the number of duplexed strands on the smaller B particles is also observed.

By discretizing space and counting the visitation frequency of the smaller particles, f_k, the value for the degree of delocalization of the colloids, which we termed the metallicity can be computed. We treat f_k as a probability function and use the information entropy (Shannon entropy) given by

$$S = -\sum_k f_k \log(f_k)$$

The entropy is minimized if all colloids are localized and maximized for a uniform distribution. We then define metallicity as available volume per B particle using:

$$M = S + \log(V_{cell}/N_B)$$

Where V_{cell} is the volume of a unit cell and N_B the number of B particles per unit cell. For a classical metal electron with a uniform distribution in space, Shannon entropy is maximized, while localization into specific regions is minimized. PAE design allows for control of the metallicity (Fig. 7.2A and B). Increasing the number of duplexed strands on the small PAE tends to form a more ionic crystal, confirming the initial hypothesis that delocalization is based on probability of unbinding PAEs. Furthermore, delocalization increases with temperature as the number of sticky ends hybridized falls. The metallicity can be controlled by changing the valency (i.e., the stoichiometry). Increasing the number of small particles results in a more ionic crystal until a certain stoichiometric ratio is attained and then falls.

In order to demonstrate the duality in the bonding from metallic to compound decreasing temperature, we draw an analogy with the nearly free electron models, where the band structure is comprised of a valence and a conduction band separated in energy by a bandgap which is proportional to the atom electron interaction. From this picture, by increasing valency we "fill" the valency states, which decreases conductivity until the valency band is completely filled. Further increasing

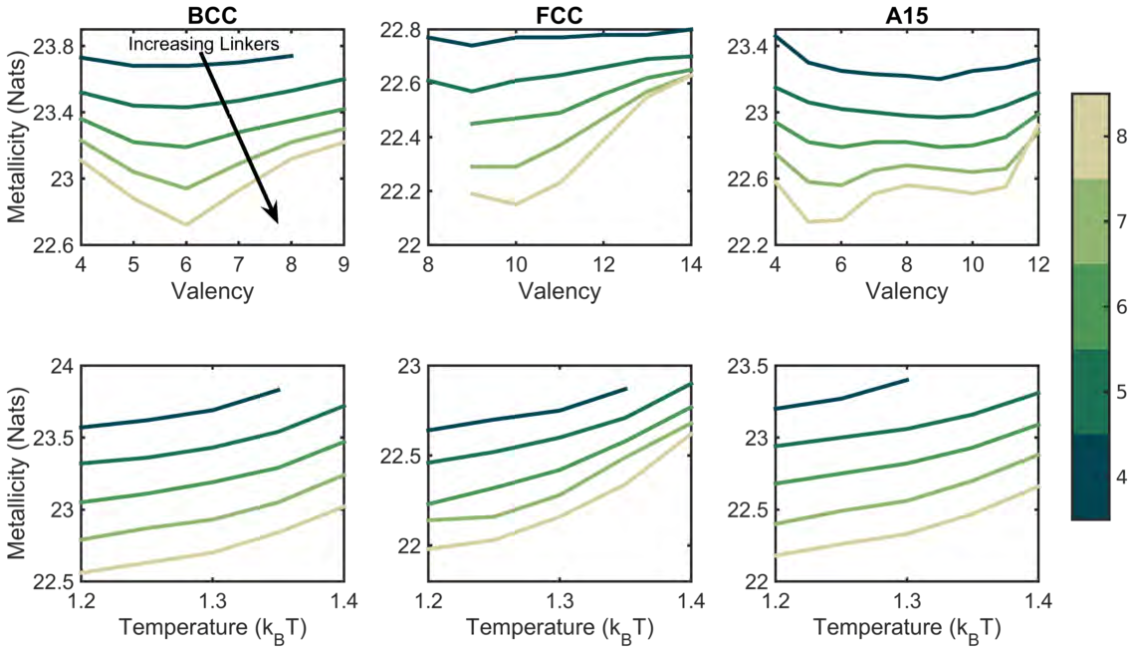

Figure 7.2. (**A**) Metallicity as a function of valency obtained from simulations of BCC (left), FCC (middle) and A15 (right) phases at temperatures of $k_BT = 1.3$. For PAE grafted with a large number of strands minimums are clearly seen, corresponding to ideal compound stoichiometric ratios (**B**) Metallicity as a function of temperature for BCC (valency of 6), FCC (valency of 10) and A15 (valency of 5). The degree of metallicity increases with temperature and is clearly controllable.

valency fills the conduction band and thus increases conductivity again. The amount of thermal excitations in our case is given by Boltzmann statistics and a probability $P \sim \exp(-E_g/k_BT)$, where E_g is the bandgap energy, rather than Fermi-Dirac statistics. Reducing the number of linkers on small PAE reduces the binding energy. In this picture of nearly-free electrons, this leads to a vanishing bandgap and thermally filled conduction band. Conversely, in strongly interacting PAEs, this leads to a large bandgap and a transition to an insulator state.

In PAE systems, the small particles, which behave as nearly free electrons, have energies close to room temperature and therefore, the Fermi liquid approach is invalid. While the crystals show a metallic character, not all the volume is accessible to small particles. Since many PAEs can occupy similar energy states, the Fermi surface is not a relevant concept to employ to study the

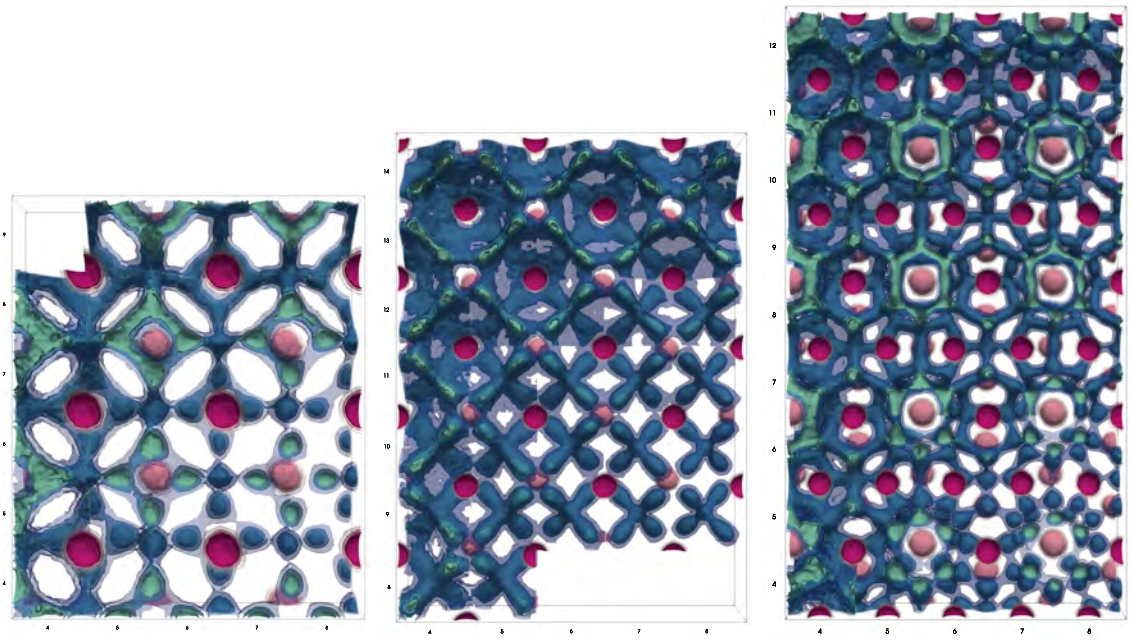

Figure 7.3. Boltzmann volumes constructed from four equally probable partitions of space as a function of linker number and metal valency. Crystal lattices are reconstructed by taking 1/8th of individual unit cells and using the cubic mirror planes to obtain global symmetries for BCC (left), FCC (center) and A15 (right) lattices. Position of large particles are indicated in red but are not to scale. Temperature is set to $k_BT = 1.30$. Images are numerically smoothed by Gaussian blur for visualization purposes. Missing data indicates numerically unstable phases.

metal-insulator transition. Rather, the localization is characterized by isoprobable volumes, which we call Boltzmann volumes as opposed to Fermi surfaces of quantum solids. We can probe the changes in metallicity in terms of Boltzmann volumes and the real space localization of PAEs in the system. Indeed on Fig. 7.3A, we can clearly see the localization into the AB_6 lattice. As valency is increased past the ideal value of six, the Boltzmann volume forms more extended states as a classical analogue of metal-insulator transitions of solids.

When PAEs are fully localized and assume their building block ground state, we recover compound lattices. The BCC lattice correspond to a previously observed AB_6 lattice (Fig. 7.4A). Other lattices have not been previously observed in PAE systems. The compound lattice of the

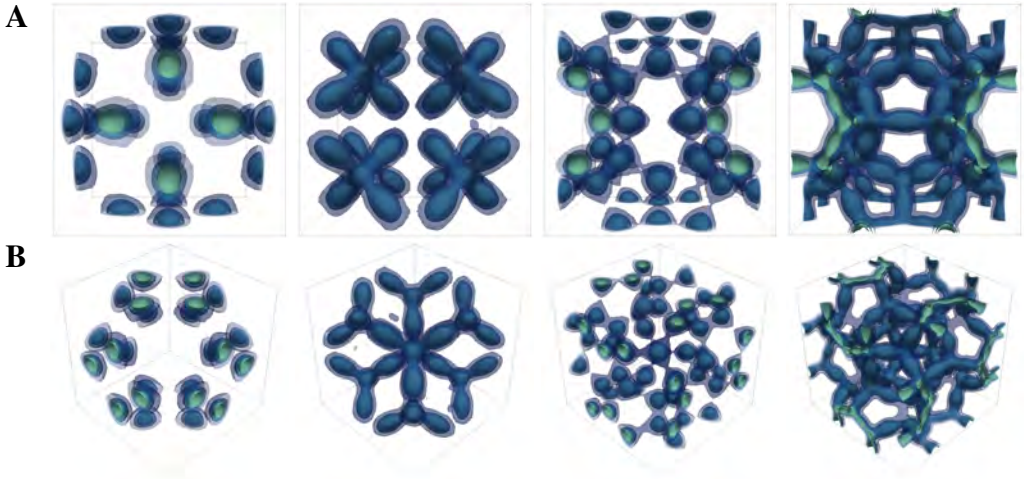

Figure 7.4. Boltzmann volumes of compound lattices for AB_6 lattice (BCC), A_4B_40 lattice (FCC), A_8B_46 lattice (A15) and A_8B_80 lattice (A15), viewed from side (**A**) and top (**B**). Cubic unit cell is drawn for clarity

FCC structure is a fully filled high temperature Cu_2Se lattice (Fig. 7.4B, A_4B_{40} structure, Fm3m, Wyckoff positions 8c and 32f), while the A15 shows two possible lattices, either clathrate type I (Fig. 7.4C, A_8B_{46} structure, equivalent to Ba_8Si_{46}) or an unobserved crystal (Fig. 7.4D, A_8B_{80} lattice, Pm3n, Wyckoff positions: 6c, 12f, 16i, 24j and 24k). Appearance of metallic phases open new avenues even for ionic crystal structures. By changing the binding energy of DNA strands one could attempt to form a metal lattice at elevated temperatures followed by a transition into an insulator compound.

Interestingly, the last two compounds both correspond to thermoelectric intermetallic structures. The appearance of complex metallic alloys (CMA) phases is also highly relevant to understanding and probing fundamentals of crystal formation. A currently open question in the CMA field is: "why do they form ?" (see[**160**] for further reading on the subject). In particular, CMA are stabilized by formation of a pseudogap and a depletion of the density of states around the Fermi energy, which is strikingly similar to the solid state analogy we described with a nearly free electron model. Moreover, we also find that metallicity, which should correlate with mobility, increases

with temperature just as electronic conductivity in CMA. We thus believe this system could be used as a platform to further study complex atomic systems.

As they are outside the previously established literature on spherical DNA-mediated assemblies they open a whole new design space. In particular, they should allow for studies of metallic alloys by using ternary A-B-C mixtures of PAEs. Equivalent to atomic electronegativity, interactions between electrons and different metallic ions can be tuned by changing the A-C and A-B hybridization energies independently, a parameter which cannot be finely controlled in atomic systems, but dictates metal solubilities and CMA phases obtained. Furthermore, electron core shells of the metallic ions can be controlled by particle shape. In previous works, PAE shape was referred to as an equivalent to atomic orbitals[**33**]. In retrospective, PAE shape dictates valence orbitals for ionic systems, while for metals it should dictate core orbitals.

In conclusion, this work shows that metallic crystals can be self-assembled using DNA programmable building blocks. The smaller PAEs can behave as electrons in metals or as building blocks of ionic crystals, which can be continuously tuned. Specifically, their metallic character can be tailored for specific applications by choosing appropriate DNA sticky end sequences. The tunable fundamental character of the building blocks is also relevant to other disciplines than PAEs as they can be used to probe fundamentals of complex systems. As we have shown, CMA arise naturally in these systems without involving quantum mechanics.

CHAPTER 8

Conclusions and future work

In the first part of this thesis, I presented work on orbital representations of colloids. This method is able to handle any colloid described by a density of particles oscillating around some mean density as long as the potential energy function possesses a Fourier transform. It is highly suitable for polymer-grafted particles of arbitrary shapes. While the method is able to deal with deformation of the shell during assembly processes, it is still not suitable for use with DNA systems. This is due to the depletion of available free bases of the sticky ends. While the discussion would suggest that it only plagues our mean-field approximation, we have to realize that all of the currently used coarse-graining schemes that remove explicit chains suffer from the same problem. For instance, in [**161**], an interaction potential is assigned to every bead that constitutes the surface of the colloids, which can be mapped to a time-static orbital representation. This is a problem that needs to be addressed in the coarse-graining community. At this point, the only solution I have envisioned is a separation of the orbitals into free and bound components. Yet, this does not solve the problem as they are physically coupled. This needs to be studied in much greater detail.

In the second part, I have discussed four different experimental systems. In the first, I simulated the phase diagram of polyhedrons. The phases correspond to close packed structures for short DNA and sphere-like phases for long DNA. There is a crossover regime for cubes in which symmetry of the lattice is broken with respect to the underlying particles. This is an interesting regime as it can be used to extend the available crystal lattices and symmetries. The regime is extremely sensitive to changes in the DNA grafting density, and shows a variety of lattices from tetragonal

lattice down to triclinic lattices. Changing the DNA grafting density may be a potential challenge in experiments that will require exploration.

In the second article, I have shown that hexagonal crystals formed by binary PAEs exhibit large energy barriers between different planes with identical Miller indices. This results in a long hexagonal rod crystal habit exposing high energy facets, a consequence of the kinetic Wulff shape construction. This shape is highly reproducible and can be externally controlled, for instance by the salt concentration. As mentioned very early on, this is suitable for optical properties control. There are remaining binary compounds to be looked at, namely Cr_3Si and Cs_6C_{60}. Those are cubic lattices but it would be interesting to look at the degree of control one has over their crystal habit.

In the third article, I have shown that increasing salt concentration in water during assembly results in a slowdown of the attachment process and formation of larger crystals. Enabling control over kinetics enables tailoring of the crystal sizes, which is important for many applications.

The last article of this part deals with mixtures of large particles (atom-equivalents) with small particles (electron-equivalents). In this work, we have found that the system assembles into various lattices corresponding to metals. By reducing the temperature, electron-equivalent particles take specific sites in the crystals, an emulation of Mott transitions in atomic systems. These lattices then correspond to complex metal alloys or intermetallics. This is highly interesting from a fundamental point of view. As mentioned early on, we have limited knowledge of these systems in the atomic world. This soft system can be used as a testing platform to see why complex metal alloys form in the first place. For this purpose, ternary systems could be employed, with DNA binding strength playing the role of electronegativity. In this representation, the system is free of quantum behavior, which should simplify interpretation. Moreover, the equivalent metal valency can be chosen arbitrarily and independently of the atom-equivalent, something that is impossible in natural elements.

Yet, there remains some unfilled gaps that should be explored. In particular, how closely related our intermetallic phases are with the atomic equivalent phases. The similarity between solid-state physics and behavior of the system is striking, but the Mott transition is not identical in nature. Our electrons transition towards atoms instead of localized electrons. The quantum nature of electrons is likely to be the source of this difference, but a more in-depth study is warranted.

Moreover, I introduced early on how defects can be used to concentrate electric fields. However, there is another approach that is tempting in these self-assembled materials: defect engineering. These defects can be made by introducing an additional type of building block nearly identical to one of the blocks used to build the crystal. With small changes, for instance to the DNA length, the interaction between defects may be tailored. Each of these defects would represent a single optical resonator. Collections of broad optical resonances may lead to formation of sharp spectral features through the interaction of different resonators and formation of the so-called Fano-Feshbach resonances [**162**]. While the exact origin of these modes is still up to debate (see [**163**] for Mie-resonance based description and [**164**] for radiation-less based description), they could provide easy access to tailoring resonant properties.

References

1. R. J. Macfarlane, B. Lee, H. D. Hill, A. J. Senesi, S. Seifert, and C. A. Mirkin, "Assembly and organization processes in dna-directed colloidal crystallization," *Proceedings of the National Academy of Sciences*, vol. 106, no. 26, pp. 10493–10498, 2009.

2. I. Langmuir, "The role of attractive and repulsive forces in the formation of tactoids, thixotropic gels, protein crystals and coacervates," *The Journal of Chemical Physics*, vol. 6, no. 12, pp. 873–896, 1938.

3. E. Auyeung, T. I. N. G. Li, A. J. Senesi, A. L. Schmucker, B. C. Pals, M. O. de la Cruz, and C. A. Mirkin, "DNA-mediated nanoparticle crystallization into Wulff polyhedra," *Nature*, vol. 505, p. 73, Nov. 2013.

4. R. V. Thaner, Y. Kim, T. I. N. G. Li, R. J. Macfarlane, S. T. Nguyen, M. Olvera de la Cruz, and C. A. Mirkin, "Entropy-Driven Crystallization Behavior in DNA-Mediated Nanoparticle Assembly," *Nano Letters*, vol. 15, pp. 5545–5551, Aug. 2015.

5. R. J. Macfarlane, B. Lee, M. R. Jones, N. Harris, G. C. Schatz, and C. A. Mirkin, "Nanoparticle Superlattice Engineering with DNA," *Science*, vol. 334, p. 204, Oct. 2011.

6. M. N. O'Brien, M. R. Jones, K. A. Brown, and C. A. Mirkin, "Universal noble metal nanoparticle seeds realized through iterative reductive growth and oxidative dissolution reactions," *Journal of the American Chemical Society*, vol. 136, no. 21, pp. 7603–7606, 2014. PMID: 24830921.

7. C. R. Laramy, K. A. Brown, M. N. O'Brien, and C. A. Mirkin, "High-throughput, algorithmic determination of nanoparticle structure from electron microscopy images," *ACS Nano*, vol. 9, no. 12, pp. 12488–12495, 2015. PMID: 26588107.

8. M. R. Jones, R. J. Macfarlane, B. Lee, J. Zhang, K. L. Young, A. J. Senesi, and C. A. Mirkin, "DNA-nanoparticle superlattices formed from anisotropic building blocks," *Nature Materials*, vol. 9, p. 913, Oct. 2010.

9. J. D. Brodin, E. Auyeung, and C. A. Mirkin, "DNA-mediated engineering of multicomponent enzyme crystals," *Proceedings of the National Academy of Sciences*, vol. 112, no. 15, pp. 4564–4569, 2015.

10. T. Kuech, *Handbook of Crystal Growth: Thin Films and Epitaxy*. Handbook of Crystal Growth, Elsevier Science, 2014.

11. M. X. Wang, S. E. Seo, P. A. Gabrys, D. Fleischman, B. Lee, Y. Kim, H. A. Atwater, R. J. Macfarlane, and C. A. Mirkin, "Epitaxy: Programmable Atom Equivalents Versus Atoms," *ACS Nano*, vol. 11, pp. 180–185, Jan. 2017.

12. P. A. Gabrys, S. E. Seo, M. X. Wang, E. Oh, R. J. Macfarlane, and C. A. Mirkin, "Lattice Mismatch in Crystalline Nanoparticle Thin Films," *Nano Letters*, vol. 18, pp. 579–585, Jan. 2018.

13. C. Knorowski, S. Burleigh, and A. Travesset, "Dynamics and statics of dna-programmable nanoparticle self-assembly and crystallization," *Phys. Rev. Lett.*, vol. 106, p. 215501, May 2011.

14. T. I. Li, R. Sknepnek, R. J. Macfarlane, C. A. Mirkin, and M. Olvera de la Cruz, "Modeling the Crystallization of Spherical Nucleic Acid Nanoparticle Conjugates with Molecular Dynamics Simulations," *Nano Letters*, vol. 12, pp. 2509–2514, May 2012.

15. D. M. Hinckley and J. J. de Pablo, "Coarse-Grained Ions for Nucleic Acid Modeling," *Journal of Chemical Theory and Computation*, vol. 11, pp. 5436–5446, Nov. 2015.

16. D. M. Hinckley, G. S. Freeman, J. K. Whitmer, and J. J. de Pablo, "An experimentally-informed coarse-grained 3-site-per-nucleotide model of DNA: Structure, thermodynamics, and dynamics of hybridization," *The Journal of Chemical Physics*, vol. 139, p. 144903, Oct. 2013.

17. J. B. Pendry, A. J. Holden, D. J. Robbins, and W. J. Stewart, "Magnetism from conductors and enhanced nonlinear phenomena," *IEEE Transactions on Microwave Theory and Techniques*, vol. 47, pp. 2075–2084, Nov 1999.

18. J. E. G. J. Wijnhoven and W. L. Vos, "Preparation of photonic crystals made of air spheres in titania," *Science*, vol. 281, no. 5378, pp. 802–804, 1998.

19. D. J. Park, C. Zhang, J. C. Ku, Y. Zhou, G. C. Schatz, and C. A. Mirkin, "Plasmonic photonic crystals realized through DNA-programmable assembly," *Proceedings of the National Academy of Sciences*, vol. 112, no. 4, pp. 977–981, 2015.

20. A. Travesset, "Soft skyrmions, spontaneous valence and selection rules in nanoparticle superlattices," *ACS Nano*, vol. 11, no. 6, pp. 5375–5382, 2017. PMID: 28514592.

21. M. A. Boles and D. V. Talapin, "Many-body effects in nanocrystal superlattices: Departure from sphere packing explains stability of binary phases," *Journal of the American Chemical Society*, vol. 137, no. 13, pp. 4494–4502, 2015. PMID: 25773648.

22. C. Li, J. Shen, C. Peter, and N. F. A. van der Vegt, "A chemically accurate implicit-solvent coarse-grained model for polystyrenesulfonate solutions," *Macromolecules*, vol. 45, no. 5, pp. 2551–2561, 2012.

23. E. Brini, E. A. Algaer, P. Ganguly, C. Li, F. Rodriguez-Ropero, and N. F. A. van der Vegt, "Systematic coarse-graining methods for soft matter simulations - a review," *Soft Matter*, vol. 9, pp. 2108–2119, 2013.

24. W. G. Noid, *Systematic Methods for Structurally Consistent Coarse-Grained Models*, pp. 487–531. Totowa, NJ: Humana Press, 2013.

25. F. Sciortino, A. Giacometti, and G. Pastore, "Phase diagram of janus particles," *Phys. Rev. Lett.*, vol. 103, p. 237801, 2009.

26. Q. Chen, S. C. Bae, and S. Granick, "Directed self-assembly of a colloidal kagome lattice," *Nature*, vol. 469, no. 7330, pp. 381–384, 2011.

27. J. Zhang, B. A. Grzybowski, and S. Granick, "Janus particle synthesis, assembly, and application," *Langmuir*, vol. 33, no. 28, pp. 6964–6977, 2017.

28. J. Yan, M. Han, J. Zhang, C. Xu, E. Luijten, and S. Granick, "Reconfiguring active particles by electrostatic imbalance," *Nat Mater*, vol. 15, no. 10, pp. 1095–1099, 2016.

29. M. Han, J. Yan, S. Granick, and E. Luijten, "Effective temperature concept evaluated in an active colloid mixture," *Proceedings of the National Academy of Sciences*, vol. 114, no. 29, pp. 7513–7518, 2017.

30. S. Sacanna, M. Korpics, K. Rodriguez, L. Colón-Meléndez, S.-H. Kim, D. J. Pine, and G.-R. Yi, "Shaping colloids for self-assembly," *Nature Communications*, vol. 4, p. 1688, Apr 2013.

31. X. Zheng, M. Liu, M. He, D. J. Pine, and M. Weck, "Shape-shifting patchy particles," *Angewandte Chemie International Edition*, vol. 129, no. 20, pp. 5599–5603, 2017.

32. H. R. Vutukuri, A. Imhof, and A. vanBlaaderen, "Fabrication of polyhedral particles from spherical colloids and their self-assembly into rotator phases," *Angewandte Chemie International Edition*, vol. 53, pp. 13830–13834, 2014.

33. M. N. O'Brien, M. Girard, H.-X. Lin, J. A. Millan, M. Olvera de la Cruz, B. Lee, and C. A. Mirkin, "Exploring the zone of anisotropy and broken symmetries in dna-mediated

nanoparticle crystallization," *Proceedings of the National Academy of Sciences*, vol. 113, no. 38, pp. 10485–10490, 2016.

34. S. Mann, "Self-assembly and transformation of hybrid nano-objects and nanostructures under equilibrium and non-equilibrium conditions," *Nat Mater*, vol. 8, pp. 781–792, 2009.

35. J. J. McManus, P. Charbonneau, E. Zaccarelli, and N. Asherie, "The physics of protein self-assembly," *Current Opinion in Colloid & Interface Science*, vol. 22, pp. 73–79, 2016.

36. E. Lindahl and M. S. P. Sansom, "Membrane proteins: molecular dynamics simulations," *Current Opinion in Structural Biology*, vol. 18, pp. 425–431, 2008.

37. M. X. Wang, J. D. Brodin, J. A. Millan, S. E. Seo, M. Girard, M. Olvera de la Cruz, B. Lee, and C. A. Mirkin, "Altering dna-programmable colloidal crystallization paths by modulating particle repulsion," *Nano Letters*, vol. 17, pp. 5126–5132, 2017.

38. U. Agarwal and F. A. Escobedo, "Mesophase behaviour of polyhedral particles," *Nature Materials*, vol. 10, p. 230, Feb. 2011.

39. S. Torquato and Y. Jiao, "Dense packings of the Platonic and Archimedean solids," *Nature*, vol. 460, p. 876, Aug. 2009.

40. J. de Graaf, R. van Roij, and M. Dijkstra, "Dense regular packings of irregular nonconvex particles," *Phys. Rev. Lett.*, vol. 107, p. 155501, 2011.

41. P. F. Damasceno, M. Engel, and S. C. Glotzer, "Predictive Self-Assembly of Polyhedra into Complex Structures," *Science*, vol. 337, p. 453, July 2012.

42. J. Downs, K. Gubbins, S. Murad, and C. Gray, "Spherical harmonic expansion of the intermolecular site-site potential," *Molecular Physics*, vol. 37, pp. 129–140, 1979.

43. R. A. Sack, "Expansions in spherical harmonics. iv. integral form of the radial dependence," *Journal of Mathematical Physics*, vol. 8, pp. 1774–1784, 1967.

44. K. Ruedenberg, "Bipolare entwicklungen, fouriertransformation und molekulare mehrzentren-integrale," *Theoretica chimica acta*, vol. 7, pp. 359–366, 1967.

45. J. G. Gay and B. J. Berne, "Modification of the overlap potential to mimic a linear sitesite potential," *The Journal of Chemical Physics*, vol. 74, pp. 3316–3319, 1981.

46. D. J. Cleaver, C. M. Care, M. P. Allen, and M. P. Neal, "Extension and generalization of the gay-berne potential," *Phys. Rev. E*, vol. 54, pp. 559–567, 1996.

47. D. J. Ashton, R. L. Jack, and N. B. Wilding, "Self-assembly of colloidal polymers via depletion-mediated lock and key binding," *Soft Matter*, vol. 9, pp. 9661–9666, 2013.

48. D. Marx and J. Hutter, "Ab initio molecular dynamics: Theory and implementation," *Modern methods and algorithms of quantum chemistry*, vol. 13, pp. 301–449, 2000.

49. S. J. Plimpton, "Fast parallel algorithms for short-range molecular dynamics," *J. Comp. Phys.*, vol. 117, pp. 1–19, 1995.

50. W. Kung and M. O. de la Cruz, "Mediation of long-range attraction selectively between negatively charged colloids on surfaces by solvation," *The Journal of Chemical Physics*, vol. 127, no. 24, p. 244907, 2007.

51. W. Kung, P. Gonzalez-Mozuelos, and M. O. de la Cruz, "A minimal model of nanoparticle crystallization in polar solvents via steric effects," *The Journal of Chemical Physics*, vol. 133, p. 074704, 2010.

52. Z.-G. Wang, "Fluctuation in electrolyte solutions: The self energy," *Phys. Rev. E*, vol. 81, p. 021501, 2010.

53. J. M. Dempster and M. Olvera de la Cruz, "Aggregation of heterogeneously charged colloids," *ACS Nano*, vol. 10, pp. 5909–5915, 2016.

54. N. Baddour, "Operational and convolution properties of three-dimensional fourier transforms in spherical polar coordinates," *J. Opt. Soc. Am. A*, vol. 27, pp. 2144–2155, 2010.

55. M. Boyle, "Angular velocity of gravitational radiation from precessing binaries and the corotating frame," *Phys. Rev. D*, vol. 87, p. 104006, 2013.

56. M. Toyoda and T. Ozaki, "Fast spherical bessel transform via fast fourier transform and recurrence formula," *Computer Physics Communications*, vol. 181, pp. 277–282, 2010.

57. B. Keinert, M. Innmann, M. Sänger, and M. Stamminger, "Spherical fibonacci mapping," *ACM Trans. Graph.*, vol. 34, pp. 193:1–193:7, 2015.

58. R. Kjellander and R. Ramirez, "Yukawa multipole electrostatics and nontrivial coupling between electrostatic and dispersion interactions in electrolytes," *Journal of Physics: Condensed Matter*, vol. 20, p. 494209, 2008.

59. W. M. Brown, T. D.Nguyen, MiguelFuentes-Cabrerab, J. D.Fowlkes, P. D.Rack, MarkBerger, and A. S.Bland, "An evaluation of molecular dynamics performance on the hybrid cray xk6 supercomputer," *Procedia Computer Science*, vol. 9, pp. 186–195, 2012.

60. J. C. Shelley and G. N. Patey, "A comparison of liquidvapor coexistence in charged hard sphere and charged hard dumbbell fluids," *The Journal of Chemical Physics*, vol. 103, pp. 8299–8301, 1995.

61. M. E. van Leeuwen and B. Smit, "What makes a polar liquid a liquid?," *Phys. Rev. Lett.*, vol. 71, pp. 3991–3994, 1993.

62. R. Agrawal and D. A. Kofke, "Thermodynamic and structural properties of model systems at solid-fluid coexistence," *Molecular Physics*, vol. 85, no. 1, pp. 23–42, 1995.

63. A. Travesset, "Topological structure prediction in binary nanoparticle superlattices," *Soft Matter*, vol. 13, pp. 147–157, 2017.

64. Y. Levin, P. S. Kuhn, and M. C. Barbosa, "Criticality in polar fluids," *Physica A: Statistical Mechanics and its Applications*, vol. 292, pp. 129–136, 2001.

65. I. S. Gradshteyn and I. M. Ryzhik, *Table of integrals, series, and products*. Elsevier/Academic Press, Amsterdam, seventh ed., 2007.

66. C. A. Mirkin, R. L. Letsinger, R. C. Mucic, and J. J. Storhoff, "A DNA-based method for rationally assembling nanoparticles into macroscopic materials," *Nature*, vol. 382, p. 607, Aug. 1996.

67. X. Ye, C. Zhu, P. Ercius, S. N. Raja, M. R. He, Bo amd Jones, M. R. Hauwiller, Y. Liu, T. Xu, and A. P. Alivisatos, "Structural diversity in binary superlattices self-assembled from polymer-grafted nanocrystals," *Nat. Commun.*, vol. 6, p. 10052, Dec 2015.

68. J. N. Israelachvili, *Intermolecular and Surface Forces, 3rd Edition*. Academic Press, 2011.

69. K. J. Bishop, C. E. Wilmer, S. Soh, and B. A. Grzybowski, "Nanoscale forces and their uses in self-assembly," *Small*, vol. 5, pp. 1600–1630, Jul 2009.

70. M. Girard, T. D. Nguyen, and M. O. de la Cruz, "Orbitals for classical arbitrary anisotropic colloidal potentials," *Phys. Rev. E*, vol. 96, p. 053309, Nov 2017.

71. B. M. Mladek, J. Fornleitner, F. J. Martinez-Veracoechea, A. Dawid, and D. Frenkel, "Procedure to construct a multi-scale coarse-grained model of dna-coated colloids from experimental data," *Soft Matter*, vol. 9, pp. 7342–7355, 2013.

72. X. P. Liu, Y. Ni, and L. H. He, "Molecular dynamics simulation of interparticle spacing and many-body effect in gold supracrystals," *Nanotechnology*, vol. 27, no. 13, p. 135707, 2016.

73. N. Horst and A. Travesset, "Prediction of binary nanoparticle superlattices from soft potentials," *The Journal of Chemical Physics*, vol. 144, no. 1, p. 014502, 2016.

74. G. Bauer, N. Gribova, A. Lange, C. Holm, and J. Gross, "Three-body effects in triplets of capped gold nanocrystals," *Molecular Physics*, vol. 115, no. 9-12, pp. 1031–1040, 2017.

75. E. M. Y. Lee, A. J. Mork, A. P. Willard, and W. A. Tisdale, "Including surface ligand effects in continuum elastic models of nanocrystal vibrations," *The Journal of Chemical Physics*, vol. 147, no. 4, p. 044711, 2017.

76. G. Zhang and T. Schlick, "Lin: A new algorithm to simulate the dynamics of biomolecules by combining implicitintegration and normal mode techniques," *Journal of Computational Chemistry*, vol. 14, no. 10, pp. 1212–1233, 1993.

77. A. P. Alivisatos, K. P. Johnsson, X. Peng, T. E. Wilson, C. J. Loweth, M. P. Bruchez Jr, and P. G. Schultz, "Organization of 'nanocrystal molecules' using DNA," *Nature*, vol. 382, p. 609, Aug. 1996.

78. E. V. Shevchenko, D. V. Talapin, N. A. Kotov, S. O'Brien, and C. B. Murray, "Structural diversity in binary nanoparticle superlattices," *Nature*, vol. 439, p. 55, Jan. 2006.

79. Y. Min, M. Akbulut, K. Kristiansen, Y. Golan, and J. Israelachvili, "The role of interparticle and external forces in nanoparticle assembly," *Nature Materials*, vol. 7, p. 527, July 2008.

80. B. K. J. M., W. C. E., S. Siowling, and G. B. A., "Nanoscale forces and their uses in self-assembly," *Small*, vol. 5, no. 14, pp. 1600–1630, 2009.

81. M. R. Jones, K. D. Osberg, R. J. Macfarlane, M. R. Langille, and C. A. Mirkin, "Templated techniques for the synthesis and assembly of plasmonic nanostructures," *Chemical Reviews*, vol. 111, no. 6, pp. 3736–3827, 2011. PMID: 21648955.

82. M. R. Jones, N. C. Seeman, and C. A. Mirkin, "Programmable materials and the nature of the DNA bond," *Science*, vol. 347, Feb. 2015.

83. C. A. Silvera Batista, R. G. Larson, and N. A. Kotov, "Nonadditivity of nanoparticle interactions," *Science*, vol. 350, Oct. 2015.

84. C. L. Choi and A. P. Alivisatos, "From artificial atoms to nanocrystal molecules: Preparation and properties of more complex nanostructures," *Annual Review of Physical Chemistry*, vol. 61, no. 1, pp. 369–389, 2010. PMID: 20055683.

85. R. J. Macfarlane, M. N. O'Brien, S. H. Petrosko, and C. A. Mirkin, "Nucleic acid-modified nanostructures as programmable atom equivalents: Forging a new "table of elements"," *Angewandte Chemie International Edition*, vol. 52, no. 22, pp. 5688–5698, 2012.

86. S. Y. Park, A. K. R. Lytton-Jean, B. Lee, S. Weigand, G. C. Schatz, and C. A. Mirkin, "DNA-programmable nanoparticle crystallization," *Nature*, vol. 451, p. 553, Jan. 2008.

87. D. Nykypanchuk, M. M. Maye, D. van der Lelie, and O. Gang, "DNA-guided crystallization of colloidal nanoparticles," *Nature*, vol. 451, p. 549, Jan. 2008.

88. L. D. Michele and E. Eiser, "Developments in understanding and controlling self assembly of dna-functionalized colloids," *Phys. Chem. Chem. Phys.*, vol. 15, pp. 3115–3129, 2013.

89. M. N. O'Brien, M. R. Jones, B. Lee, and C. A. Mirkin, "Anisotropic nanoparticle complementarity in DNA-mediated co-crystallization," *Nature Materials*, vol. 14, p. 833, May 2015.

90. W. B. Rogers and V. N. Manoharan, "Programming colloidal phase transitions with DNA strand displacement," *Science*, vol. 347, p. 639, Feb. 2015.

91. Y. Kim, R. J. Macfarlane, M. R. Jones, and C. A. Mirkin, "Transmutable nanoparticles with reconfigurable surface ligands," *Science*, vol. 351, p. 579, Feb. 2016.

92. W. Liu, M. Tagawa, H. L. Xin, T. Wang, H. Emamy, H. Li, K. G. Yager, F. W. Starr, A. V. Tkachenko, and O. Gang, "Diamond family of nanoparticle superlattices," *Science*, vol. 351, p. 582, Feb. 2016.

93. A. J. Senesi and B. Lee, "Small-angle scattering of particle assemblies," *Journal of Applied Crystallography*, vol. 48, pp. 1172–1182, Aug 2015.

94. T. Li, A. J. Senesi, and B. Lee, "Small Angle X-ray Scattering for Nanoparticle Research," *Chemical Reviews*, vol. 116, pp. 11128–11180, Sept. 2016.

95. J. Henzie, M. Grnwald, A. Widmer-Cooper, P. L. Geissler, and P. Yang, "Self-assembly of uniform polyhedral silver nanocrystals into densest packings and exoticsuperlattices," *Nature Materials*, vol. 11, p. 131, Nov. 2011.

96. R. Ni, A. P. Gantapara, J. de Graaf, R. van Roij, and M. Dijkstra, "Phase diagram of colloidal hard superballs: from cubes via spheres to octahedra," *Soft Matter*, vol. 8, pp. 8826–8834, 2012.

97. A. P. Gantapara, J. de Graaf, R. van Roij, and M. Dijkstra, "Phase diagram and structural diversity of a family of truncated cubes: Degenerate close-packed structures and vacancy-rich states," *Phys. Rev. Lett.*, vol. 111, p. 015501, Jul 2013.

98. G. van Anders, N. K. Ahmed, R. Smith, M. Engel, and S. C. Glotzer, "Entropically Patchy Particles: Engineering Valence through Shape Entropy," *ACS Nano*, vol. 8, pp. 931–940, Jan. 2014.

99. J. A. Anderson, C. D. Lorenz, and A. Travesset, "General purpose molecular dynamics simulations fully implemented on graphics processing units," *Journal of Computational Physics*, vol. 227, no. 10, pp. 5342 – 5359, 2008.

100. J. Glaser, T. D. Nguyen, J. A. Anderson, P. Lui, F. Spiga, J. A. Millan, D. C. Morse, and S. C. Glotzer, "Strong scaling of general-purpose molecular dynamics simulations on GPUs," *Computer Physics Communications*, vol. 192, pp. 97 – 107, 2015.

101. Y. Zhang, F. Lu, D. van der Lelie, and O. Gang, "Continuous phase transformation in nanocube assemblies," *Phys. Rev. Lett.*, vol. 107, p. 135701, Sep 2011.

102. R. D. Batten, F. H. Stillinger, and S. Torquato, "Phase behavior of colloidal superballs: Shape interpolation from spheres to cubes," *Phys. Rev. E*, vol. 81, p. 061105, Jun 2010.

103. M. A. Boles and D. V. Talapin, "Self-Assembly of Tetrahedral CdSe Nanocrystals: Effective "Patchiness" via Anisotropic Steric Interaction," *Journal of the American Chemical Society*, vol. 136, pp. 5868–5871, Apr. 2014.

104. A. J. Senesi, D. J. Eichelsdoerfer, K. A. Brown, B. Lee, E. Auyeung, C. H. J. Choi, R. J. Macfarlane, K. L. Young, and C. A. Mirkin, "Oligonucleotide flexibility dictates crystal quality in dna-programmable nanoparticle superlattices," *Advanced Materials*, vol. 26, no. 42, pp. 7235–7240, 2014.

105. S. N. Barnaby, R. V. Thaner, M. B. Ross, K. A. Brown, G. C. Schatz, and C. A. Mirkin, "Modular and Chemically Responsive Oligonucleotide "Bonds" in Nanoparticle Superlattices," *Journal of the American Chemical Society*, vol. 137, pp. 13566–13571, Oct. 2015.

106. G. Wulff, "On the question of speed of growth and dissolution of crystal surfaces," *Z. Kristallogr*, vol. 34, pp. 449–530, 1901.

107. R. F. Sekerka, "Equilibrium and growth shapes of crystals: how do they differ and why should we care?," *Crystal Research and Technology*, vol. 40, no. 45, pp. 291–306, 2005.

108. R. W. Balluffi, S. Allen, and W. C. Carter, *Kinetics of materials*. John Wiley & Sons, 2005.

109. D. Shi, V. Adinolfi, R. Comin, M. Yuan, E. Alarousu, A. Buin, Y. Chen, S. Hoogland, A. Rothenberger, and K. Katsiev, "Low trap-state density and long carrier diffusion in organolead trihalide perovskite single crystals," *Science*, vol. 347, no. 6221, pp. 519–522, 2015.

110. W. Nie, H. Tsai, R. Asadpour, J.-C. Blancon, A. J. Neukirch, G. Gupta, J. J. Crochet, M. Chhowalla, S. Tretiak, and M. A. Alam, "High-efficiency solution-processed perovskite solar cells with millimeter-scale grains," *Science*, vol. 347, no. 6221, pp. 522–525, 2015.

111. K. Watanabe, T. Taniguchi, and H. Kanda, "Direct-bandgap properties and evidence for ultraviolet lasing of hexagonal boron nitride single crystal," *Nature materials*, vol. 3, no. 6, p. 404, 2004.

112. T. Kessler, C. Hagemann, C. Grebing, T. Legero, U. Sterr, F. Riehle, M. J. Martin, L. Chen, and J. Ye, "A sub-40-mHz-linewidth laser based on a silicon single-crystal optical cavity," *Nature Photonics*, vol. 6, no. 10, p. 687, 2012.

113. M. B. Ross, J. C. Ku, V. M. Vaccarezza, G. C. Schatz, and C. A. Mirkin, "Nanoscale form dictates mesoscale function in plasmonic DNAnanoparticle superlattices," *Nature nanotechnology*, vol. 10, no. 5, p. 453, 2015.

114. M. B. Ross, M. G. Blaber, and G. C. Schatz, "Using nanoscale and mesoscale anisotropy to engineer the optical response of three-dimensional plasmonic metamaterials," *Nature Communications*, vol. 5, p. 4090, 2014.

115. H. Dong, Z. Chen, L. Sun, J. Lu, W. Xie, H. H. Tan, C. Jagadish, and X. Shen, "Whispering gallery modes in indium oxide hexagonal microcavities," *Applied physics letters*, vol. 94, no. 17, p. 173115, 2009.

116. C. Tessarek, G. Sarau, M. Kiometzis, and S. Christiansen, "High quality factor whispering gallery modes from self-assembled hexagonal GaN rods grown by metal-organic vapor phase epitaxy," *Optics express*, vol. 21, no. 3, pp. 2733–2740, 2013.

117. S.-H. Gong, S.-M. Ko, M.-H. Jang, and Y.-H. Cho, "Giant rabi splitting of whispering gallery polaritons in GaN/InGaN coreshell wire," *Nano letters*, vol. 15, no. 7, pp. 4517–4524, 2015.

118. R. W. Boyd, R. J. Gehr, G. L. Fischer, and J. E. Sipe, "Nonlinear optical properties of nanocomposite materials," *Pure and Applied Optics: Journal of the European Optical Society Part A*, vol. 5, no. 5, p. 505, 1996.

119. J. Zhang, X. Jin, P. I. Morales-Guzman, X. Yu, H. Liu, H. Zhang, L. Razzari, and J. P. Claverie, "Engineering the absorption and field enhancement properties of AuTiO2 nanohybrids via whispering gallery mode resonances for photocatalytic water splitting," *ACS nano*, vol. 10, no. 4, pp. 4496–4503, 2016.

120. A. Tao, P. Sinsermsuksakul, and P. Yang, "Tunable plasmonic lattices of silver nanocrystals," *Nature nanotechnology*, vol. 2, no. 7, p. 435, 2007.

121. X. Ye, J. Chen, B. T. Diroll, and C. B. Murray, "Tunable plasmonic coupling in self-assembled binary nanocrystal superlattices studied by correlated optical microspectrophotometry and electron microscopy," *Nano letters*, vol. 13, no. 3, pp. 1291–1297, 2013.

122. A. S. Urban, X. Shen, Y. Wang, N. Large, H. Wang, M. W. Knight, P. Nordlander, H. Chen, and N. J. Halas, "Three-dimensional plasmonic nanoclusters," *Nano letters*, vol. 13, no. 9, pp. 4399–4403, 2013.

123. S. E. Seo, M. X. Wang, C. M. Shade, J. L. Rouge, K. A. Brown, and C. A. Mirkin, "Modulating the bond strength of DNAnanoparticle superlattices," *ACS nano*, vol. 10, no. 2, pp. 1771–1779, 2015.

124. R. J. Macfarlane, M. R. Jones, A. J. Senesi, K. L. Young, B. Lee, J. Wu, and C. A. Mirkin, "Establishing the Design Rules for DNAMediated Programmable Colloidal Crystallization," *Angewandte Chemie*, vol. 122, no. 27, pp. 4693–4696, 2010.

125. J. I. Cutler, E. Auyeung, and C. A. Mirkin, "Spherical nucleic acids," *Journal of the American Chemical Society*, vol. 134, no. 3, pp. 1376–1391, 2012.

126. C. Zhang, R. J. Macfarlane, K. L. Young, C. H. J. Choi, L. Hao, E. Auyeung, G. Liu, X. Zhou, and C. A. Mirkin, "A general approach to DNA-programmable atom equivalents," *Nature Materials*, vol. 12, p. 741, May 2013.

127. Y. Zhang, F. Lu, K. G. Yager, D. van der Lelie, and O. Gang, "A general strategy for the DNA-mediated self-assembly of functional nanoparticles into heterogeneous systems," *Nature Nanotechnology*, vol. 8, p. 865, Oct. 2013.

128. M. N. O'Brien, H.-X. Lin, M. Girard, M. Olvera de la Cruz, and C. A. Mirkin, "Programming Colloidal Crystal Habit with Anisotropic Nanoparticle Building Blocks and DNA Bonds," *Journal of the American Chemical Society*, vol. 138, pp. 14562–14565, Nov. 2016.

129. S. E. Seo, T. Li, A. J. Senesi, C. A. Mirkin, and B. Lee, "The Role of Repulsion in Colloidal Crystal Engineering with DNA," *Journal of the American Chemical Society*, vol. 139, pp. 16528–16535, Nov. 2017.

130. M. Maye, D. Nykypanchuk, D. vanderLelie, and O. Gang, "DNA-Regulated Micro- and Nanoparticle Assembly," *Small*, vol. 3, pp. 1678–1682, Oct. 2007.

131. L. D. Marks and L. Peng, "Nanoparticle shape, thermodynamics and kinetics," *Journal of Physics: Condensed Matter*, vol. 28, p. 053001, Feb. 2016.

132. W. F. Berg, "Crystal Growth from Solutions," *Proceedings of the Royal Society A: Mathematical, Physical and Engineering Sciences*, vol. 164, pp. 79–95, Jan. 1938.

133. J. Villain, "The shape of crystals to come," *Nature*, vol. 350, p. 273, Mar. 1991.

134. E. Auyeung, R. J. Macfarlane, C. H. J. Choi, J. I. Cutler, and C. A. Mirkin, "Transitioning DNA-Engineered Nanoparticle Superlattices from Solution to the Solid State," *Advanced Materials*, vol. 24, pp. 5181–5186, Oct. 2012.

135. R. V. Zucker, D. Chatain, U. Dahmen, S. Hagège, and W. C. Carter, "New software tools for the calculation and display of isolated and attached interfacial-energy minimizing particle shapes," *Journal of Materials Science*, vol. 47, pp. 8290–8302, Dec 2012.

136. M. A. Boles, M. Engel, and D. V. Talapin, "Self-Assembly of Colloidal Nanocrystals: From Intricate Structures to Functional Materials," *Chemical Reviews*, vol. 116, pp. 11220–11289, Sept. 2016.

137. Z. Qian and D. S. Ginger, "Reversibly Reconfigurable Colloidal Plasmonic Nanomaterials," *Journal of the American Chemical Society*, vol. 139, pp. 5266–5276, Apr. 2017.

138. N. J. Halas, S. Lal, W.-S. Chang, S. Link, and P. Nordlander, "Plasmons in Strongly Coupled Metallic Nanostructures," *Chemical Reviews*, vol. 111, pp. 3913–3961, June 2011.

139. D. J. Park, J. C. Ku, L. Sun, C. M. Lethiec, N. P. Stern, G. C. Schatz, and C. A. Mirkin, "Directional emission from dye-functionalized plasmonic DNA superlattice microcavities," *Proceedings of the National Academy of Sciences*, vol. 114, no. 3, pp. 457–461, 2017.

140. S. Pal, Y. Zhang, S. K. Kumar, and O. Gang, "Dynamic Tuning of DNA-Nanoparticle Superlattices by Molecular Intercalation of Double Helix," *Journal of the American Chemical Society*, vol. 137, pp. 4030–4033, Apr. 2015.

141. J. J. De Yoreo, "Principles of Crystal Nucleation and Growth," *Reviews in Mineralogy and Geochemistry*, vol. 54, pp. 57–93, Jan. 2003.

142. R. J. Macfarlane, R. V. Thaner, K. A. Brown, J. Zhang, B. Lee, S. T. Nguyen, and C. A. Mirkin, "Importance of the DNA bond in programmable nanoparticle crystallization," *Proceedings of the National Academy of Sciences*, vol. 111, no. 42, pp. 14995–15000, 2014.

143. Y. Okahata, M. Kawase, K. Niikura, F. Ohtake, H. Furusawa, and Y. Ebara, "Kinetic Measurements of DNA Hybridization on an Oligonucleotide-Immobilized 27-MHz Quartz Crystal Microbalance," *Analytical Chemistry*, vol. 70, pp. 1288–1296, Apr. 1998.

144. E. M. Knipping, M. J. Lakin, K. L. Foster, P. Jungwirth, D. J. Tobias, R. B. Gerber, D. Dabdub, and B. J. Finlayson-Pitts, "Experiments and Simulations of Ion-Enhanced Interfacial Chemistry on Aqueous NaCl Aerosols," *Science*, vol. 288, no. 5464, pp. 301–306, 2000.

145. P. Gonzlez-Mozuelos, M. S. Yeom, and M. Olvera de la Cruz, "Molecular multivalent electrolytes: microstructure and screeninglengths," *The European Physical Journal E*, vol. 16, pp. 167–178, Feb. 2005.

146. Y. Li, M. Girard, M. Shen, J. A. Millan, and M. Olvera de la Cruz, "Strong attractions and repulsions mediated by monovalent salts," *Proceedings of the National Academy of Sciences*, vol. 114, no. 45, pp. 11838–11843, 2017.

147. A. A. Lee, C. S. Perez-Martinez, A. M. Smith, and S. Perkin, "Scaling Analysis of the Screening Length in Concentrated Electrolytes," *Physical Review Letters*, vol. 119, July 2017.

148. E. J. Mittemeijer and U. Welzel, "The state of the art of the diffraction analysis of crystallite size and lattice strain," *Zeitschrift fr Kristallographie*, vol. 223, Jan. 2008.

149. J. R. Kirkpatrick, "Crystal growth from the melt: A review," *American Mineralogist*, vol. 60, pp. 798–614, 1975.

150. S. Dhakal, K. L. Kohlstedt, G. C. Schatz, C. A. Mirkin, and M. Olvera de la Cruz, "Growth Dynamics for DNA-Guided Nanoparticle Crystallization," *ACS Nano*, vol. 7, pp. 10948–10959, Dec. 2013.

151. L. J. Moore, R. D. Dear, M. D. Summers, R. P. A. Dullens, and G. A. D. Ritchie, "Direct Observation of Grain Rotation-Induced Grain Coalescence in Two-Dimensional Colloidal Crystals," *Nano Letters*, vol. 10, pp. 4266–4272, Oct. 2010.

152. M. B. Ross, J. C. Ku, M. G. Blaber, C. A. Mirkin, and G. C. Schatz, "Defect tolerance and the effect of structural inhomogeneity in plasmonic DNA-nanoparticle superlattices," *Proceedings of the National Academy of Sciences*, vol. 112, pp. 10292–10297, Aug. 2015.

153. X. Lu and W. K. Olson, "3dna: a software package for the analysis, rebuilding and visualization of threedimensional nucleic acid structures," *Nucleic Acids Research*, vol. 31, no. 17, pp. 5108–5121, 2003.

154. L. Ratke and P. W. Voorhees, *Growth and coarsening: Ostwald ripening in material processing*. Springer Science & Business Media, 2013.

155. J. R. McMillan, J. D. Brodin, J. A. Millan, B. Lee, M. Olvera de la Cruz, and C. A. Mirkin, "Modulating Nanoparticle Superlattice Structure Using Proteins with Tunable Bond Distributions," *Journal of the American Chemical Society*, vol. 139, pp. 1754–1757, Feb. 2017.

156. S. Kewalramani, G. I. Guerrero-Garca, L. M. Moreau, J. W. Zwanikken, C. A. Mirkin, M. Olvera de la Cruz, and M. J. Bedzyk, "Electrolyte-Mediated Assembly of Charged Nanoparticles," *ACS Central Science*, vol. 2, pp. 219–224, Apr. 2016.

157. Y. Tian, Y. Zhang, T. Wang, H. L. Xin, H. Li, and O. Gang, "Lattice engineering through nanoparticleDNA frameworks," *Nature Materials*, vol. 15, p. 654, Feb. 2016.

158. D. Shechtman, I. Blech, D. Gratias, and J. W. Cahn, "Metallic Phase with Long-Range Orientational Order and No Translational Symmetry," *Physical Review Letters*, vol. 53, pp. 1951–1953, Nov. 1984.

159. T. I. N. G. Li, R. Sknepnek, and M. Olvera de la Cruz, "Thermally Active Hybridization Drives the Crystallization of DNA-Functionalized Nanoparticles," *Journal of the American Chemical Society*, vol. 135, pp. 8535–8541, June 2013.

160. J.-M. Dubois and E. Belin-Ferr, eds., *Complex metallic alloys: fundamentals and applications*. Weinheim: Wiley-VCH, 2011. OCLC: ocn655675976.

161. H. Lin, S. Lee, L. Sun, M. Spellings, M. Engel, S. C. Glotzer, and C. A. Mirkin, "Clathrate colloidal crystals," *Science*, vol. 355, no. 6328, pp. 931–935, 2017.

162. J. S. T. Gongora, G. Favraud, and A. Fratalocchi, "Fundamental and high-order anapoles in all-dielectric metamaterials via fanofeshbach modes competition," *Nanotechnology*, vol. 28, no. 10, p. 104001, 2017.

163. B. Stout and R. McPhedran, "Egocentric physics: Just about mie," *EPL (Europhysics Letters)*, vol. 119, no. 4, p. 44002, 2017.

164. A. E. Miroshnichenko, A. B. Evlyukhin, Y. F. Yu, R. M. Bakker, A. Chipouline, A. I. Kuznetsov, B. Luk'yanchuk, B. N. Chichkov, and Y. S. Kivshar, "Nonradiating anapole modes in dielectric nanoparticles," *Nature Communications*, vol. 6, p. 8069, 2015.